Nusselt Numbers for Superhydrophobic Microchannels and Shrouded Longitudinal-Fin Heat Sinks

A dissertation submitted by
Georgios Karamanis

in partial fulfillment of the requirements for the degree of

Doctor of Philosophy
in
Mechanical Engineering

School of Engineering
Tufts University
August 2018

Certified by:
Professor Marc Hodes
Department of Mechanical Engineering
Tufts University

Committee:
Assistant Professor Erica Cherry Kemmerling
Department of Mechanical Engineering
Tufts University

Committee:
Associate Professor James Adler
Department of Mathematics
Tufts University

Committee:
Professor Alan Lyons
Department of Chemistry
City University of New York

Abstract

Nusselt numbers that are relevant, but not limited, to thermal management of electronics are computed in this thesis. The first two parts of the thesis compute Nusselt numbers for liquid flow between parallel plates that are textured with ridges oriented parallel to the flow. The configurations analyzed are both plates textured, and one plate textured as such and the other one smooth and adiabatic. The flow is laminar and the liquid is in the Cassie state on the textured surface(s). The menisci are flat and adiabatic, and the ridges are isothermal. First, axial conduction is neglected and the three-dimensional developing temperature field is computed assuming a hydrodynamically developed flow, i.e., the Graetz-Nusselt problem is solved. Then, the assumption of negligible axial conduction is relaxed, i.e., the Extended Graetz-Nusselt problem is solved. Effects of viscous dissipation and (uniform) volumetric heat generation are also considered. The last two parts of the thesis are relevant to conjugate forced-convection heat transfer through longitudinal-fin heat sinks. The third part computes and tabulates conjugate Nusselt numbers for such heat sinks. Importantly, the analysis accounts for axial conduction in the coolant and the fin. The flow is laminar, and simultaneously-developing. The heat sink has an adiabatic shroud and its base is isothermal. A conjugate boundary condition applies at the fin-coolant interface to impose continuity of the temperature field and heat flux there. In the last part of the thesis, an algorithm is presented to simultaneously optimize the geometry of an array of such heat sinks utilizing the conjugate Nusselt number tabulations. The optimization algorithm models heat transfer in a circuit pack using the Flow Network Modeling method. The resulting system of nonlinear algebraic equations constitutes the implicit constraints of the optimization problem. The objective function and the explicit constraints of the optimization problem are user defined and arbitrary. The optimization problem is iteratively solved using the Barrier Function method in conjunction with the Trust Region method.

Acknowledgments

First, I would like to express my utmost gratitude towards my advisor, Professor Marc Hodes. Professor Hodes provided excellent guidance throughout the completion of my research and supported me in every aspect. It has been an honor for me to conduct my thesis under the supervision of such an excellent researcher and a caring teacher.

Also, I am beholden to Professor Alan Lyons for all of his technical and carrier advice during my studies.

Next, I would like to express my deep appreciation to Professor Robert White, my first advisor at Tufts, for selflessly guiding me to pursue the right path for my graduate research and for always allowing me to access his lab.

Moreover, my sincere thanks goes to Professor Chris Rogers for his critical insight and constructive criticism.

Finally and most importantly, I am indebted to my parents Ioanni and Maria for their unconditional support throughout my life.

Contents

List of Tables

List of Figures

Part I

Thesis Overview

Chapter 1

Introduction

The thesis computes Nusselt numbers that are relevant but not limited to thermal management of electronics. In Parts II and III, the Nusselt numbers are for flows through diabatic microchannels when the liquid is in the Cassie State. In Parts IV and V, the Nusselt numbers are conjugate ones relevant to longitudinal-fin heat sinks. Although the entire thesis focuses on Nusselt numbers, Parts II and III are not otherwise related to Parts IV and V. The rest of this Introduction provides more high-level context about the Parts of the thesis. We further note that each Part of the thesis corresponds to a published or submitted paper. Specifically, the reference for Part II is [3] (published), that for Part III is [4] (published), that for Part IV is [2] (submitted) and that for Part V is [5] (submitted).

Parts II and III are relevant to direct liquid cooling of electronics and compute Nusselt numbers for liquid flow between parallel plates that are textured with ridges oriented parallel to the flow. The configurations analyzed are both plates textured, and one plate textured as such and the other one smooth and adiabatic. The flow is assumed to be laminar with constant thermophysical properties. The liquid is assumed to be in the Cassie state on the textured surface(s), to which a mixed boundary condition of no-slip on the ridges and no-shear along the menisci applies. The menisci are assumed to be adiabatic too and the ridges isothermal. In Part II axial conduction is neglected and the analysis solves for the three-dimensional developing temperature profile assuming a hydrodynamically developed flow, i.e., it solves the Graetz-Nusselt problem. The dimensionless independent variables are the solid fraction, the dimensionless distance between opposite plates, the dimensionless transverse coordinate along the ridge and the dimensionless streamwise coordinate. The hydrodynamic problem is numerically solved using the Finite Element Method. The thermal problem is reduced using the method of separation of variables to a two-dimensional linear eigenvalue problem in the transverse coordinates which is numerically solved using the Finite Element Method. Expressions are derived for the local and the fully developed Nusselt number along the ridge and that averaged over the composite interface in terms of the eigenvalues and eigenfunctions. Nusselt numbers averaged over the period and length of the domain are also provided. In Part III the assumption of negligible axial conduction is relaxed, i.e., the analysis considers the corresponding Extended Graetz-Nusselt problem. Effects of viscous dissipation and (uniform) volumetric heat generation are also considered. The additional independent variables in this case are the Péclet and Brinkman numbers, and a dimensionless volumetric heat generation rate. The homogeneous part of the thermal problem is reduced using the method of separation of variables to a nonlinear eigenvalue problem in the transverse coordinates which is numerically solved using the Finite Element Method. Expressions are derived for the local and the fully developed Nusselt number along the ridge and that averaged over the composite interface in terms of the eigenvalues, eigenfunctions, Brinkman number, and dimensionless volumetric heat generation rate. Estimates are provided too for the streamwise location where viscous dissipation effects become important.

Insofar as to the contribution of Part III to the literature, which reduces to the less general one of Part II when axial conduction and viscous dissipation effects are ignored, some context is provided here. First, albeit not for simultaneously-developing flow, Parts II and III are the only published work for this microchannel configuration where the temperature field is developing rather than developed. The same holds for capturing dissipation effects in the liquid in Part III. However, other studies, notably those by Kirk et al. [6] and Game et al. [7], have captured meniscus curvature effects in the case of hydrodynamically and thermally fully-developed flow and for a constant heat flux rather than constant temperature boundary condition along the ridges. We note that neither of these boundary conditions is ideal in practice where the heat is input into the solid substrate and a conjugate heat transfer problem need be solved. However and importantly, the analyses in Parts II and III have fewer assumptions invoked than their predecessors. It is also noted that, although the literature review Sections of Parts II and III is not in the vein of a critical review, a more detailed literature review of diabatic flows of liquid in the Cassie state through microchannels is given by Game et al. [7]. Additional effects such as of variable meniscus curvature, temperature-dependent surface tension and thus of thermocapillary stress inducing a transverse velocity field, phase change (evaporation and condensation) along menisci, convection in the subphase, etc., have been treated to a limited extent as mentioned here and by Game et al. [7]. However, it is emphasized that the full, three-dimensional convective transport problem has yet to be formulated and resolved, and the present work is the only published study where the domain is finite in the streamwise direction rather than restricted to a plane. Moreover, every study to date treats certain effects in isolation rather than the full problem. Thus, Part III of this thesis should be viewed as advancing the state of understanding of the diabatic flows of interests, but, there remains much work to be done. This is even more important in the context of experiments than for models, as there is essentially no experimental data to compare the results here or those of others to at present.

Regarding engineering applications of the Nusselt numbers in Parts II and III, direct liquid cooling of microelectronics is perhaps the most obvious one. In such configurations liquid is pumped through a semiconductor and the caloric rather than the convective resistance is often dominant. As such, lubrication provided by superhydrophobic surfaces is of interest as discussed by Lam et al. [8]. However, the coolant that is best suited to such uses on these surfaces is a low temperature liquid metal, e.g., Galinstan, rather than water as the loss of surface area for heat transfer in a poor conductor like water is not likely to be viable [8]. Importantly, such liquid metals have essentially no vapor pressure at temperatures of interest and thus phase change along menisci is negligible as assumed here. Conversely, meniscus curvature is important and it will vary substantially along the streamwise direction of the flow, and thermocapillary stress may be important as well, but temperature-dependent surface tension measurements of such liquids are limited. For liquids like water, or biological fluids, the use of superhydrophobic surfaces in such microchannels is probably more realistic when the liquid needs to be insulated from its surroundings and the pumping power reduced, rather than being used as a coolant.

Part IV and V are relevant to heat transfer through longitudinal fin heat sinks. Part IV computes conjugate Nusselt numbers for such heat sinks. Importantly, the analysis accounts for axial conduction in the coolant and the fin. The flow is laminar, simultaneously-developing, with constant thermophysical properties. A no-slip boundary condition applies at the solid-coolant interfaces. The heat sink has an adiabatic shroud and its base is isothermal. A conjugate boundary condition applies at the fin-coolant interface to impose continuity of the temperature field and the heat flux. At the outlet of the heat sink a uniform pressure and zero-temperature-normal-gradient applies. The independent variables are the dimensionless fin thickness, spacing and length, the Reynolds number of the flow, the Prandtl number of the coolant, and the coolant to fin thermal conductivity ratio. The conjugate heat transfer problem is solved using the Finite Volume Method (CFD) over a relevant range of values of the independent variables relevant to thermal management of electronics, and the corresponding computed conjugate Nusselt numbers are tabulated. Part V develops an algorithm to simultaneously optimize the geometry of an array of heat sinks (fin height, spacing, etc.) found in, e.g., a blade server, utilizing such tabulations for the conjugate Nusselt number. The optimization algorithm models heat transfer in a circuit pack using the Flow Network Modeling method where a circuit pack is discretized into multiple sub-regions each of which is associated with a flow and thermal resistance. The flow and thermal resistances for the heat sinks are evaluated interpolating from the CFD-precomputed results for the Poiseuille and conjugate Nusselt numbers. The resulting system of nonlinear algebraic equations constitutes the implicit constraints of the optimization problem. The objective function and the explicit constraints of the optimization problem are user defined and can be arbitrary. The optimization problem is iteratively solved using the Barrier Function method in conjunction with the Trust Region method.

The practical utility of Parts IV and V of the thesis is rather significant. Thermal engineers that design blade servers and telecommunication circuit packs for data and telecommunication centers, respectively, should benefit from this technology. At present, there is no optimization algorithm that allows them to define an objective function, e.g., have all of the components in a circuit pack operate the same number of degrees centigrade below their maximum operating temperature to maximize reliability, and a set of constraints, e.g., on fin height to thickness ratio for a low-cost extrusion process, and based on them to compute the optimal heat sink geometry. Currently, this is possible by using CFD in a brute-force approach for one of many heat sinks in a circuit pack, but not for an array of them in the context of simultaneous optimization of each heat sink. Once the optimal geometry is estimated for each heat sink using the approach in this work, a detailed CFD simulation is complimentary as it will give the fine details of the velocity and temperature fields and slightly more accurate results based on the cases examined thus far.

The Parts of the thesis follow next. It is noted that the Nomenclature for each Part is given at its end.

Part II

Solution of the Graetz-Nusselt Problem for Liquid Flow over Isothermal Parallel Ridge

Chapter 2

Introduction

Superhydrophobic surfaces, i.e., those with hydrophobic micro- and/or nanoscale protrusions, are of interest in the context of liquid-flow through microchannels, especially in direct liquid cooling applications as a means to reduce flow and thus caloric resistance [8]. When criteria are met [9, 8] the solid-liquid interfaces are confined to the tips of the structures, forming a composite interface along with the liquid-gas interfaces (menisci), as per Fig. 2.1, and the liquid is said to be in the unwetted or Cassie state[10, 11]. Then, the solid-liquid interfaces are subjected to the no-slip [12, 13] boundary condition whereas the menisci are subjected to a low-shear boundary condition. Thus, a lubrication effect is provided which reduces caloric resistance. However, the reduction in the solid-liquid interface area reduces the Nusselt number (Nu) and thus increases the convective component of thermal resistance. A net reduction of the total, i.e., caloric plus convective, thermal resistance can be achieved with proper sizing of the structures [8] and it requires knowledge of Nusselt numbers as a function of the geometry of the channel and the structures. The surfaces can be textured with a variety of periodic structures such as pillars, transverse ridges, or parallel ridges relative to the flow direction [9]. The latter configuration for the ridges is examined here and it is the most favorable from a heat transfer perspective [8, 14].

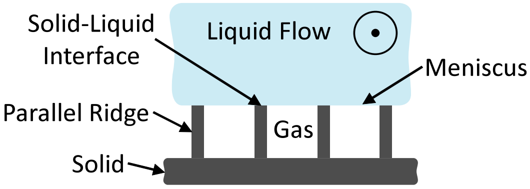

Figure 2.1: Liquid in the Cassie state and the composite interface.

The hydrodynamic effects of structured surfaces with parallel ridges have been studied for flat and curved menisci[15, 16, 17, 18, 19]. However, there is a relatively limited body of work on heat transfer effects. Enright *et al.* [14] derived an expression for the Nusselt number for fully developed flow through a microchannel with isoflux structured surfaces as a function of the (apparent) hydrodynamic and thermal slip lengths. Moreover, Enright *et al.* [14] developed analytical expressions for slip lengths for structured surfaces with parallel or transverse ridges or pillar arrays assuming flat and adiabatic menisci. Ng and Wang [20] derived semi-analytical expressions for the thermal slip length for isothermal parallel ridges while accounting for conduction through the gas phase. Lam *et al.* [21] derived expressions for the thermal slip length for isoflux and isothermal parallel ridges accounting for small meniscus curvature. Hodes *et al.* [22] captured the effects of evaporation and condensation along menisci on the thermal slip length for isoflux ridges. Lam *et al.* [23] developed expressions for the Nusselt number for Couette flow as a function of the slip lengths for various boundary conditions. Also, Lam *et al.* [23] discussed when Nu results from the molecular slip literature can be used to capture the effects of apparent slip. Maynes *et al.* [24] numerically investigated the thermal transport in microchannels with isothermal transverse ridges and flat menisci taking into account the heat transfer through the gas and/or vapor in the cavities. Maynes *et al.* [25] and Maynes & Crockett [26] developed expressions for the Nusselt number and the thermal slip length for microchannels with isoflux transverse and parallel ridges, respectively, assuming flat menisci and using the Navier slip approximation for the velocity profile. Kirk *et al.* [6] also developed expressions for the Nusselt number for isoflux parallel ridges using the fully-resolved velocity field in the thermal energy equation. Furthermore, Kirk *et al.* [6] accounted for small meniscus curvature using a boundary perturbation method.

The present work develops semi-analytical expressions for the Nusselt number for the case of isothermal parallel ridges for hydrodynamically developed and thermally developing flow with negligible axial conduction, i.e., for the *Graetz-Nusselt problem*[1] [28, 29, 30], and it is emphasized that we do not assume diffusive heat transfer near the composite interface.

We consider three different configurations for the parallel ridges: 1) one plate textured and the other one smooth, as per Fig. 2.2; 2) both plates textured and the ridges aligned in the transverse direction (see Fig. 2.3); 3) both plates textured and the ridges staggered in

---

[1] We use the term *Graetz-Nusselt problem* rather than *Graetz problem* because they refer to flow between parallel plates and through circular duct, respectively, as per the distinction made in Shah and London [27].

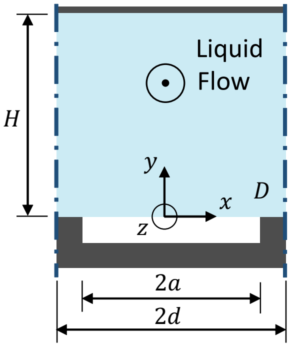

Figure 2.2: Schematic of the domain when one plate is textured and the other one is smooth.

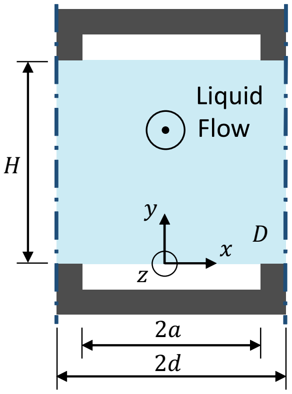

Figure 2.3: Schematic of the domain when both plates are textured and the ridges are aligned.

the transverse direction by half a pitch (see Fig. 2.4). The solution approach is similar in all three configurations. Therefore, it suffices to present here the detailed analyses for the first one and the relevant parts of the analysis for the other two configurations in the Appendix.

The domain (D) for the first configuration is depicted in Fig. 2.2, where $|x| \leq d$ and $0 \leq y \leq H$ and where $2d$ is the pitch of the ridges and H is the distance between the parallel plates. The hydraulic diameter of the domain (D_h) is $2H$. The width of the meniscus is $2a$. The curvature of the meniscus is neglected [21, 6] and the triple contact lines coincide with the corners of the ridges at $x = |a|$ and $y = 0$. The cavities may be filled with inert gas and/or vapor. Along the composite interface ($y = 0$), a no-shear boundary condition is applied for $|x| < a$ and a no-slip one is imposed for $a < |x| < d$. A no-slip boundary condition is also imposed on the smooth upper plate. Symmetry boundary conditions apply at the $x = |d|$ boundaries. The flow is pressure driven, steady, laminar, hydrodynamically developed, and thermally developing with constant thermophysical properties and negligible

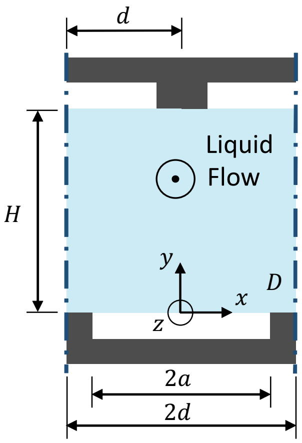

Figure 2.4: Schematic of the domain when both plates are textured and the ridges are staggered by half a pitch.

axial conduction and viscous dissipation. The ridges on the lower plate are isothermal, whereas the upper plate and the meniscus are considered adiabatic. The temperature profile in the liquid starts developing at $z = 0$ from an arbitrary (unless otherwise stated) two-dimensional distribution $T_{\text{in}}(x, y)$. Effects due to Marangoni stresses [31, 32], evaporation and condensation [22], and gas diffusion in the liquid phase are neglected. The independent dimensionless variables are the solid fraction of the ridge ($\phi = (d - a)/d$) and the aspect ratio of the domain (H/d).

Chapter 3

Analysis

3.1 Hydrodynamic Problem

The relevant form of the streamwise-momentum equation is

$$\frac{\partial^2 w}{\partial x^2} + \frac{\partial^2 w}{\partial y^2} = \frac{1}{\mu}\frac{\mathrm{d}p}{\mathrm{d}z} \tag{3.1}$$

where w is the streamwise velocity, $\mathrm{d}p/\mathrm{d}z$ is the prescribed pressure gradient, and μ is the dynamic viscosity. Denoting nondimensional variables with tildes, Eq. (3.1) and the boundary conditions imposed to it are rendered dimensionless by defining

$$\tilde{x} = \frac{x}{a} \tag{3.2}$$

$$\tilde{y} = \frac{y}{a} \tag{3.3}$$

$$\tilde{H} = \frac{H}{a} \tag{3.4}$$

$$\tilde{w} = \frac{2\mu w}{aH\left(-\mathrm{d}p/\mathrm{d}z\right)} \tag{3.5}$$

Then, Eq. (3.1) becomes

$$\frac{\partial^2 \tilde{w}}{\partial \tilde{x}^2} + \frac{\partial^2 \tilde{w}}{\partial \tilde{y}^2} = -\frac{2}{\tilde{H}} \tag{3.6}$$

subjected to

$$
\begin{aligned}
\frac{\partial \tilde{w}}{\partial \tilde{y}} &= 0 \quad \text{for } |\tilde{x}| < 1,\ \tilde{y} = 0 && (3.7)\\
\tilde{w} &= 0 \quad \text{for } 1 < |\tilde{x}| < \tilde{d},\ \tilde{y} = 0 && (3.8)\\
\tilde{w} &= 0 \quad \text{for } |\tilde{x}| < \tilde{d},\ \tilde{y} = \tilde{H} && (3.9)\\
\frac{\partial \tilde{w}}{\partial \tilde{x}} &= 0 \quad \text{for } |\tilde{x}| = \tilde{d},\ 0 < \tilde{y} < \tilde{H} && (3.10)
\end{aligned}
$$

where $\tilde{d} = d/a$ is the dimensionless (half) pitch of the ridges.

This hydrodynamic problem has been solved analytically [15] and semi-analytically [16, 18]. However, no analytical solutions have been found for the problems in the Appendix. Therefore, the velocity field is numerically determined here for all cases, which also facilitates the numerical solution of the thermal energy equation in Section VI. The numerical results were validated against the analytical solution [15] using the computed Poiseuille number (fRe), where

$$
\begin{aligned}
\mathrm{Re} &= \frac{\rho \overline{w} D_\mathrm{h}}{\mu} && (3.11)\\
f &= -\frac{\mathrm{d}p}{\mathrm{d}z}\frac{2D_\mathrm{h}}{\rho \overline{w}^2} && (3.12)\\
\overline{w} &= \frac{1}{2dH}\int_0^H \int_{-d}^{d} w \,\mathrm{d}x\mathrm{d}y && (3.13)
\end{aligned}
$$

are the Reynolds number based on the hydraulic diameter, the friction factor and the mean velocity of the flow, respectively, and ρ is the density. From Eqs. (3.5) and (3.11)-(3.13) it follows that the Poiseuille number is given by

$$
f\mathrm{Re} = 16\frac{\tilde{H}}{\overline{\tilde{w}}} \tag{3.14}
$$

where

$$
\overline{\tilde{w}} = \frac{1}{2\tilde{d}\tilde{H}}\int_0^{\tilde{H}} \int_{-\tilde{d}}^{\tilde{d}} \tilde{w} \,\mathrm{d}\tilde{x}\mathrm{d}\tilde{y} \tag{3.15}
$$

is the dimensionless mean velocity of the flow.

3.2 Thermal Problem

The relevant form of the dimensional thermal energy equation is

$$w\frac{\partial T}{\partial z} = \alpha\left(\frac{\partial^2 T}{\partial x^2}+\frac{\partial^2 T}{\partial y^2}\right) \tag{3.16}$$

where T and α are the temperature and the thermal diffusivity of the liquid, respectively. Defining the dimensionless temperature $\tilde{T}$ and the dimensionless streamwise coordinate $\tilde{z}$ as

$$\tilde{T} = \frac{T-T_{\mathrm{sl}}}{T_{\mathrm{ref}}-T_{\mathrm{sl}}} \tag{3.17}$$

$$\tilde{z} = \frac{2\alpha\mu z}{a^3 H\left(-\mathrm{d}p/\mathrm{d}z\right)} \tag{3.18}$$

where T_{sl} is the constant temperature of the ridge and T_{ref} is a reference temperature for the problem, Eq. (3.16) becomes

$$\tilde{w}\frac{\partial \tilde{T}}{\partial \tilde{z}} = \frac{\partial^2 \tilde{T}}{\partial \tilde{x}^2}+\frac{\partial^2 \tilde{T}}{\partial \tilde{y}^2} \tag{3.19}$$

It is subject to the following boundary conditions

$$\frac{\partial \tilde{T}}{\partial \tilde{y}} = 0 \quad \text{for } |\tilde{x}|<1,\ \tilde{y}=0 \tag{3.20}$$

$$\tilde{T} = 0 \quad \text{for } 1<|\tilde{x}|<\tilde{d},\ \tilde{y}=0 \tag{3.21}$$

$$\frac{\partial \tilde{T}}{\partial \tilde{y}} = 0 \quad \text{for } |\tilde{x}|<\tilde{d},\ \tilde{y}=\tilde{H} \tag{3.22}$$

$$\frac{\partial \tilde{T}}{\partial \tilde{x}} = 0 \quad \text{for } |\tilde{x}|=\tilde{d},\ 0<\tilde{y}<\tilde{H} \tag{3.23}$$

$$\tilde{T} = \tilde{T}_{\mathrm{in}} \quad \text{at } \tilde{z}=0 \tag{3.24}$$

where $\tilde{T}_{\mathrm{in}}(\tilde{x},\tilde{y})$ is the prescribed dimensionless temperature profile at the inlet of the domain ($\tilde{z}=0$).

Seeking separable solutions of the form $\tilde{T}=\psi(\tilde{x},\tilde{y})g(\tilde{z})$, which separate the streamwise coordinate $\tilde{z}$ from the transverse coordinates $\tilde{x}$ and $\tilde{y}$, it can be shown that $g(\tilde{z})=\exp(-\lambda\tilde{z})$ and $\psi(\tilde{x},\tilde{y})$ satisfies

$$\nabla^2\psi = -\lambda\tilde{w}\psi \tag{3.25}$$

with λ real and positive[1]. Note that $\psi(\tilde{x},\tilde{y})$ cannot be separated further into a product of a function of $\tilde{x}$ and one of $\tilde{y}$ since the velocity field, $\tilde{w}=\tilde{w}(\tilde{x},\tilde{y})$, is not separable in such a way. Equation (3.25) satisfies the boundary conditions

---

[1] To show that λ is real and positive we multiply Eq. (3.25) by the complex conjugate of ψ, integrate over the domain, and use the Divergence Theorem.

$$\frac{\partial\psi}{\partial\tilde{y}} = 0 \quad \text{for } |\tilde{x}| < 1,\ \tilde{y} = 0 \tag{3.26}$$

$$\psi = 0 \quad \text{for } 1 < |\tilde{x}| < \tilde{d},\ \tilde{y} = 0 \tag{3.27}$$

$$\frac{\partial\psi}{\partial\tilde{y}} = 0 \quad \text{for } |\tilde{x}| < \tilde{d},\ \tilde{y} = \tilde{H} \tag{3.28}$$

$$\frac{\partial\psi}{\partial\tilde{x}} = 0 \quad \text{for } |\tilde{x}| = \tilde{d},\ 0 < \tilde{y} < \tilde{H} \tag{3.29}$$

and so constitutes a two-dimensional Sturm-Liouville eigenvalue problem for λ and the corresponding eigenfunction ψ, with weight function $\tilde{w}(\tilde{x},\tilde{y})$. Assuming that the eigenvalues are discrete and there are infinitely many, let λ_i and ψ_i denote the i-th eigenvalue and eigenfunction, respectively, ordered such that $0 < \lambda_1 < \lambda_2 < \cdots < \lambda_i < \cdots \to \infty$. The eigenfunctions are orthogonal with respect to the inner product defined by

$$\langle F_1, F_2\rangle = \int_0^{\tilde{H}} \int_{-\tilde{d}}^{\tilde{d}} \tilde{w} F_1 F_2 \mathrm{d}\tilde{x}\mathrm{d}\tilde{y} \tag{3.30}$$

that is,

$$\langle \psi_i, \psi_j\rangle = 0 \text{ for } i \neq j \tag{3.31}$$

Moreover, the eigenfunctions are unique up to a multiplication by a constant. Thus, for the rest of the present analysis we normalize ψ_i such that

$$\langle \psi_i, \psi_i\rangle = 1 \tag{3.32}$$

The eigenvalue problem is solved numerically. The calculation of ψ_i and λ_i is detailed in Section VI, and for the rest of the present analysis they are assumed to be known.

We proceed by expressing the solution $\tilde{T}(\tilde{x},\tilde{y},\tilde{z})$ as a linear combination of the eigenfunctions,

$$\tilde{T}(\tilde{x},\tilde{y},\tilde{z}) = \sum_{i=1}^{\infty} c_i \psi_i(\tilde{x},\tilde{y}) \exp(-\lambda_i \tilde{z}) \tag{3.33}$$

using the expansion coefficients c_i. The c_i are determined by taking the inner product of Eq. (3.33) with ψ_i at the inlet $\tilde{z} = 0$, where $\tilde{T}(\tilde{x},\tilde{y},0) = \tilde{T}_{\text{in}}(\tilde{x},\tilde{y})$, giving

$$c_i = \left\langle \psi_i, \tilde{T}_{\text{in}} \right\rangle \tag{3.34}$$

Substituting Eq. (3.34) into Eq. (3.33), the dimensionless temperature profile takes the form

$$\tilde{T}(\tilde{x},\tilde{y},\tilde{z}) = \sum_{i=1}^{\infty} \left\langle \psi_i, \tilde{T}_{\text{in}} \right\rangle \psi_i(\tilde{x},\tilde{y}) \exp(-\lambda_i \tilde{z}) \tag{3.35}$$

Chapter 4

Nusselt Number

The local Nusselt number is defined as

$$\mathrm{Nu_l} = \frac{h_\mathrm{l} D_\mathrm{h}}{k} \tag{4.1}$$

where h_l is the local heat transfer coefficient and k is the thermal conductivity of the liquid. An energy balance at a point along the ridges yields

$$-k \left.\frac{\partial T}{\partial y}\right|_{y=0} = h_\mathrm{l}\left(T_\mathrm{sl} - T_\mathrm{b}\right) \tag{4.2}$$

where T_b is the bulk temperature of the liquid defined as

$$T_\mathrm{b} = \frac{1}{2dH\overline{w}} \int_0^H \int_{-d}^{d} wT \mathrm{d}x\mathrm{d}y \tag{4.3}$$

Combining Eqs. (4.1)-(4.3), the Nusselt number can be written in terms of dimensionless quantities as

$$\mathrm{Nu_l} \quad = \quad 2\frac{\tilde{H}}{\tilde{T}_\mathrm{b}} \left.\frac{\partial \tilde{T}}{\partial \tilde{y}}\right|_{\tilde{y}=0} \tag{4.4}$$

where $\tilde{T}_\mathrm{b}$ is the dimensionless bulk temperature of the liquid defined as

$$\tilde{T}_\mathrm{b} = \frac{1}{2\tilde{d}\tilde{H}\overline{\tilde{w}}} \left\langle \tilde{T}, 1 \right\rangle \tag{4.5}$$

Next, combining Eqs. (3.14), (3.33), (4.4) and (4.5) yields

$$\mathrm{Nu_l} \quad = \quad 64\frac{\tilde{H}^3\tilde{d}}{f\mathrm{Re}} \frac{\sum\limits_{i=1}^{\infty} \left\langle \psi_i, \tilde{T}_\mathrm{in} \right\rangle \left.\frac{\partial \psi_i}{\partial \tilde{y}}\right|_{\tilde{y}=0} \exp\left(-\lambda_i \tilde{z}\right)}{\sum\limits_{i=1}^{\infty} \left\langle \psi_i, \tilde{T}_\mathrm{in} \right\rangle \left\langle \psi_i, 1 \right\rangle \exp\left(-\lambda_i \tilde{z}\right)} \tag{4.6}$$

The local Nusselt number for the limiting case of fully developed flow ($\mathrm{Nu}_{\mathrm{l,fd}}$) follows from the evaluation of Eq. (4.6) as $\tilde{z} \to \infty$. Given that the λ_i are real and $0 < \lambda_1 < \lambda_2 < ... < \lambda_i < ... \to \infty$, upon dividing both the numerator and the denominator of Eq. (4.6) by $e^{-\lambda_1 \tilde{z}}$ and letting $\tilde{z} \to \infty$, only the first term of each sum remains. It follows that

$$\mathrm{Nu}_{\mathrm{l,fd}} = 64 \frac{\tilde{H}^3 \tilde{d}}{f\mathrm{Re}} \frac{\left.\frac{\partial \psi_1}{\partial \tilde{y}}\right|_{\tilde{y}=0}}{\langle \psi_1, 1 \rangle} \tag{4.7}$$

$\mathrm{Nu}_{\mathrm{l,fd}}$ is a function only of the first eigenfunction and it is independent of the inlet temperature profile. However, in the thermally developing region Nu_{l} is a function of $\tilde{T}_{\mathrm{in}}$.

The Nusselt number averaged over the composite interface is

$$\mathrm{Nu} = \frac{1}{2d} \int_{-d}^{d} \mathrm{Nu}_{\mathrm{l}} \mathrm{d}x \tag{4.8}$$

Substituting Eq. (4.6) into Eq. (4.8) and utilizing the symmetry of the eigenvalue problem with respect to the y axis and the boundary condition given by Eq. (3.26) yields

$$\mathrm{Nu} = 64 \frac{\tilde{H}^3}{f\mathrm{Re}} \frac{\sum_{i=1}^{\infty} \left\langle \psi_i, \tilde{T}_{\mathrm{in}} \right\rangle \int_1^{\tilde{d}} \left.\frac{\partial \psi_i}{\partial \tilde{y}}\right|_{\tilde{y}=0} \mathrm{d}\tilde{x} \, \exp\left(-\lambda_i \tilde{z}\right)}{\sum_{i=1}^{\infty} \left\langle \psi_i, \tilde{T}_{\mathrm{in}} \right\rangle \langle \psi_i, 1 \rangle \exp\left(-\lambda_i \tilde{z}\right)} \tag{4.9}$$

Next, we express the integral in the numerator of Eq. (4.9) as a function of the inner product $\langle \psi_i, 1 \rangle$. This is because it is more accurate to numerically evaluate $\langle \psi_i, 1 \rangle$ than $\int_1^{\tilde{d}} \partial \psi_i / \partial \tilde{y}|_{\tilde{y}=0} \, \mathrm{d}\tilde{x}$ as the latter requires numerical differentiation in order to evaluate the derivative at the boundary. The steps are as follows. First, we rearrange Eq. (3.25) and integrate it over the cross section of the domain to obtain

$$\int_0^{\tilde{H}} \int_{-\tilde{d}}^{\tilde{d}} -\frac{1}{\lambda_i} \nabla^2 \psi_i \mathrm{d}\tilde{x} \mathrm{d}\tilde{y} = \langle \psi_i, 1 \rangle \tag{4.10}$$

Then, applying the Divergence Theorem to the left-hand side of Eq. (4.10), we find that

$$-\frac{1}{\lambda_i} \oint_{\partial D} \nabla \psi_i \cdot \hat{\mathrm{n}} \mathrm{d}\tilde{S} = \langle \psi_i, 1 \rangle \tag{4.11}$$

where $\hat{\mathrm{n}}$ is the outward pointing unit normal vector on the boundary ∂D and $\tilde{S}$ is a dimensionless coordinate along ∂D. Then, imposing boundary conditions (3.26)-(3.29) we obtain

$$\int_1^{\tilde{d}} \left.\frac{\partial \psi_i}{\partial \tilde{y}}\right|_{\tilde{y}=0} \mathrm{d}\tilde{x} = \frac{\lambda_i}{2} \langle \psi_i, 1 \rangle \tag{4.12}$$

Inserting this result into Eq. (4.9) yields

$$\mathrm{Nu} \quad = \quad 32\frac{\tilde{H}^3}{f\mathrm{Re}}\frac{\sum\limits_{i=1}^{\infty}\left\langle \psi_i, \tilde{T}_{\mathrm{in}}\right\rangle \langle \psi_i, 1\rangle \lambda_i \exp\left(-\lambda_i \tilde{z}\right)}{\sum\limits_{i=1}^{\infty}\left\langle \psi_i, \tilde{T}_{\mathrm{in}}\right\rangle \langle \psi_i, 1\rangle \exp\left(-\lambda_i \tilde{z}\right)} \tag{4.13}$$

The Nusselt number averaged over the composite interface for the limiting case of fully developed flow ($\mathrm{Nu}_{\mathrm{fd}}$) follows in the same manner as Eq. (4.7) and it is given by

$$\mathrm{Nu}_{\mathrm{fd}} \quad = \quad 32\frac{\tilde{H}^3\lambda_1}{f\mathrm{Re}} \tag{4.14}$$

$\mathrm{Nu}_{\mathrm{fd}}$ is a function only of the first eigenvalue λ_1 and it is independent of $\tilde{T}_{\mathrm{in}}$.

The Nusselt number averaged over the composite interface and the streamwise length of the domain is defined as

$$\overline{\mathrm{Nu}} = \frac{1}{\tilde{z}}\int_0^{\tilde{z}} \mathrm{Nu} d\tilde{z} \tag{4.15}$$

Substituting Eq. (4.13) into Eq. (4.15), it follows that

$$\overline{\mathrm{Nu}} \quad = \quad 32\frac{\tilde{H}^3}{f\mathrm{Re}}\frac{1}{\tilde{z}}\ln\left(\frac{\sum\limits_{i=1}^{\infty}\left\langle \psi_i, \tilde{T}_{\mathrm{in}}\right\rangle \langle \psi_i, 1\rangle}{\sum\limits_{i=1}^{\infty}\left\langle \psi_i, \tilde{T}_{\mathrm{in}}\right\rangle \langle \psi_i, 1\rangle \exp\left(-\lambda_i \tilde{z}\right)}\right) \tag{4.16}$$

In the case of a uniform inlet temperature (UIT) at T_{ref}, we have $\tilde{T}_{\mathrm{in}} = 1$. Then, the foregoing expression reduces to

$$\overline{\mathrm{Nu}}_{\mathrm{UIT}} \quad = \quad 32\frac{\tilde{H}^3}{f\mathrm{Re}}\frac{1}{\tilde{z}}\ln\left(\frac{1}{\tilde{T}_{\mathrm{b}}}\right) \tag{4.17}$$

It is emphasized that Eqs (4.6), (4.13), (4.16) and (4.17) hold for all streamwise locations $\tilde{z}$; however, to achieve a given accuracy, more terms are required in the evaluation of each sum as $\tilde{z}$ is decreased. Moreover, expressions for the Nusselt number averaged only over the width of the ridge rather than the composite interface follow by dividing Eqs. (4.13), (4.14), (4.16) and (4.17) by the solid fraction.

Chapter 5

Results

In this Section we present the results for the case at hand and some representative ones for the cases in the Appendix for comparison. The additional results are presented in the Appendix.

Figure 5.1 plots the fully developed Nusselt number averaged over the composite interface, $\mathrm{Nu}_{\mathrm{fd}}$, versus the solid fraction ϕ for aspect ratios of $H/d = 1,\ 1.5,\ 2,\ 4,\ 6,\ 10$ and 100, when the lower plate is textured with isothermal ridges and the upper one is smooth and adiabatic. The dashed curve corresponds to smooth plates with Nusselt number $\mathrm{Nu}_{\mathrm{fd,s}} = 4.86$. The results obey the expected asymptotic behavior as $\phi \to 1$, with $\mathrm{Nu}_{\mathrm{fd}} \to \mathrm{Nu}_{\mathrm{fd,s}}$, irrespective of the aspect ratio. Additionally as $\phi \to 0$, $\mathrm{Nu}_{\mathrm{fd}}$ tends to zero because the available area for heat transfer vanishes. Moreover, for a given ϕ (excluding the aforementioned limits) as $H/d \to 0$ and $H/d \to \infty$, $\mathrm{Nu}_{\mathrm{fd}}$ tends to zero and to $\mathrm{Nu}_{\mathrm{fd,s}}$, respectively. This is because as $H/d \to 0$ heat is mainly advected by the part of the flow above the shear-free meniscus as opposed to the relatively stagnant liquid above the ridges degrading the heat transfer. In the other limit, as $H/d \to \infty$ the difference between the temperature of the ridge and the mean temperature of the composite interface becomes significantly smaller than the difference between the temperature of the ridge and the bulk temperature of the flow.

Figure 5.2 plots the fully developed local Nusselt number, $\mathrm{Nu}_{\mathrm{l,fd}}$, versus the normalized coordinate along the ridge $(\tilde{x} - 1) / \left(\tilde{d} - 1\right)$ for $H/d = 10$ and $\phi = 0.01,\ 0.1$ and 0.99. The results show that $\mathrm{Nu}_{\mathrm{l,fd}}$ increases with decreasing ϕ, indicating a local enhancement of heat transfer. The same trend has been observed in previous studies [25] and it is due to the fact that as $\phi \to 0$ the velocity of the liquid close to the ridge increases. Figure 5.3 plots the fully developed Nusselt number averaged over the width of the ridge, $\mathrm{Nu}_{\mathrm{fd,ridge}}$, versus the

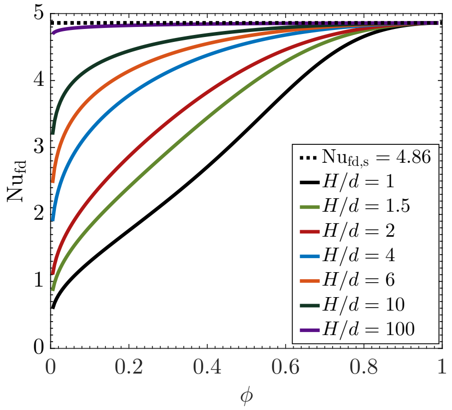

Figure 5.1: $\mathrm{Nu}_{\mathrm{fd}}$ vs. ϕ for selected H/d when one plate is textured with isothermal ridges and the other one is smooth and adiabatic.

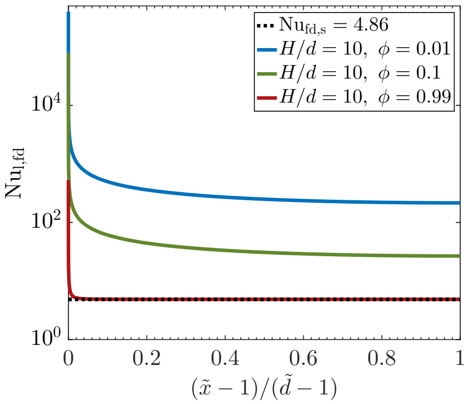

Figure 5.2: $\mathrm{Nu}_{\mathrm{l,fd}}$ vs. the normalized coordinate $(\tilde{x}-1)/\left(\tilde{d}-1\right)$ along the ridge for $H/d = 10$ and selected values of ϕ when one plate is textured with isothermal ridges and the other one is smooth and adiabatic.

solid fraction. In summary, the overall effect of the decrease in the available heat transfer area and the local enhancement of heat transfer for $\phi < 1$ is an increase in the convective portion of the total thermal resistance that is completely captured in Fig. 5.1.

For the case of uniform inlet temperature (UIT), Figs 5.4 and 5.5 plot $\mathrm{Nu}_{\mathrm{UIT}}$ and $\overline{\mathrm{Nu}}_{\mathrm{UIT}}$ versus $z^* = z/(D_{\mathrm{h}}\mathrm{Pe}) = \tilde{z}/\left(4\tilde{H}^2\overline{\tilde{w}}\right)$ for $\phi = 0.01$ and 0.1, respectively. We present the results in the thermal entrance region as function of z^* instead of $\tilde{z}$ to allow for direct comparison of them with those for non-structured channels. The results were computed using the first 29 eigenvalues[1]. The results exhibit the correct asymptotic behavior as

---

[1] If 28 eigenvalues are used instead the maximum discrepancies for the presented values of $\mathrm{Nu}_{\mathrm{UIT}}$ and $\overline{\mathrm{Nu}}_{\mathrm{UIT}}$ are less than 0.002% and 0.0003%, respectively, and if 25 eigenvalues are used instead the maximum discrepancies are less than 0.09% and 0.02%, respectively.

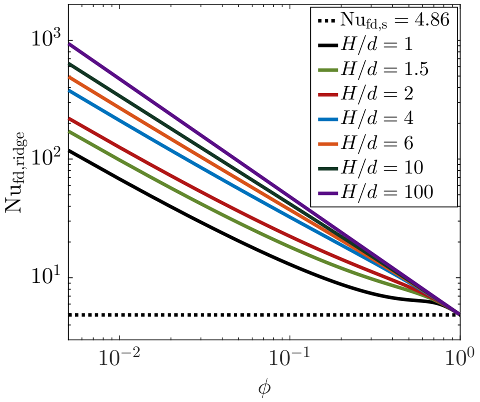

Figure 5.3: $\mathrm{Nu}_{\mathrm{fd,ridge}}$ vs. ϕ for selected H/d when one plate is textured with isothermal ridges and the other one is smooth and adiabatic.

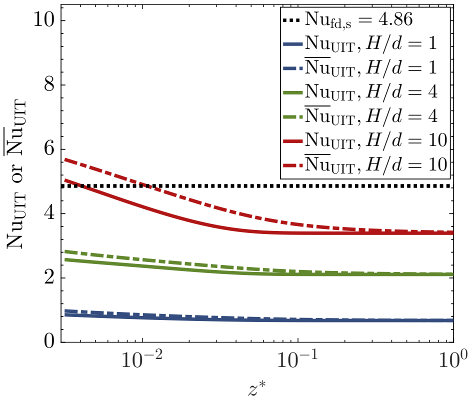

Figure 5.4: $\mathrm{Nu}_{\mathrm{UIT}}$ and $\overline{\mathrm{Nu}}_{\mathrm{UIT}}$ vs. z^* for selected H/d when one plate is textured with isothermal ridges and the other one is smooth and adiabatic for $\phi = 0.01$.

$z^* \to 0$ and $z^* \to \infty$; in the former case both $\mathrm{Nu}_{\mathrm{UIT}}$ and $\overline{\mathrm{Nu}}_{\mathrm{UIT}}$ increase monotonically with decreasing z^*, and in the latter case they tend to $\mathrm{Nu}_{\mathrm{fd}}$. The first 10 eigenvalues and the corresponding expansion coefficients that were computed for $H/d = 4$ at $\phi = 0.01$ and 0.1 are provided in Table 1.

Figures 5.6 and 5.7 compare the computed values of $f\mathrm{Re}$ and $\mathrm{Nu}_{\mathrm{fd}}$, respectively, for the case when one plate is textured and the other one is smooth (solid curves), to the case in the Appendix when both plates are textured and the ridges are aligned in the transverse direction (dashed curves). In both cases one plate has isothermal ridges and the other one is adiabatic. Although $f\mathrm{Re}$ is significantly reduced if both plates are textured, especially as $\phi \to 0$, $\mathrm{Nu}_{\mathrm{fd}}$ changes by only a small fraction due to texturing. More importantly, as per Fig. 5.7, $\mathrm{Nu}_{\mathrm{fd}}$ decreases if both plates are textured and heat is exchanged through the domain only through

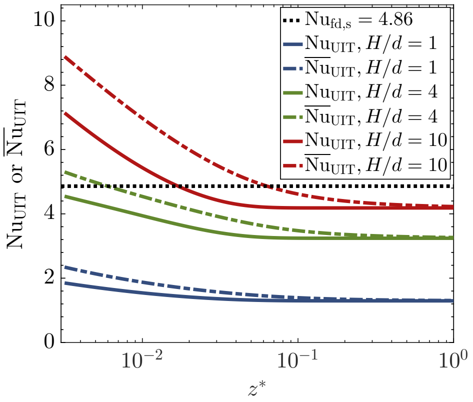

Figure 5.5: $\mathrm{Nu}_{\mathrm{UIT}}$ and $\overline{\mathrm{Nu}}_{\mathrm{UIT}}$ vs. z^* for selected H/d when one plate is textured with isothermal ridges and the other one is smooth and adiabatic for $\phi = 0.1$.

$H/d = 4$			
$\phi = 0.01$		$\phi = 0.1$	
λ_i	c_i	λ_i	c_i
4.375E-02	3.441	6.578E-02	3.428
6.078E-01	4.248E-01	6.923E-01	6.707E-01
1.976E+00	1.309E-01	2.039E+00	2.504E-01
4.174E+00	4.645E-02	4.130E+00	9.351E-02
5.478E+00	5.006E-02	5.453E+00	5.008E-02
6.832E+00	3.990E-02	6.791E+00	2.538E-02
7.400E+00	4.909E-02	7.367E+00	7.305E-02
9.063E+00	5.237E-02	9.289E+00	8.425E-02
1.115E+01	7.095E-03	1.075E+01	7.194E-03
1.197E+01	4.493E-02	1.230E+01	8.377E-02

Table 5.1: First 10 eigenvalues and corresponding expansion coefficients for $H/d = 4$ and $\phi = 0.01$ and 0.1 when one plate is textured with isothermal ridges, the other one is smooth and adiabatic and $\tilde{T}_{\mathrm{in}} = 1$.

the isothermal ridges of one plate. This can be explained by comparing Figs. 5.9 and 5.8 that present the contour plots of the scaled dimensionless streamwise velocity $\tilde{w}/\overline{\tilde{w}}$ for the cases at hand for $H/d = 4$ and $\phi = 0.3$. Indeed, when both plates are textured and the ridges are aligned, as per Fig. 5.8, the flow exhibits higher velocities closer to the center of the domain, but lower velocities closer to the ridge. Thus, the convective thermal transport is degraded. When one plate is smooth, however (see Fig. 5.9), the velocity in the vicinity of the ridge is higher and so enhances heat transfer. This can be quantified by considering the ratio (R) of the average velocity of the flow in an area close to the ridge, i.e., $0 \leq \tilde{x} \leq \tilde{d}$ and $0 \leq \tilde{y} \leq \tilde{H}/2$, over the mean velocity of the flow

$$R = \frac{2\int_0^{\tilde{H}/2}\int_0^{\tilde{d}} \tilde{w} \mathrm{d}\tilde{x} \mathrm{d}\tilde{y}}{\tilde{d}\tilde{H}\overline{\tilde{w}}} \tag{5.1}$$

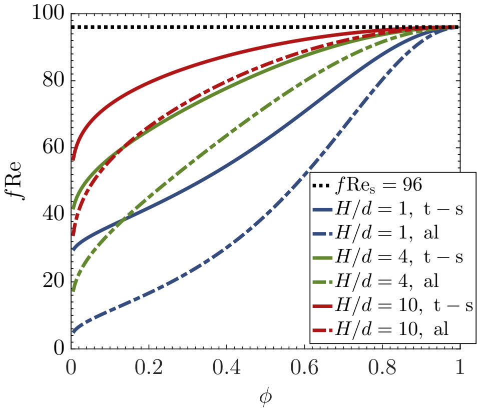

Figure 5.6: fRe vs. ϕ for selected H/d when one plate is textured with isothermal ridges and the other one is adiabatic and either smooth (t−s) or textured with aligned ridges (al).

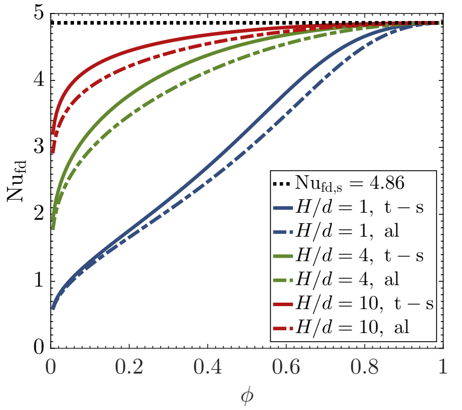

Figure 5.7: $\mathrm{Nu_{fd}}$ vs. ϕ for selected H/d when one plate is textured with isothermal ridges and the other one is adiabatic and either smooth (t−s) or textured with aligned ridges (al).

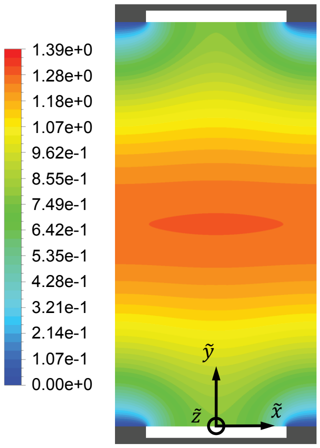

Figure 5.8: Contour plot of $\tilde{w}/\overline{\tilde{w}}$ when one plate is textured with isothermal and the other one with adiabatic ridges and the ridges are aligned (al) for $H/d = 4$ and $\phi = 0.3$.

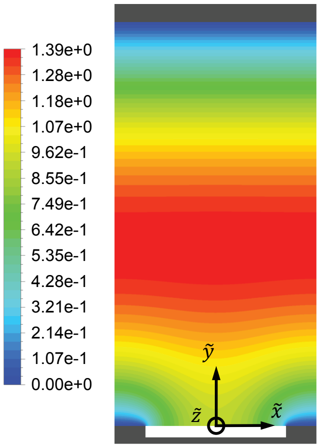

Figure 5.9: Contour plot of $\tilde{w}/\overline{\tilde{w}}$ when one plate is textured with isothermal ridges and the other one is adiabatic and smooth (t − s) for $H/d = 4$ and $\phi = 0.3$.

When both plates are textured and the ridges are aligned R is equal to 1 due to symmetry, but, when one plate is smooth, R becomes 1.127 for the prescribed values of H/d and ϕ, which indicates higher velocities close to the ridge. The same observations can be made for the case when both plates are textured, but the ridges are staggered in the transverse direction. The corresponding plots for $f\mathrm{Re}$ and $\mathrm{Nu}_{\mathrm{fd}}$ and the contour plot of the scaled dimensionless streamwise velocity are presented in the Appendix.

Finally, Fig. 5.10 compares the computed values of $\mathrm{Nu}_{\mathrm{fd}}$ when both plates are textured with isothermal aligned ridges against those calculated for the same configuration but for isoflux ridges ($\mathrm{Nu}_{\mathrm{fd,if}}$) by Kirk *et al.* [6]. The results show that depending on the aspect ratio H/d there is a range for ϕ where the fully developed Nusselt number average over the composite interface for isothermal ridges is slightly higher than for isoflux ridges despite the fact that the fully developed Nusselt number for smooth isothermal plates is smaller than for isoflux plates.

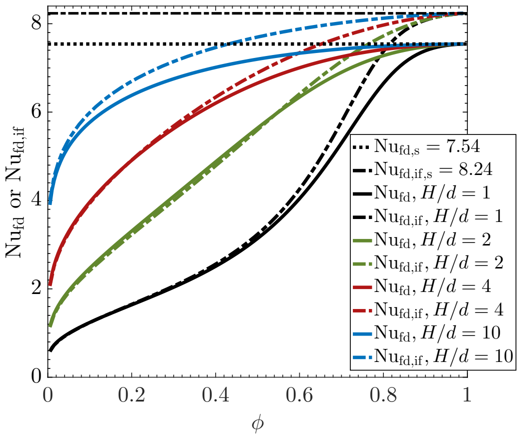

Figure 5.10: Nu$_{\mathrm{fd}}$ and Nu$_{\mathrm{fd,if}}$ vs. ϕ for selected H/d when both plates are textured with aligned isothermal and isoflux ridges, respectively.

Chapter 6

Conclusions

We developed semi-analytical expressions for the Nusselt number for the case of hydrodynamically developed and thermally developing flow between parallel plates that are textured with ridges oriented parallel to the flow. The ridges of one plate are isothermal and the other plate can be smooth and adiabatic, or textured with adiabatic or isothermal ridges. When both plates are textured, the ridges can be aligned or staggered by half a pitch in the transverse direction. The menisci between the ridges were considered to be flat and adiabatic. The solid-liquid interface and the menisci were subjected to no-slip and no-shear boundary conditions, respectively. Using separation of variables, we expressed the three-dimensional temperature field as an infinite sum of the product of an exponentially decaying function of the streamwise coordinate and a second eigenfunction depending on the transverse coordinates. The latter eigenfunctions satisfy a two-dimensional Sturm-Liouville problem from which the eigenvalues and eigenfunctions follow numerically.

The derived expressions for the local Nusselt number, the Nusselt number averaged over the composite interface and the Nusselt number averaged over the composite interface and the streamwise length of the domain, indicate that the Nusselt number is a function of the dimensionless streamwise coordinate, the aspect ratio of the domain, the solid fraction and the inlet temperature profile. Expressions were also derived for the fully developed local Nusselt number and for the fully developed Nusselt number averaged over the composite interface in terms of the first eigenfunction and of the first eigenvalue, respectively.

The results indicate that the Nusselt number decreases as the aspect ratio and/or the solid fraction decrease. Moreover, it was observed that when one plate is adiabatic, the configuration where the adiabatic plate is smooth provides a higher Nusselt number than when it is textured. Finally, using the present analysis, the fully developed local Nusselt number and the fully developed Nusselt number averaged over the composite interface, can be computed in a small fraction of the time that is required by a general computational fluid dynamics (CFD) solver. More importantly, the analysis provides semi-analytical expressions to evaluate the Nusselt number averaged over the composite interface and, additionally, the streamwise length of the domain at any location, quantities which are prohibitively expensive to compute using a general CFD code.

Nomenclature

Roman Symbols

a	half meniscus width, m
c_i	expansion coefficients
D	Domain
d	half ridge pitch, m
∂D	boundary of the dimensionless domain
D_{h}	Hydraulic diameter; $2H$
$\mathrm{d}p/\mathrm{d}z$	prescribed pressure gradient, Pa/m
$\tilde{d}$	dimensionless half ridge pitch; d/a
f	friction factor; $2D_{\mathrm{h}}\left(-\mathrm{d}p/\mathrm{d}z\right)/\left(\rho\overline{w}^2\right)$
$f\mathrm{Re}$	Poiseuille number
H	distance between parallel plates, m
h_{l}	local heat transfer coefficient,W/(m^2 K)
$\tilde{H}$	dimensionless distance between parallel plates; H/a
k	thermal conductivity of liquid, W/(m K)
$\hat{\mathrm{n}}$	outward pointing unit normal vector on boundaries

Nu	Nusselt number averaged over the composite interface
Nu_l	local Nusselt number, $h_\mathrm{l} D_\mathrm{h}/k$
$\overline{\mathrm{Nu}}$	Nusselt number averaged over the composite interface and the streamwise length of the domain
Pe	Péclet number; $\overline{w} D_\mathrm{h}/\alpha$
R	average velocity ratio close to the ridge; $\left(2\int_0^{\tilde{H}/2}\int_0^{\tilde{d}} \tilde{w}\,\mathrm{d}\tilde{x}\,\mathrm{d}\tilde{y}\right)/\left(\tilde{d}\tilde{H}\overline{\tilde{w}}\right)$
Re	Reynolds number; $\rho \overline{w} D_\mathrm{h}/\mu$
$\tilde{S}$	dimensionless coordinate along ∂D
T	temperature, °C
T_in	inlet temperature, °C
T_ref	reference temperature, °C
T_sl	ridge temperature, °C
$\tilde{T}$	dimensionless temperature; $\left(T - T_\mathrm{sl}\right)/\left(T_\mathrm{in} - T_\mathrm{sl}\right)$
$\tilde{T}_\mathrm{in}$	dimensionless inlet temperature
T_b	bulk temperature
$\tilde{T}_\mathrm{b}$	dimensionless bulk temperature
w	streamwise velocity, m/s
$\overline{w}$	mean velocity
$\overline{w}$	mean velocity
$\tilde{w}$	dimensionless velocity; $2\mu w/\left[aH\left(-\mathrm{d}p/\mathrm{d}z\right)\right]$
$\overline{\tilde{w}}$	dimensionless mean velocity
x	lateral coordinate, m
$\tilde{x}$	dimensionless lateral coordinate; x/a

y	vertical coordinate, m
$\tilde{y}$	dimensionless vertical coordinate; y/a
z	streamwise coordinate, m
z^*	dimensionless streamwise coordinate for the thermal entrance region; $z/(D_\mathrm{h}\mathrm{Pe})$
$\tilde{z}$	dimensionless streamwise coordinate; $2\alpha\mu z/\left[a^3 H\left(-\mathrm{d}p/\mathrm{d}z\right)\right]$

Greek Symbols

α	thermal diffusivity, m^2/s
λ_i	i-th eigenvalue
μ	dynamic viscosity, $\mathrm{Pa}\cdot\mathrm{s}$
ϕ	solid fraction; $(d-a)/d$
ψ_i	i-th eigenfunction
ρ	density, kg/m^3

Subscripts

al	textured plates with aligned ridges
fd	fully developed flow
if	isoflux ridges
ridge	indicates quantity based on the width of the ridge
$\mathrm{t}-\mathrm{s}$	one textured and one smooth plate
UIT	uniform inlet temperature

Part III

Extended Graetz-Nusselt Problem for Liquid Flow in Cassie State Over Isothermal Parallel Ridges

Chapter 8

Introduction

A sessile droplet on a structured surface characterized by small periodic length scales compared to the capillary length may be stable in the Cassie state [10, 11] where solid–liquid contact is exclusively at the tips of the structures. A liquid flowing through a microchannel with structured surfaces may be as well and the necessary criteria are provided by Lam *et al.* [8]. Then, a mixed boundary condition of no-slip [12, 13] and low-shear applies along the solid-liquid and the liquid-gas[1] interfaces (menisci), respectively. The low-shear boundary condition provides a lubrication effect and thus reduces both the hydrodynamic resistance and the caloric part of the thermal resistance. However, the reduction in the solid-liquid interfacial area reduces the available area for heat transfer and thus increases the convective part of the thermal resistance. A net reduction of the total, i.e., caloric plus convective, thermal resistance can be achieved with proper sizing of the structures [8] and it requires the knowledge of the Nusselt number (Nu). Such Nusselt numbers are especially relevant to direct liquid cooling applications [8] as per Fig. 8.1 that depicts a structured microchannel etched into the upper portion of a microprocessor die.

The channel surfaces can be textured with a variety of periodic structures such as pillars, transverse ridges, or parallel ridges [9]. The latter configuration is examined here since it is more favorable from a heat transfer perspective [8, 14]. The hydrodynamic effects of structured surfaces with parallel ridges in parallel plate channels have been studied for flat and curved menisci[15, 16, 33, 18, 19, 17, 34, 35]. In terms of the heat transfer effects, Enright *et al.* [14] derived an expression for the Nusselt number for fully-developed flow through a microchannel with isoflux structured surfaces as a function of the apparent hydrodynamic

---

[1] In general the cavities beneath the menisci are filled with inert gas and vapor on account of the vapor pressure of the liquid phase and for brevity we refer to this mixture as “gas”.

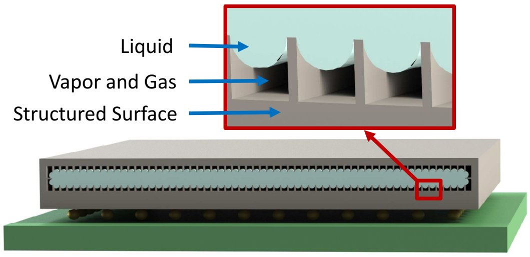

Figure 8.1: Depiction of a structured microchannel etched into the upper portion of a microprocessor die.

and thermal slip lengths. Their analysis applies to both symmetrically and asymmetrically heated channels with large plate spacing to structure pitch ratio. Enright *et al.* [14] too developed analytical expressions for apparent slip lengths for structured surfaces with parallel or transverse ridges or pillar arrays assuming flat and adiabatic menisci. Ng and Wang [20] derived semi-analytical expressions for the apparent thermal slip length for isothermal parallel ridges while accounting for conduction through the gas phase. Lam *et al.* [21] derived expressions for the apparent thermal slip length for isoflux and isothermal parallel ridges accounting for small meniscus curvature. Hodes *et al.* [22] captured the effects of evaporation and condensation along menisci on the apparent thermal slip length for isoflux ridges. Lam *et al.* [23] developed expressions for the Nusselt number for thermally developing Couette flow as a function of apparent slip lengths for various boundary conditions. Also, Lam *et al.* [23] discuss when Nu results accounting for molecular slip can be used to capture the effects of apparent slip. Maynes & Crockett [26] developed expressions for the Nusselt number and the thermal slip length for microchannels with isoflux parallel ridges assuming flat menisci and using the Navier slip approximation for the velocity profile. Kirk *et al.* [6] also developed expressions for the Nusselt number for this configuration, but without invoking the Navier slip approximation. Kirk *et al.* [6] also accounted for small meniscus curvature using a boundary perturbation method. Karamanis *et al.* [3] developed expressions for the Nusselt number for the case of isothermal parallel ridges for hydrodynamically-developed and thermally-developing flow with negligible axial conduction, i.e., for the Graetz-Nusselt problem [28, 29, 30].

The present work extends the analysis in [3] to the case of flow with finite axial conduction, i.e., to the Extended Graetz-Nusselt problem [36, 37, 38]. Viscous dissipation [39, 40] and (uniform) volumetric heat generation [41] are also captured. The menisci are assumed to be flat [21] and adiabatic. The configurations for the isothermal ridges are either both

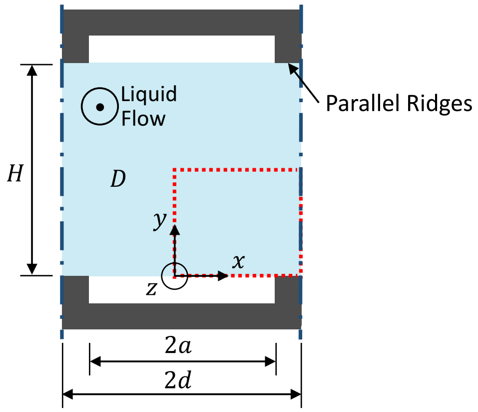

Figure 8.2: Schematic of the periodic domain when both plates are textured; the computational domain is indicated with red line.

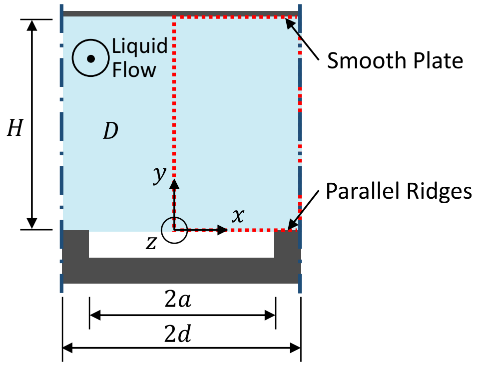

Figure 8.3: Schematic of the periodic domain when one plate is textured with isothermal ridges and the other one is smooth and adiabatic; the computational domain is indicated with red line.

plates textured, as per Fig. 8.2, or one plate textured and the other one smooth and adiabatic, as per Fig 8.3. The solution approach is similar in both configurations. It therefore suffices to present the detailed analysis for the first configuration. The second configuration is considered in Appendix A.

The cross-sectional view of one period of the domain (D) considered is depicted in Fig. 8.2 where it is colored in light blue. It extends from minus to plus infinity in the streamwise direction z, and $|x| \leq d$ and $0 \leq y \leq H$, where $2d$ is the pitch of the ridges and H is the distance between the ridge tips on opposing plates. The hydraulic diameter of the domain (D_h) is $2H$. The width of the meniscus is $2a$. The triple contact lines coincide with the corners of the ridges at $|x| = a$ at both $y = 0$ and $y = H$. Along the composite interfaces at $y = 0$ and $y = H$, a no-shear boundary condition applies for $|x| < a$ and a no-slip one is imposed for $a < |x| < d$ [12, 13]. Symmetry boundary conditions apply along the boundaries at $x = |d|$. The temperature of the ridges is $T_{\mathrm{r}-}$ and $T_{\mathrm{r}+}$ for $z \leq 0$ and $z > 0$, respectively. The flow is pressure driven, steady, laminar, hydrodynamically developed, and thermally developing with constant thermophysical properties. The temperature profile becomes uniform throughout the cross-section as $z \to -\infty$ and $z \to +\infty$, where it is $T_{\mathrm{r}-}$ and $T_{\mathrm{r}+}$, respectively. Effects due to Marangoni stresses [31, 32], evaporation and condensation [22], and gas diffusion in the liquid phase are neglected. The independent dimensionless geometric variables are the solid fraction of the ridge, $\phi = (d - a)/d$, and the aspect ratio of the domain, H/d. Finally, the analysis utilizes the symmetry of the domain with respect to the yz and zx planes through $x = 0$ and $y = H/2$, respectively, and therefore we further restrict to $0 \leq x \leq d$ and $0 \leq y \leq H/2$.

Chapter 9

Analysis

9.1 Hydrodynamic Problem

Assuming hydrodynamically-developed laminar flow with constant thermophysical properties, the streamwise-momentum equation takes the form

$$\nabla^2 w = \frac{1}{\mu}\frac{\mathrm{d}p}{\mathrm{d}z} \tag{9.1}$$

where w is the streamwise velocity, μ is the dynamic viscosity and $\mathrm{d}p/\mathrm{d}z$ is the prescribed (constant) pressure gradient. Denoting nondimensional variables with tildes, Eq. (9.1) is rendered dimensionless by defining

$$\tilde{x} = \frac{x}{D_\mathrm{h}} \tag{9.2}$$

$$\tilde{y} = \frac{y}{D_\mathrm{h}} \tag{9.3}$$

$$\tilde{w} = \frac{\mu}{D_\mathrm{h}^2}\left(-\frac{\mathrm{d}p}{\mathrm{d}z}\right)^{-1} w \tag{9.4}$$

It becomes

$$\nabla^2 \tilde{w} = -1 \tag{9.5}$$

subjected to

$$\frac{\partial \tilde{w}}{\partial \tilde{y}} = 0 \quad \text{for } 0 < \tilde{x} < \tilde{a},\ \tilde{y} = 0 \tag{9.6}$$

$$\tilde{w} = 0 \quad \text{for } \tilde{a} < \tilde{x} < \tilde{d},\ \tilde{y} = 0 \tag{9.7}$$

$$\frac{\partial \tilde{w}}{\partial \tilde{y}} = 0 \quad \text{for } 0 < \tilde{x} < \tilde{d},\ \tilde{y} = 1/4 \tag{9.8}$$

$$\frac{\partial \tilde{w}}{\partial \tilde{x}} = 0 \quad \text{for } \tilde{x} = 0,\ \tilde{x} = \tilde{d},\ 0 < \tilde{y} < 1/4 \tag{9.9}$$

where $\tilde{d} = d/D_\mathrm{h}$ and $\tilde{a} = a/D_\mathrm{h}$ are the dimensionless (half) pitch of the ridges and width of the meniscus, respectively. This hydrodynamic problem has been studied analytically [35], semi-analytically [18, 34] and numerically [33] in the past. Here, we solve it numerically (see Appendix B) to facilitate the solution of the thermal energy equation.

To proceed with the formulation of the Nusselt number, we first compute the Poiseuille number $f\mathrm{Re}$ where

$$\mathrm{Re} = \frac{\rho \overline{w} D_\mathrm{h}}{\mu} \tag{9.10}$$

$$f = \frac{2D_\mathrm{h}}{\rho \overline{w}^2}\left(-\frac{\mathrm{d}p}{\mathrm{d}z}\right) \tag{9.11}$$

$$\overline{w} = \frac{2}{dH}\int_0^{H/2}\int_0^{d} w\,\mathrm{d}x\mathrm{d}y \tag{9.12}$$

are the Reynolds number based on hydraulic diameter, the friction factor and the mean velocity of the liquid, respectively, and ρ is the density. Combining Eqs. (9.2)-(9.4) and (9.10)-(9.12), it follows that

$$f\mathrm{Re} = \frac{2}{\overline{\tilde{w}}} \tag{9.13}$$

where

$$\overline{\tilde{w}} = \frac{4}{\tilde{d}}\int_0^{1/4}\int_0^{\tilde{d}} \tilde{w}\,\mathrm{d}\tilde{x}\mathrm{d}\tilde{y} \tag{9.14}$$

is the dimensionless mean velocity of the flow. Henceforth, $\tilde{w}\left(\tilde{x},\tilde{y}\right)$ and thus $f\mathrm{Re}$ are considered to be known given that the hydrodynamic problem can be solved independently from the thermal one.

9.2 Thermal Problem

Capturing axial conduction, viscous dissipation and volumetric heat generation, the relevant form of the thermal energy equation is

$$
\begin{aligned}
\rho c_p w \frac{\partial T}{\partial z} &= k\left(\frac{\partial^2 T}{\partial x^2}+\frac{\partial^2 T}{\partial y^2}+\frac{\partial^2 T}{\partial z^2}\right) \\
&\quad +\mu\left[\left(\frac{\partial w}{\partial x}\right)^2+\left(\frac{\partial w}{\partial y}\right)^2\right]+\dot{q} \qquad (9.15)
\end{aligned}
$$

where T, k and c_p are the temperature, thermal conductivity and specific heat at constant pressure of the liquid, respectively, and $\dot{q}$ is the (constant) volumetric heat generation rate within the liquid.

Next, we introduce the dimensionless streamwise coordinate $\tilde{z}$ and temperature $\tilde{T}$, as per

$$
\begin{aligned}
\tilde{z} &= \frac{z}{\mathrm{Pe} D_{\mathrm{h}}} \qquad (9.16) \\
\tilde{T} &= \frac{T-T_{\mathrm{r}-}}{T_{\mathrm{r}+}-T_{\mathrm{r}-}} \qquad (9.17)
\end{aligned}
$$

respectively, where

$$
\mathrm{Pe} = \mathrm{Re}\mathrm{Pr} \qquad (9.18)
$$

is the Péclet number, i.e., the scale of the ratio of advective to axially-diffusive heat transfer and

$$
\mathrm{Pr} = \frac{c_p \mu}{k} \qquad (9.19)
$$

is the Prandtl number of the liquid. Combining Eqs. (9.2)-(9.4), (9.13) and (9.15)-(9.19), the dimensionless form of the (inhomogeneous) thermal energy equation is

$$
\begin{aligned}
\frac{f\mathrm{Re}}{2}\tilde{w}\frac{\partial \tilde{T}}{\partial \tilde{z}} &= \frac{\partial^2 \tilde{T}}{\partial \tilde{x}^2}+\frac{\partial^2 \tilde{T}}{\partial \tilde{y}^2}+\frac{1}{\mathrm{Pe}^2}\frac{\partial^2 \tilde{T}}{\partial \tilde{z}^2} \\
&+ \frac{\mathrm{Br}\left(f\mathrm{Re}\right)^2}{4}\left[\left(\frac{\partial \tilde{w}}{\partial \tilde{x}}\right)^2+\left(\frac{\partial \tilde{w}}{\partial \tilde{y}}\right)^2\right]+\tilde{\dot{q}} \qquad (9.20)
\end{aligned}
$$

where

$$
\begin{aligned}
\mathrm{Br} &= \frac{\mu \overline{w}^2}{k\left(T_{\mathrm{r}+}-T_{\mathrm{r}-}\right)} \qquad (9.21) \\
\tilde{\dot{q}} &= \frac{\dot{q} D_{\mathrm{h}}^2}{k\left(T_{\mathrm{r}+}-T_{\mathrm{r}-}\right)} \qquad (9.22)
\end{aligned}
$$

are the Brinkman number and the dimensionless heat generation rate. It is subjected to the following boundary conditions

$$\frac{\partial \tilde{T}}{\partial \tilde{y}} = 0 \quad \text{for } 0 < \tilde{x} < \tilde{a},\ \tilde{y} = 0 \tag{9.23}$$

$$\tilde{T} = 0 \quad \text{for } \tilde{a} < \tilde{x} < \tilde{d},\ \tilde{y} = 0,\ \tilde{z} \leq 0 \tag{9.24}$$

$$\tilde{T} = 1 \quad \text{for } \tilde{a} < \tilde{x} < \tilde{d},\ \tilde{y} = 0,\ \tilde{z} > 0 \tag{9.25}$$

$$\frac{\partial \tilde{T}}{\partial \tilde{y}} = 0 \quad \text{for } 0 < \tilde{x} < \tilde{d},\ \tilde{y} = 1/4 \tag{9.26}$$

$$\frac{\partial \tilde{T}}{\partial \tilde{x}} = 0 \quad \text{for } \tilde{x} = 0,\ \tilde{x} = \tilde{d},\ 0 < \tilde{y} < 1/4 \tag{9.27}$$

$$\tilde{T} = 0 \quad \text{for } 0 < \tilde{x} < \tilde{d},\ 0 < \tilde{y} < 1/4,\ \tilde{z} \to -\infty \tag{9.28}$$

$$\tilde{T} = 1 \quad \text{for } 0 < \tilde{x} < \tilde{d},\ 0 < \tilde{y} < 1/4,\ \tilde{z} \to +\infty \tag{9.29}$$

The dimensionless temperature field is decomposed as

$$\tilde{T} = \tilde{T}_{\mathrm{h}} + \tilde{T}_{\mathrm{p}} \tag{9.30}$$

where $\tilde{T}_{\mathrm{h}}\left(\tilde{x}, \tilde{y}, \tilde{z}, H/d, \phi, \mathrm{Pe}\right)$ and $\tilde{T}_{\mathrm{p}}\left(\tilde{x}, \tilde{y}, H/d, \phi, \mathrm{Br}, \tilde{q}\right)$ are the homogeneous and particular solutions, respectively. Thus, $\tilde{T}_{\mathrm{h}}$ satisfies the homogeneous form of Eq. (9.20), with viscous dissipation and heat generation absent, and $\tilde{T}_{\mathrm{p}}$ satisfies Eq. (9.20) but with homogeneous boundary conditions.

9.2.1 Homogeneous Solution

Here we consider the homogeneous form of Eq. (9.20), i.e., Br and $\tilde{q}$ are set to zero. We seek solutions of the form

$$\tilde{T}_{\mathrm{h}}\left(\tilde{x}, \tilde{y}, \tilde{z}\right) = \begin{cases} \psi_{-}\left(\tilde{x}, \tilde{y}\right) g_{-}\left(\tilde{z}\right) & \text{for } \tilde{z} \leq 0 \\ 1 - \psi_{+}\left(\tilde{x}, \tilde{y}\right) g_{+}\left(\tilde{z}\right) & \text{for } \tilde{z} > 0 \end{cases} \tag{9.31}$$

which separate the dependence of $\tilde{T}$ on the streamwise coordinate $\tilde{z}$ from that on the transverse coordinates $\tilde{x}$ and $\tilde{y}$. It follows that

$$g_{\pm}\left(\tilde{z}\right) = \exp(\text{-}\lambda_{\pm}\tilde{z}) \tag{9.32}$$

and $\psi_{\pm}\left(\tilde{x}, \tilde{y}\right)$ satisfies

$$\nabla^2\psi_\pm = -\lambda_\pm\left(\frac{f\mathrm{Re}}{2}\tilde{w}+\frac{\lambda_\pm}{\mathrm{Pe}^2}\right)\psi_\pm \tag{9.33}$$

subject to the boundary conditions

$$\frac{\partial\psi_\pm}{\partial\tilde{y}} = 0 \quad \text{for } 0<\tilde{x}<\tilde{a},\ \tilde{y}=0 \tag{9.34}$$

$$\psi_\pm = 0 \quad \text{for } \tilde{a}<\tilde{x}<\tilde{d},\ \tilde{y}=0 \tag{9.35}$$

$$\frac{\partial\psi_\pm}{\partial\tilde{y}} = 0 \quad \text{for } 0<\tilde{x}<\tilde{d},\ \tilde{y}=1/4 \tag{9.36}$$

$$\frac{\partial\psi_\pm}{\partial\tilde{x}} = 0 \quad \text{for } \tilde{x}=0,\ \tilde{x}=\tilde{d},\ 0<\tilde{y}<1/4 \tag{9.37}$$

Therefore, (ψ_+,λ_+) and (ψ_-,λ_-) are solutions of the same nonlinear eigenvalue problem, given by Eqs. (9.33)-(9.37). The eigenvalues are real. We assume they are discrete and there are infinitely many and let λ_i and ψ_i denote the i-th eigenvalue and eigenfunction, respectively, ordered such that $-\infty \leftarrow < \cdots < \lambda_{-2} < \lambda_{-1} < 0 < \lambda_1 < \lambda_2 < \cdots \rightarrow +\infty$. Then, the eigensolutions for $\tilde{z}>0$ and $\tilde{z}\le 0$ correspond to those with $\lambda_i>0$ and $\lambda_i<0$, respectively, so that there is exponential decay in the upstream ($\tilde{z}\rightarrow-\infty$) and downstream ($\tilde{z}\rightarrow+\infty$) directions. The set of ψ_i and λ_i are determined numerically (see Appendix B) and henceforth assumed to be known.

We proceed by expressing the general homogeneous solution $\tilde{T}_\mathrm{h}(\tilde{x},\tilde{y},\tilde{z})$ as a linear combination of the appropriate eigenfunctions in each region, i.e.,

$$\tilde{T}_\mathrm{h}(\tilde{x},\tilde{y},\tilde{z}) = \begin{cases} \sum\limits_{i=-\infty}^{-1} c_i\psi_i(\tilde{x},\tilde{y})\exp(-\lambda_i\tilde{z}) & \text{for } \tilde{z}\le 0 \\ 1-\sum\limits_{i=1}^{+\infty} c_i\psi_i(\tilde{x},\tilde{y})\exp(-\lambda_i\tilde{z}) & \text{for } \tilde{z}>0 \end{cases} \tag{9.38}$$

The expansion coefficients c_i follow from the requirement that both temperature and heat flux are continuous at $\tilde{z}=0$, for $0<\tilde{x}<\tilde{d}$ and $0<\tilde{y}<1/4$, i.e.,

$$\lim_{\tilde{z}\rightarrow 0^-}\tilde{T}_\mathrm{h} = \lim_{\tilde{z}\rightarrow 0^+}\tilde{T}_\mathrm{h} \tag{9.39}$$

$$\lim_{\tilde{z}\rightarrow 0^-}\frac{\partial\tilde{T}_\mathrm{h}}{\partial\tilde{z}} = \lim_{\tilde{z}\rightarrow 0^+}\frac{\partial\tilde{T}_\mathrm{h}}{\partial\tilde{z}} \tag{9.40}$$

Substituting Eq. (9.38) in Eqs. (9.39) and (9.40), the latter become, respectively

$$\sum_{i=-\infty, i\neq 0}^{+\infty} c_i \psi_i = 1 \tag{9.41}$$

$$\sum_{i=-\infty, i\neq 0}^{+\infty} c_i \lambda_i \psi_i = 0 \tag{9.42}$$

Given that the eigenvalue problem is nonlinear, we lack a natural orthogonality condition for the eigenfunctions ψ_i. Therefore, we modify the analysis by Deavours [37] to derive an orthogonality condition, to enable us to determine the expansion coefficients from Eqs. (9.41) and (9.42). First, we multiply both sides of the equation for the i-th eigenvalue by $\lambda_j \psi_j$ to give

$$\lambda_j \psi_j \nabla^2 \psi_i = -\lambda_j \psi_j \lambda_i \left(\frac{f\mathrm{Re}}{2} \tilde{w} + \frac{\lambda_i}{\mathrm{Pe}^2} \right) \psi_i \tag{9.43}$$

Interchanging i and j in Eq. (9.43) and subtracting the result from Eq. (9.43), it follows that

$$\lambda_j \psi_j \nabla^2 \psi_i - \lambda_i \psi_i \nabla^2 \psi_j = \frac{\lambda_i \lambda_j}{\mathrm{Pe}^2} \left(\lambda_j - \lambda_i \right) \psi_i \psi_j \tag{9.44}$$

Using the identity

$$\psi_j \nabla^2 \psi_i = \nabla \cdot (\psi_j \nabla \psi_i) - \nabla \psi_j \cdot \nabla \psi_i \tag{9.45}$$

Eq. (9.44) can be rewritten

$$\lambda_j \nabla \cdot (\psi_j \nabla \psi_i) - \lambda_i \nabla \cdot (\psi_i \nabla \psi_j) = (\lambda_j - \lambda_i) \left(\frac{\lambda_i \lambda_j}{\mathrm{Pe}^2} \psi_i \psi_j + \nabla \psi_i \cdot \nabla \psi_j \right) \tag{9.46}$$

Integrating Eq. (9.46) over the domain yields

$$\begin{aligned} \lambda_j \int_0^{1/4} \int_0^{\tilde{d}} \nabla \cdot (\psi_j \nabla \psi_i) \, \mathrm{d}\tilde{x} \mathrm{d}\tilde{y} - \lambda_i \int_0^{1/4} \int_0^{\tilde{d}} \nabla \cdot (\psi_i \nabla \psi_j) \, \mathrm{d}\tilde{x} \mathrm{d}\tilde{y} &= \\ (\lambda_j - \lambda_i) \int_0^{1/4} \int_0^{\tilde{d}} \left(\frac{\lambda_i \lambda_j}{\mathrm{Pe}^2} \psi_i \psi_j + \nabla \psi_i \cdot \nabla \psi_j \right) \mathrm{d}\tilde{x} \mathrm{d}\tilde{y} & \end{aligned} \tag{9.47}$$

However, employing the Divergence Theorem and utilizing Eqs. (9.34)-(9.37), we can show that

$$\int_0^{1/4} \int_0^{\tilde{d}} \nabla \cdot (\psi_i \nabla \psi_j) \, \mathrm{d}\tilde{x} \mathrm{d}\tilde{y} = 0 \tag{9.48}$$

Hence, from Eq. (9.48) and given that $\lambda_j \neq \lambda_i$, Eq. (9.47) yields

$$\int_0^{1/4}\int_0^{\tilde{d}}\left(\frac{\lambda_i\lambda_j}{\mathrm{Pe}^2}\psi_i\psi_j+\nabla\psi_i\cdot\nabla\psi_j\right)\mathrm{d}\tilde{x}\mathrm{d}\tilde{y}=0,\ \ i\neq j \tag{9.49}$$

or, in vector notation,

$$\int_0^{1/4}\int_0^{\tilde{d}}\begin{bmatrix}\lambda_i\psi_i\\ \partial\psi_i/\partial\tilde{x}\\ \partial\psi_i/\partial\tilde{y}\end{bmatrix}^T\begin{bmatrix}\frac{1}{\mathrm{Pe}^2}&0&0\\ 0&1&0\\ 0&0&1\end{bmatrix}\begin{bmatrix}\lambda_j\psi_j\\ \partial\psi_j/\partial\tilde{x}\\ \partial\psi_j/\partial\tilde{y}\end{bmatrix}\mathrm{d}\tilde{x}\mathrm{d}\tilde{y}\quad=\quad 0 \tag{9.50}$$

Thus, the required orthogonality condition is that the vectors $[\lambda_i\psi_i,\partial\psi_i/\partial\tilde{x},\partial\psi_i/\partial\tilde{y}]^T$ and $[\lambda_j\psi_j,\partial\psi_j/\partial\tilde{x},\partial\psi_j/\partial\tilde{y}]^T$ are orthogonal with respect to the matrix

$$\mathbf{B}=\begin{bmatrix}\frac{1}{\mathrm{Pe}^2}&0&0\\ 0&1&0\\ 0&0&1\end{bmatrix} \tag{9.51}$$

With this orthogonality relation, we can now proceed to compute the expansion coefficients c_i. We multiply each vector $[\lambda_j\psi_j,\partial\psi_j/\partial\tilde{x},\partial\psi_j/\partial\tilde{y}]^T$ by the corresponding expansion coefficient c_j and sum the resulting expressions over all indices j. Then, it follows from Eq. (9.42) that

$$\sum_{j=-\infty,j\neq 0}^{+\infty}c_j\begin{bmatrix}\lambda_j\psi_j\\ \partial\psi_j/\partial\tilde{x}\\ \partial\psi_j/\partial\tilde{y}\end{bmatrix}\quad=\quad\sum_{j=-\infty,j\neq 0}^{+\infty}c_j\begin{bmatrix}0\\ \partial\psi_j/\partial\tilde{x}\\ \partial\psi_j/\partial\tilde{y}\end{bmatrix} \tag{9.52}$$

Next, taking the dot product of both sides of Eq. (9.52) with the vector $\mathbf{B}\,[\lambda_i\psi_i,\partial\psi_i/\partial\tilde{x},\partial\psi_i/\partial\tilde{y}]^T$ and integrating the resulting expression over the domain, it follows that

$$\begin{aligned}\int_0^{1/4}\int_0^{\tilde{d}}\sum_{j=-\infty,j\neq 0}^{+\infty}c_j\left(\frac{\lambda_j\lambda_i}{\mathrm{Pe}^2}\psi_j\psi_i+\nabla\psi_j\cdot\nabla\psi_i\right)\mathrm{d}\tilde{x}\mathrm{d}\tilde{y}\quad&=\\ \int_0^{1/4}\int_0^{\tilde{d}}\sum_{j=-\infty,j\neq 0}^{+\infty}c_j\left(\nabla\psi_j\cdot\nabla\psi_i\right)\mathrm{d}\tilde{x}\mathrm{d}\tilde{y}&\end{aligned} \tag{9.53}$$

Switching the order of integration and summation on the left-hand side of Eq. (9.53) and employing Eq. (9.49), yields

$$\begin{aligned}c_i\int_0^{1/4}\int_0^{\tilde{d}}\left(\frac{\lambda_i^2}{\mathrm{Pe}^2}\psi_i^2+\nabla\psi_i\cdot\nabla\psi_i\right)\mathrm{d}\tilde{x}\mathrm{d}\tilde{y}\quad&=\\ \int_0^{1/4}\int_0^{\tilde{d}}\sum_{j=-\infty,j\neq 0}^{+\infty}c_j\left(\nabla\psi_j\cdot\nabla\psi_i\right)\mathrm{d}\tilde{x}\mathrm{d}\tilde{y}&\end{aligned} \tag{9.54}$$

Then, using Eq. (9.45) (which is valid for $i = j$ as well as $i \neq j$), Eq. (9.54) becomes

$$\begin{aligned} c_i \int_0^{1/4} \int_0^{\tilde{d}} \left[\frac{\lambda_i^2}{\mathrm{Pe}^2} \psi_i^2 + \nabla \cdot (\psi_i \nabla \psi_i) - \psi_i \nabla^2 \psi_i \right] \mathrm{d}\tilde{x}\mathrm{d}\tilde{y} \quad &= \\ \int_0^{1/4} \int_0^{\tilde{d}} \sum_{j=-\infty, j\neq 0}^{+\infty} c_j \left[\nabla \cdot (\psi_j \nabla \psi_i) - \psi_j \nabla^2 \psi_i \right] \mathrm{d}\tilde{x}\mathrm{d}\tilde{y} & \end{aligned} \tag{9.55}$$

Switching the order of integration and summation on the first term of the right-hand side of Eq. (9.55) and employing Eqs. (9.33) and (9.48), yields

$$\begin{aligned} c_i \int_0^{1/4} \int_0^{\tilde{d}} \left(\frac{2\lambda_i}{\mathrm{Pe}^2} + \frac{f\mathrm{Re}}{2} \tilde{w} \right) \psi_i^2 \mathrm{d}\tilde{x}\mathrm{d}\tilde{y} \quad &= \\ \int_0^{1/4} \int_0^{\tilde{d}} \left(\frac{\lambda_i}{\mathrm{Pe}^2} + \frac{f\mathrm{Re}}{2} \tilde{w} \right) \psi_i \left(\sum_{j=-\infty, j\neq 0}^{+\infty} c_j \psi_j \right) \mathrm{d}\tilde{x}\mathrm{d}\tilde{y} & \end{aligned} \tag{9.56}$$

Then, using condition Eq. (9.41), it follows that

$$\begin{aligned} c_i \int_0^{1/4} \int_0^{\tilde{d}} \left(\frac{2\lambda_i}{\mathrm{Pe}^2} + \frac{f\mathrm{Re}}{2} \tilde{w} \right) \psi_i^2 \mathrm{d}\tilde{x}\mathrm{d}\tilde{y} \quad &= \\ \int_0^{1/4} \int_0^{\tilde{d}} \left(\frac{\lambda_i}{\mathrm{Pe}^2} + \frac{f\mathrm{Re}}{2} \tilde{w} \right) \psi_i \mathrm{d}\tilde{x}\mathrm{d}\tilde{y} & \end{aligned} \tag{9.57}$$

Thus, rearranging Eq. (9.57) gives the expansion coefficients as per

$$c_i = \frac{\int_0^{1/4} \int_0^{\tilde{d}} \left[\tilde{w} + 2\lambda_i / \left(f\mathrm{Re}\mathrm{Pe}^2 \right) \right] \psi_i \mathrm{d}\tilde{x}\mathrm{d}\tilde{y}}{\int_0^{1/4} \int_0^{\tilde{d}} \left[\tilde{w} + 4\lambda_i / \left(f\mathrm{Re}\mathrm{Pe}^2 \right) \right] \psi_i^2 \mathrm{d}\tilde{x}\mathrm{d}\tilde{y}} \tag{9.58}$$

Finally, our attention shifts to compute the integral over the ridge of $\partial\psi_i / \partial\tilde{y}|_{\tilde{y}=0}$ that is used later in the formulation of the Nusselt number. Integrating Eq. (9.33) over the domain yields

$$\int_0^{1/4} \int_0^{\tilde{d}} \nabla^2 \psi_i \mathrm{d}\tilde{x}\mathrm{d}\tilde{y} = -\lambda_i \int_0^{1/4} \int_0^{\tilde{d}} \left(\frac{f\mathrm{Re}}{2} \tilde{w} + \frac{\lambda_i}{\mathrm{Pe}^2} \right) \psi_i \mathrm{d}\tilde{x}\mathrm{d}\tilde{y} \tag{9.59}$$

Applying the Divergence Theorem on the left-hand side and utilizing Eqs. (9.34)-(9.37), Eq. (9.59) becomes

$$\int_{\tilde{a}}^{\tilde{d}} \left. \frac{\partial \psi_i}{\partial \tilde{y}} \right|_{\tilde{y}=0} \mathrm{d}\tilde{x} = \lambda_i \int_0^{1/4} \int_0^{\tilde{d}} \left(\frac{f\mathrm{Re}}{2} \tilde{w} + \frac{\lambda_i}{\mathrm{Pe}^2} \right) \psi_i \mathrm{d}\tilde{x}\mathrm{d}\tilde{y} \tag{9.60}$$

9.2.2 Particular Solution

We choose the particular solution to be the solution constant in $\tilde{z}$ of Eq. (9.20) (the inhomogeneous equation) with homogeneous boundary conditions. Viscous dissipation and volumetric heat generation are considered separately and the solutions are superimposed. Therefore, we express the particular solution as

$$\tilde{T}_{\mathrm{p}} = \frac{\mathrm{Br}\,(f\mathrm{Re})^2}{4}\tilde{T}_{\mathrm{p,Br}} + \tilde{q}\tilde{T}_{\mathrm{p},\tilde{\mathrm{q}}} \tag{9.61}$$

The quantity $\tilde{T}_{\mathrm{p,Br}}$ satisfies

$$\nabla^2\tilde{T}_{\mathrm{p,Br}} \quad = \quad -\left|\nabla\tilde{w}\right|^2 \tag{9.62}$$

with boundary conditions

$$\frac{\partial\tilde{T}_{\mathrm{p,i}}}{\partial\tilde{y}} = 0 \qquad \text{for } 0 < \tilde{x} < \tilde{a},\ \tilde{y} = 0 \tag{9.63}$$

$$\tilde{T}_{\mathrm{p,i}} = 0 \qquad \text{for } \tilde{a} < \tilde{x} < \tilde{d},\ \tilde{y} = 0 \tag{9.64}$$

$$\frac{\partial\tilde{T}_{\mathrm{p,i}}}{\partial\tilde{y}} = 0 \qquad \text{for } 0 < \tilde{x} < \tilde{d},\ \tilde{y} = 1/4 \tag{9.65}$$

$$\frac{\partial\tilde{T}_{\mathrm{p,i}}}{\partial\tilde{x}} = 0 \qquad \text{for } \tilde{x} = 0,\ \tilde{x} = \tilde{d},\ 0 < \tilde{y} < 1/4 \tag{9.66}$$

where i = Br. Recall that once the velocity field is computed from Eqs. (9.5)-(9.9) the right-hand side of Eq. (9.62) is known. An important result for the formulation of the Nusselt number follows by combining Eqs. (9.5), (9.45) and (9.62) to show that

$$\nabla^2\tilde{T}_{\mathrm{p,Br}} \quad = \quad -\left[\nabla\cdot(\tilde{w}\nabla\tilde{w}) + \tilde{w}\right] \tag{9.67}$$

Then, integrating both sides of Eq. (9.67) over the domain, applying the divergence theorem utilizing the boundary conditions in Eqs. (9.6)-(9.9) and (9.63)-(9.66), and using Eq. (9.13), it follows that

$$\int_{\tilde{a}}^{\tilde{d}} \left.\frac{\partial\tilde{T}_{\mathrm{p,Br}}}{\partial\tilde{y}}\right|_{\tilde{y}=0} \mathrm{d}\tilde{x} \quad = \quad \frac{\tilde{d}}{2f\mathrm{Re}} \tag{9.68}$$

It follows, from Eqs. (9.20) and (9.61) that $\tilde{T}_{\mathrm{p},\tilde{\mathrm{q}}}$ satisfies

$$\nabla^2\tilde{T}_{\mathrm{p},\tilde{\mathrm{q}}} \quad = \quad -1 \tag{9.69}$$

with boundary conditions given by Eqs. (9.63)-(9.66) where i = $\tilde{\mathrm{q}}$. Comparing Eqs. (9.69) with Eqs. (9.5), it follows that the problem for $\tilde{T}_{\mathrm{p},\tilde{\mathrm{q}}}$ is identical to the hydrodynamic problem.

However, this is not the case for the second configuration considered in Appendix A, where one plate is smooth. Next, integrating both sides of Eq. (9.69) over the domain and applying the divergence theorem utilizing the boundary conditions in Eqs. (9.63)-(9.66), yields

$$\int_{\tilde{a}}^{\tilde{d}} \left.\frac{\partial \tilde{T}_{\mathrm{p},\tilde{\mathrm{q}}}}{\partial \tilde{y}}\right|_{\tilde{y}=0} \mathrm{d}\tilde{x} = \frac{\tilde{d}}{4} \tag{9.70}$$

We note that $\tilde{T}_{\mathrm{p,Br}}$ and $\tilde{T}_{\mathrm{p},\tilde{\mathrm{q}}}$ are only functions of the transverse coordinates, the aspect ratio and the solid fraction of the domain. They are determined numerically (see Appendix C) and for the rest of the analysis they are assumed to be known.

Chapter 10

Nusselt Number

10.1 Local Nusselt Number

The local Nusselt number is defined as

$$\mathrm{Nu}_{l\pm} = \frac{h_{l\pm} D_{\mathrm{h}}}{k} \tag{10.1}$$

where $h_{l\pm}$ is the local heat transfer coefficient for $\tilde{z} > 0$ and $\tilde{z} \leq 0$, respectively. An energy balance at a point along the ridges yields

$$-k \left. \frac{\partial T_-}{\partial y} \right|_{y=0} = h_{l-} \left(T_{\mathrm{r}-} - T_{\mathrm{b}-} \right) \text{ for } z \leq 0 \tag{10.2}$$

$$-k \left. \frac{\partial T_+}{\partial y} \right|_{y=0} = h_{l+} \left(T_{\mathrm{r}+} - T_{\mathrm{b}+} \right) \text{ for } z > 0 \tag{10.3}$$

where $T_{\mathrm{b}\pm}$ is the bulk temperature of the liquid defined as

$$T_{\mathrm{b}\pm} = \frac{2}{dH\overline{w}} \int_0^{H/2} \int_0^d w T_\pm \mathrm{d}x \mathrm{d}y \tag{10.4}$$

Substituting Eqs. (10.2)-(10.4) into Eq. (10.1) yields

$$\mathrm{Nu}_{l-} = \frac{1}{\tilde{T}_{\mathrm{b}-}} \left. \frac{\partial \tilde{T}_-}{\partial \tilde{y}} \right|_{\tilde{y}=0} \text{ for } \tilde{z} \leq 0 \tag{10.5}$$

$$\mathrm{Nu}_{l+} = \frac{1}{\left(\tilde{T}_{\mathrm{b}+} - 1 \right)} \left. \frac{\partial \tilde{T}_+}{\partial \tilde{y}} \right|_{\tilde{y}=0} \text{ for } \tilde{z} > 0 \tag{10.6}$$

where

$$\begin{aligned}\tilde{T}_{\mathrm{b}-} &= \frac{2f\mathrm{Re}}{\tilde{d}} \sum_{i=-\infty}^{-1} c_i \exp\left(-\lambda_i \tilde{z}\right) \int_0^{1/4} \int_0^{\tilde{d}} \tilde{w} \psi_i \mathrm{d}\tilde{x} \mathrm{d}\tilde{y} \\ &+ \tilde{T}_{\mathrm{p,b}}\end{aligned} \tag{10.7}$$

$$\begin{aligned}\tilde{T}_{\mathrm{b}+} &= 1 - \frac{2f\mathrm{Re}}{\tilde{d}} \sum_{i=1}^{+\infty} c_i \exp\left(-\lambda_i \tilde{z}\right) \int_0^{1/4} \int_0^{\tilde{d}} \tilde{w} \psi_i \mathrm{d}\tilde{x} \mathrm{d}\tilde{y} \\ &+ \tilde{T}_{\mathrm{p,b}}\end{aligned} \tag{10.8}$$

are the dimensionless bulk temperatures of the liquid for $\tilde{z} \leq 0$ and $\tilde{z} > 0$, respectively, and

$$\begin{aligned}\tilde{T}_{\mathrm{p,b}} &= \frac{2f\mathrm{Re}}{\tilde{d}} \times \\ & \int_0^{1/4} \int_0^{\tilde{d}} \tilde{w} \left[\frac{\mathrm{Br}\left(f\mathrm{Re}\right)^2}{4} \tilde{T}_{\mathrm{p,Br}} + \tilde{q} \tilde{T}_{\mathrm{p},\tilde{\mathrm{q}}} \right] \mathrm{d}\tilde{x} \mathrm{d}\tilde{y}\end{aligned} \tag{10.9}$$

is the contribution to these quantities from the particular solution.

Thus, from Eqs. (9.30), (9.38), (9.61) and (10.5)-(10.9), it follows that the local Nusselt number is given by

$$\mathrm{Nu}_{l\pm} = \frac{\tilde{d}\left(F_{l,1\pm} \mp F_{l,2}\right)}{2f\mathrm{Re}\left(F_{3\pm} \mp F_4\right)} \tag{10.10}$$

where[1]

$$F_{l,1\pm} = \sum_{i=\pm 1}^{\pm\infty} c_i \exp\left(-\lambda_i \tilde{z}\right) \left.\frac{\partial \psi_i}{\partial \tilde{y}}\right|_{\tilde{y}=0} \tag{10.11}$$

$$F_{l,2} = \frac{\mathrm{Br}\left(f\mathrm{Re}\right)^2}{4} \left.\frac{\partial \tilde{T}_{\mathrm{p,Br}}}{\partial \tilde{y}}\right|_{\tilde{y}=0} + \tilde{q} \left.\frac{\partial \tilde{T}_{\mathrm{p},\tilde{\mathrm{q}}}}{\partial \tilde{y}}\right|_{\tilde{y}=0} \tag{10.12}$$

$$F_{3\pm} = \sum_{i=\pm 1}^{\pm\infty} c_i \exp\left(-\lambda_i \tilde{z}\right) \int_0^{1/4} \int_0^{\tilde{d}} \tilde{w} \psi_i \mathrm{d}\tilde{x} \mathrm{d}\tilde{y} \tag{10.13}$$

$$F_4 = \int_0^{1/4} \int_0^{\tilde{d}} \tilde{w} \left[\frac{\mathrm{Br}\left(f\mathrm{Re}\right)^2}{4} \tilde{T}_{\mathrm{p,Br}} + \tilde{q} \tilde{T}_{\mathrm{p},\tilde{\mathrm{q}}} \right] \mathrm{d}\tilde{x} \mathrm{d}\tilde{y} \tag{10.14}$$

We note that $F_{l,1\pm}$ and $F_{l,2}$ are functions of $\tilde{x}$, but that $F_{3\pm}$ and F_4 are not; therefore, only the former have subscript l. The Nusselt number averaged over the composite interface is

$$\mathrm{Nu}_{\pm} = \frac{1}{d} \int_0^d \mathrm{Nu}_{l\pm} \mathrm{d}x \tag{10.15}$$

---

[1] The notation convention is that the summations in F_- and F_+ are from $-\infty$ to -1 and from 1 to ∞, respectively.

Combining Eqs. (10.10)-(10.15) and utilizing Eqs. (9.60), (9.68) and (9.70) yields

$$\mathrm{Nu}_{\pm} = \frac{F_{1\pm} \mp F_2}{4\left(F_{3\pm} \mp F_4\right)} \tag{10.16}$$

where

$$\begin{aligned} F_{1\pm} &= \sum_{i=\pm 1}^{\pm\infty} \lambda_i c_i \exp\left(-\lambda_i \tilde{z}\right) \times \\ &\quad \int_0^{1/4} \int_0^{\tilde{d}} \left(\tilde{w} + \frac{2\lambda_i}{f\mathrm{RePe}^2}\right) \psi_i \mathrm{d}\tilde{x}\mathrm{d}\tilde{y} \qquad (10.17) \\ F_2 &= \frac{\tilde{d}}{4}\left(\mathrm{Br} + \frac{2\tilde{\dot{q}}}{f\mathrm{Re}}\right) \qquad (10.18) \end{aligned}$$

10.2 Fully-Developed Nusselt Number

In this section our attention shifts to the asymptotic values that the Nusselt number attains in the streamwise direction as a function of the Péclet and Brinkman numbers and the dimensionless volumetric heat generation rate. Two regions can be identified where the Nusselt number does not depend on $\tilde{z}$. First, where aside from geometrical effects, those of Pe are dominant and, secondly, when those of Br and $\tilde{\dot{q}}$ are dominant. First, notice that $F_{l,1\pm}$, $F_{1\pm}$ and $F_{3\pm}$ decay exponentially with increasing $|\tilde{z}|$. Comparing the two leading terms of $F_{\mathrm{l}\pm}$, it follows that when $|\tilde{z}| \gg |\tilde{z}_{\mathrm{Pe}\pm}|$, where

$$\tilde{z}_{\mathrm{Pe}\pm} = \frac{\ln|\lambda_{\pm 2}| - \ln|\lambda_{\pm 1}|}{\left(\lambda_{\pm 2} - \lambda_{\pm 1}\right)} \tag{10.19}$$

$F_{l,1\pm}$, $F_{1\pm}$ and $F_{3\pm}$ can be approximated with their leading term. Next, comparing the leading terms of $F_{1\pm}$ and $F_{3\pm}$ with F_2 and F_4, respectively, it follows that when $|\tilde{z}| \ll \min\left(\left|\tilde{z}_{\mathrm{Br}\pm}\right|, \left|\tilde{z}_{\tilde{\dot{\mathrm{q}}}\pm}\right|\right)$ where

$$\begin{aligned} \tilde{z}_{\mathrm{Br}\pm} &= \frac{1}{\lambda_{\pm 1}} \ln\left(\frac{1}{\mathrm{Br}}\right) \qquad (10.20) \\ \tilde{z}_{\tilde{\dot{\mathrm{q}}}\pm} &= \frac{1}{\lambda_{\pm 1}} \ln\left(\frac{1}{\tilde{\dot{q}}}\right) \qquad (10.21) \end{aligned}$$

respectively, $F_{1\pm} \gg F_2$ and $F_{3\pm} \gg F_4$.

10.2.1 Regions where Pe Effects Are Dominant

From Eqs. (10.10)-(10.14) and (10.16)-(10.18), it follows that when $|\tilde{z}_{\mathrm{Pe}\pm}| \ll |\tilde{z}| \ll \min\left(|\tilde{z}_{\mathrm{Br}\pm}|, \left|\tilde{z}_{\tilde{\mathrm{q}}\pm}\right|\right)$, the fully-developed local Nusselt number ($\mathrm{Nu}_{l,\mathrm{fd,Pe}\pm}$) and the fully-developed Nusselt number averaged over the composite interface ($\mathrm{Nu}_{\mathrm{fd,Pe}\pm}$) are given by

$$\mathrm{Nu}_{l,\mathrm{fd,Pe}\pm} = \frac{\tilde{d}\left.\frac{\partial\psi_{\pm 1}}{\partial\tilde{y}}\right|_{\tilde{y}=0}}{2f\mathrm{Re}\int_0^{1/4}\int_0^{\tilde{d}}\tilde{w}\psi_{\pm 1}\mathrm{d}\tilde{x}\mathrm{d}\tilde{y}} \tag{10.22}$$

and

$$\mathrm{Nu}_{\mathrm{fd,Pe}\pm} = \frac{\lambda_{\pm 1}}{4}\left(1+\frac{2\lambda_{\pm 1}}{f\mathrm{RePe}^2}\frac{\int_0^{1/4}\int_0^{\tilde{d}}\psi_{\pm 1}\mathrm{d}\tilde{x}\mathrm{d}\tilde{y}}{\int_0^{1/4}\int_0^{\tilde{d}}\tilde{w}\psi_{\pm 1}\mathrm{d}\tilde{x}\mathrm{d}\tilde{y}}\right) \tag{10.23}$$

respectively.

10.2.2 Regions where Br and $\tilde{q}$ Effects Are Dominant

When $|\tilde{z}| \gg \max\left(|\tilde{z}_{\mathrm{Br}\pm}|, \left|\tilde{z}_{\tilde{\mathrm{q}}\pm}\right|\right)$ such that the effects of Br and/or $\tilde{q}$ are dominant, the corresponding fully-developed local Nusselt number $\left(\mathrm{Nu}_{l,\mathrm{fd,Br},\tilde{\mathrm{q}}\pm}\right)$ and fully-developed Nusselt number averaged over the composite interface $\left(\mathrm{Nu}_{\mathrm{fd,Br},\tilde{\mathrm{q}}\pm}\right)$ are found to be

$$\mathrm{Nu}_{l,\mathrm{fd,Br},\tilde{\mathrm{q}}\pm} = \frac{\tilde{d}F_{l,2}}{2f\mathrm{Re}F_4} \tag{10.24}$$

and

$$\mathrm{Nu}_{\mathrm{fd,Br},\tilde{\mathrm{q}}\pm} = \frac{F_2}{4F_4} \tag{10.25}$$

respectively.

Equations (10.24) and (10.25) indicate that when $|\tilde{z}| \gg \max\left(|\tilde{z}_{\mathrm{Br}\pm}|, \left|\tilde{z}_{\tilde{\mathrm{q}}\pm}\right|\right)$, the fully-developed Nusselt number is independent of the Péclet number. Moreover, when $\tilde{q} \gg \mathrm{Br}$, Eq. (10.25) becomes

$$\mathrm{Nu}_{\mathrm{fd},\tilde{\mathrm{q}}\pm} = \frac{\tilde{d}}{8f\mathrm{Re}\int_0^{1/4}\int_0^{\tilde{d}}\tilde{w}\tilde{T}_{\mathrm{p},\tilde{\mathrm{q}}}\mathrm{d}\tilde{x}\mathrm{d}\tilde{y}} \tag{10.26}$$

and if $\tilde{q} = 0$, it becomes

$$\mathrm{Nu}_{\mathrm{fd,Br}\pm} \quad = \quad \frac{\tilde{d}}{4\left(f\mathrm{Re}\right)^{2}\int_{0}^{1/4}\int_{0}^{\tilde{d}}\tilde{w}\tilde{T}_{\mathrm{p,Br}}\mathrm{d}\tilde{x}\mathrm{d}\tilde{y}} \tag{10.27}$$

Equations (10.26) and (10.27) state that when volumetric heat generation is either absent or much larger than viscous dissipation, and $|\tilde{z}| \gg |\tilde{z}_{\mathrm{Br}\pm}|$, the fully-developed Nusselt number is a function of the geometry of the domain, but independent of the Péclet and Brinkman numbers.

Chapter 11

Results

This section contains three subsections. The first two consider separately the effects of axial conduction, and of viscous dissipation and volumetric heat generation, respectively, on the fully-developed (local and averaged over the composite interface) Nusselt number. The third one considers the combined effects of axial conduction and viscous dissipation on the developing Nusselt number averaged over the composite interface. The results are for the first configuration of the ridges, and those for the second configuration are presented in Appendix A. When a variable $\left(\mathrm{Pe}, \mathrm{Br}, \tilde{q}\right)$ appears as a subscript of Nu, it signifies that the corresponding physical effects is dominant in that scenario or at that streamwise location. Two subscript variables signifies that both are equally important. Note however that a subscript variable may not appear in the corresponding Nu expression, see for example Eqs. (10.26) and (10.27).

11.1 Effects of Axial Conduction on Fully-Developed Nusselt Number

11.1.1 Effects of ϕ and H/d for $\mathrm{Pe} = 1$

Figures 11.1 and 11.2 plot the fully-developed Nusselt number averaged over the composite interface versus the solid fraction ϕ for aspect ratios of $H/d = 1,\ 2,\ 4,\ 6,\ 10$ and 100, and $\mathrm{Pe} = 1$. They apply when $\min\left(\tilde{z}_{\mathrm{Br}-}, \tilde{z}_{\tilde{\mathrm{q}}-}\right) \ll \tilde{z} \ll \tilde{z}_{\mathrm{Pe}-}$ and $\tilde{z}_{\mathrm{Pe}+} \ll \tilde{z} \ll \min\left(\tilde{z}_{\mathrm{Br}+}, \tilde{z}_{\tilde{\mathrm{q}}+}\right)$, i.e., they provide $\mathrm{Nu}_{\mathrm{fd,Pe}-}$ and $\mathrm{Nu}_{\mathrm{fd,Pe}+}$, respectively. Recall that in this part (when it exists) of the fully-developed region the effects of Br and $\tilde{q}$ on the fully-developed Nusselt number are negligible. The dashed curves correspond to smooth plates

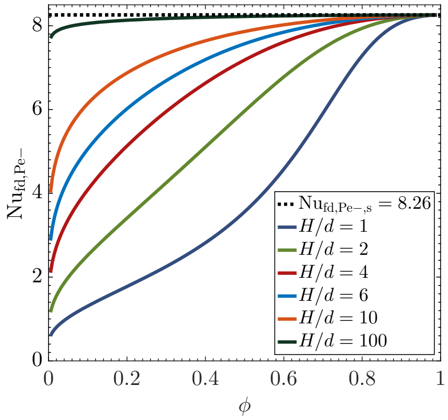

Figure 11.1: $\mathrm{Nu}_{\mathrm{fd,Pe-}}$ vs. ϕ for $\mathrm{Pe} = 1$ and selected H/d when both plates are textured with isothermal ridges.

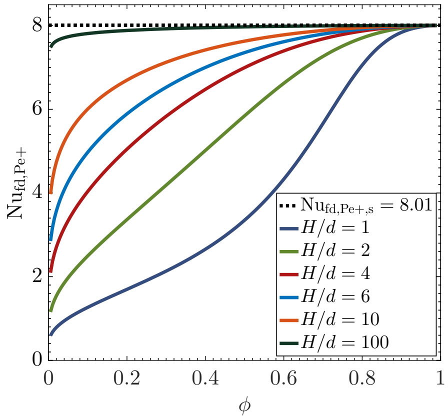

Figure 11.2: $\mathrm{Nu}_{\mathrm{fd,Pe+}}$ vs. ϕ for $\mathrm{Pe} = 1$ and selected H/d when both plates are textured with isothermal ridges.

with Nusselt numbers $\mathrm{Nu}_{\mathrm{fd,Pe-,s}} = 8.26$ and $\mathrm{Nu}_{\mathrm{fd,Pe+,s}} = 8.01$ [38], respectively. This difference between $\mathrm{Nu}_{\mathrm{fd,Pe-}}$ and $\mathrm{Nu}_{\mathrm{fd,Pe+}}$ was also observed by Agrawal [36] for the case of smooth parallel plates. Physically, this is expected since advection prevents symmetry arguments to be used pertaining to the upstream and downstream portions of the domain. Moreover, the difference between the computed $\mathrm{Nu}_{\mathrm{fd,Pe+,s}} = 8.01$ and the corresponding value of 7.54 when $\mathrm{Pe} \to \infty$ is a manifestation of the effects of axial conduction which provides an additional path to heat transfer as discussed in Section 11.1.2.

The results obey the same trends with respect to H/d and ϕ as observed in [3]. In the limit as $\phi \to 1$, $\mathrm{Nu}_{\mathrm{fd,Pe\pm}} \to \mathrm{Nu}_{\mathrm{fd,Pe\pm,s}}$, irrespective of the aspect ratio, as they should. Additionally, as $\phi \to 0$, both $\mathrm{Nu}_{\mathrm{fd,Pe-}}$ and $\mathrm{Nu}_{\mathrm{fd,Pe+}}$ tend to zero because the available

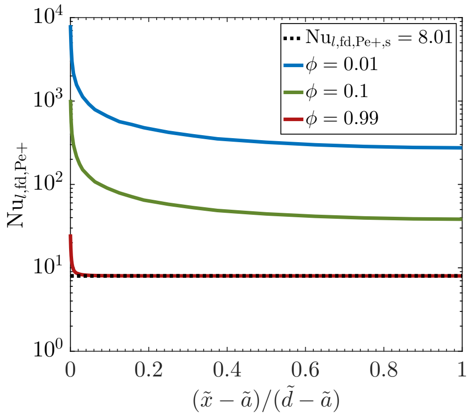

Figure 11.3: $\mathrm{Nu}_{l,\mathrm{fd,Pe+}}$ vs. the normalized coordinate along the ridge $(\tilde{x}-\tilde{a})/\left(\tilde{d}-\tilde{a}\right)$ for $\mathrm{Pe}=1$, $H/d=10$ and selected values of ϕ when both plates are textured with isothermal ridges.

area for heat transfer vanishes. Furthermore, and excluding the aforementioned limits, for fixed ϕ as $H/d \to 0$ and $H/d \to \infty$, both $\mathrm{Nu}_{\mathrm{fd,Pe-}}$ and $\mathrm{Nu}_{\mathrm{fd,Pe+}}$ tend to zero and to their corresponding counterparts for smooth plates, respectively. This is because as $H/d \to 0$ and $H/d \to \infty$, the difference between the temperature of the ridge and the mean temperature of the composite interface becomes significant and negligible, respectively, compared to the difference between the temperature of the ridge and the bulk temperature of the liquid.

Figure 11.3 plots the fully-developed local Nusselt number ($\mathrm{Nu}_{l,\mathrm{fd,Pe+}}$) versus the normalized coordinate along the ridge $(\tilde{x}-\tilde{a})/\left(\tilde{d}-\tilde{a}\right)$ for $\mathrm{Pe}=1$, $H/d=10$ and $\phi=0.01,\ 0.1$ and 0.99. The maximum and minimum values of $\mathrm{Nu}_{l,\mathrm{fd,Pe+}}$ in each case are observed at the triple contact line $(\tilde{x}=\tilde{a})$ and at the center of the ridge $\left(\tilde{x}=\tilde{d}\right)$, respectively. Moreover, $\mathrm{Nu}_{l,\mathrm{fd,Pe+}}$ increases with decreasing ϕ indicating a local enhancement of heat transfer due to the higher velocities of the liquid close to the ridge as $\phi \to 0$. Both trends are consistent with previous studies [25, 3]. In summary, the overall effect of the decrease in the available heat transfer area and the local enhancement of heat transfer for $\phi < 1$ is an increase in the convective portion of the total thermal resistance that is completely captured in Figs. 11.1 and 11.2.

11.1.2 Effects of ϕ and Pe for $H/d = 1$ and 10

Figures 11.4 and 11.5 plot the computed $\mathrm{Nu}_{\mathrm{fd,Pe-}}$ and $\mathrm{Nu}_{\mathrm{fd,Pe+}}$, respectively, versus the solid fraction for $\mathrm{Pe}=0.01,\ 1$ and 10 for $H/d=1$. The latter also includes the $\mathrm{Pe}\to\infty$ limit [3] for comparison. Figures 11.6 and 11.7 apply when $H/d=10$. The results show

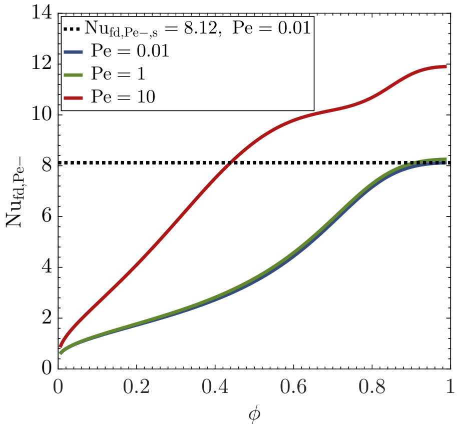

Figure 11.4: $\mathrm{Nu}_{\mathrm{fd,Pe-}}$ vs. ϕ for $\mathrm{Pe} = 0.01,\ 1,\ 10$ and $H/d = 1$ when both plates are textured with isothermal ridges.

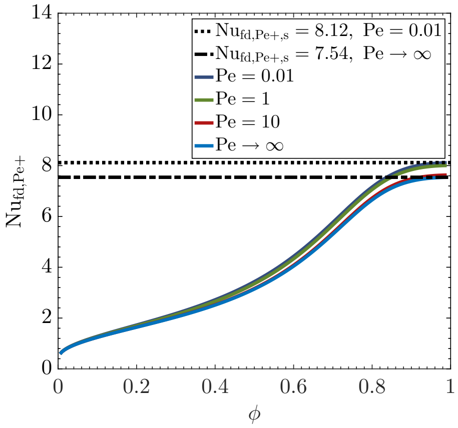

Figure 11.5: $\mathrm{Nu}_{\mathrm{fd,Pe+}}$ vs. ϕ for $\mathrm{Pe} = 0.01,\ 1,\ 10$ and $\mathrm{Pe} \to \infty$, and $H/d = 1$ when both plates are textured with isothermal ridges.

that as $\mathrm{Pe} \to 0$, $\mathrm{Nu}_{\mathrm{fd,Pe-,s}}$ approaches $\mathrm{Nu}_{\mathrm{fd,Pe+,s}}$ and they become approximately equal to 8.12 [38]. This is expected as in this limit the primary mode of heat transfer is conduction and thus the problem becomes antisymmetric with respect to $\tilde{z} = 0$, where $\tilde{T} = 0.5$.

Comparing Figs. 11.4 and 11.6 with Figs. 11.5 and 11.7, respectively, shows that as the Péclet number increases, $\mathrm{Nu}_{\mathrm{fd,Pe-}}$ and $\mathrm{Nu}_{\mathrm{fd,Pe+}}$ respond differently. $\mathrm{Nu}_{\mathrm{fd,Pe-}}$ tends to infinity as Pe increases because the temperature field for $\tilde{z} \leq 0$ becomes essentially isothermal and thus $\tilde{T}_- \to 0$ and $\partial \tilde{T}_- / \partial \tilde{y}\Big|_{\tilde{y}=0} \to 0$. Note that despite the fact that $\mathrm{Nu}_{\mathrm{fd,Pe-}}$ tends to infinity in this case, there is no heat transfer from the ridge to the liquid given that $\partial \tilde{T}_- / \partial \tilde{y}\Big|_{\tilde{y}=0} \to 0$. This behavior is consistent with the trends observed by Agrawal [36] for the case of smooth isothermal plates. Contrary, $\mathrm{Nu}_{\mathrm{fd,Pe+}}$ decreases as Pe increases because

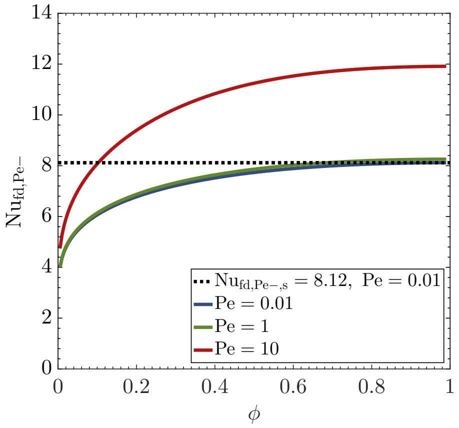

Figure 11.6: $\mathrm{Nu}_{\mathrm{fd,Pe-}}$ vs. ϕ for $\mathrm{Pe} = 0.01,\ 1,\ 10$ and $H/d = 10$ when both plates are textured with isothermal ridges.

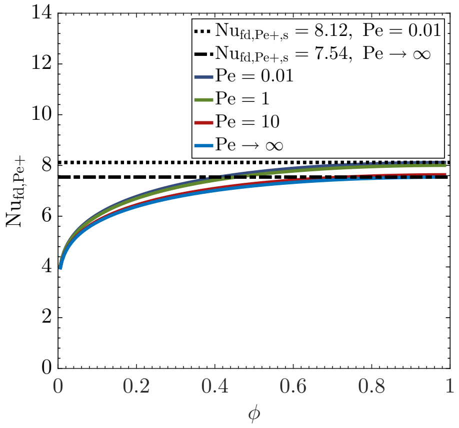

Figure 11.7: $\mathrm{Nu}_{\mathrm{fd,Pe+}}$ vs. ϕ for $\mathrm{Pe} = 0.01,\ 1,\ 10$ and $\mathrm{Pe} \to \infty$, and $H/d = 10$ when both plates are textured with isothermal ridges.

the axial conduction enhancement to heat transfer is reduced, and in the limit $\mathrm{Pe} \to \infty$, $\mathrm{Nu}_{\mathrm{fd,Pe+,s}}$ tends to finite values. These trends are reversed, however, when only one plate is textured with isothermal ridges and the other one is smooth and adiabatic. The slower velocity field in this case causes $\partial \tilde{T}_- / \partial \tilde{y}\Big|_{\tilde{y}=0}$ to tend to zero faster than $\tilde{T}_-$ does [3] and therefore $\mathrm{Nu}_{\mathrm{fd,Pe-}} \to 0$, as $\mathrm{Pe} \to \infty$ as per the corresponding results in Appendix A. Also, the adiabatic boundary condition along the smooth plate leads to convection dominated heat transfer and thus $\mathrm{Nu}_{\mathrm{fd,Pe+}}$ increases as Pe increases with $\mathrm{Nu}_{\mathrm{fd,Pe+}}$ tending to finite values as $\mathrm{Pe} \to \infty$. For both ridge configurations, the change of $\mathrm{Nu}_{\mathrm{fd,Pe-}}$ and $\mathrm{Nu}_{\mathrm{fd,Pe+}}$ for an increase of the Péclet number is small for $\mathrm{Pe} < 1$ as in this region the heat transfer is predominantly diffusive, but the change becomes large when $\mathrm{Pe} > 1$ and advection becomes

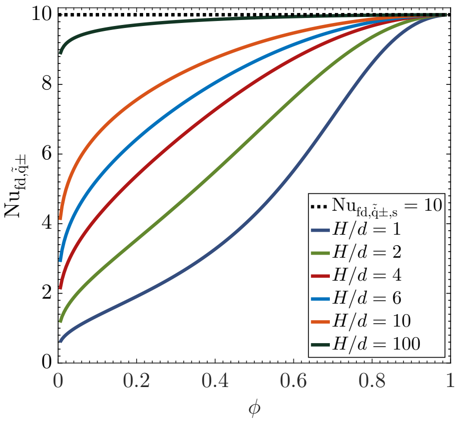

Figure 11.8: $\mathrm{Nu}_{\mathrm{fd},\tilde{\mathrm{q}}\pm}$ vs. ϕ for selected H/d when both plates are textured with isothermal ridges.

important.

Finally, comparing Figs. 11.4 and 11.6 with Figs. 11.5 and 11.7, respectively, it follows that the effects of Péclet number become important as the solid fraction increases and for $\mathrm{Nu}_{\mathrm{fd,Pe+}}$ the range of values of ϕ where change is observed increases with H/d. Moreover, the effects are more pronounced on $\mathrm{Nu}_{\mathrm{fd,Pe-}}$ which, as explained above, has a stronger dependence on Pe than $\mathrm{Nu}_{\mathrm{fd,Pe+}}$.

11.2 Effects of Viscous Dissipation and Volumetric Heat Generation on Fully-Developed Nusselt Number

The computed fully-developed Nusselt numbers averaged over the composite interface when $|\tilde{z}| \gg \max\left(|\tilde{z}_{\mathrm{Br}\pm}|, \left|\tilde{z}_{\tilde{\mathrm{q}}\pm}\right|\right)$, $\mathrm{Nu}_{\mathrm{fd,Br}\pm}$ and $\mathrm{Nu}_{\mathrm{fd},\tilde{\mathrm{q}}\pm}$, are presented in Figs. 11.9 and 11.8, respectively. The results present the same trends with respect to ϕ and H/d as those described for $\mathrm{Nu}_{\mathrm{fd,Pe}\pm}$, i.e., irrespective of H/d as $\phi \to 0$, both $\mathrm{Nu}_{\mathrm{fd,Br}\pm}$ and $\mathrm{Nu}_{\mathrm{fd},\tilde{\mathrm{q}}\pm}$ tend to zero and as $\phi \to 1$, $\mathrm{Nu}_{\mathrm{fd,Br}\pm} \to \mathrm{Nu}_{\mathrm{fd,Br}\pm,\mathrm{s}} = 17.5$[39] and $\mathrm{Nu}_{\mathrm{fd},\tilde{\mathrm{q}}\pm} \to \mathrm{Nu}_{\mathrm{fd},\tilde{\mathrm{q}}\pm,\mathrm{s}} = 10$[41], respectively.

11.3 Combined Effects of Axial Conduction and Viscous Dissipation on Developing Nusselt Number

Here, we present results for the combined effects of the Péclet and Brinkman numbers on the Nusselt number averaged over the composite interface for $\tilde{z} > 0$ (Nu_+). Figure 11.10

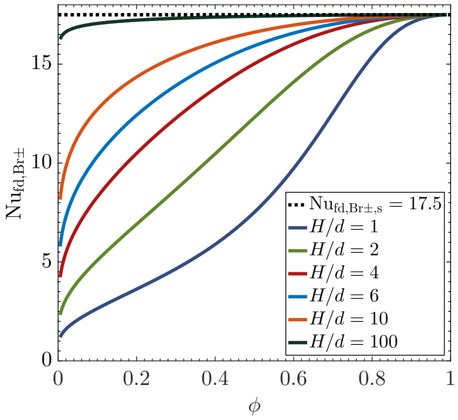

Figure 11.9: $\mathrm{Nu}_{\mathrm{fd,Br}\pm}$ vs. ϕ for selected H/d when both plates are textured with isothermal ridges.

presents Nu_+ versus the dimensionless streamwise coordinate for $\phi = 0.01$, $H/d = 10$, $\mathrm{Pe} = 1$, $\tilde{\tilde{q}} = 0$ and for three different values of the Brinkman number, namely $\mathrm{Br} = 2.71 \times 10^{-5}$, 2.71×10^{-8} and as $\mathrm{Br} \to 0$. The second value of Br is relevant to flow of liquid metals though textured microchannels [8]. In this figure we can identify the two asymptotic values of Nu_+. First, as $\tilde{z}$ increases and becomes larger than $\tilde{z}_{\mathrm{Pe}+}$, Nu_+ approaches $\mathrm{Nu}_{\mathrm{fd,Pe}+} = 4.33$. Then, as $\tilde{z}$ continues to increase, the effects of the step change of the ridge temperature decay significantly and become of the same order as the viscous dissipation effects. Thus, in the region where $\tilde{z} \approx \tilde{z}_{\mathrm{Br}+}$, Nu_+ starts to increase until $\tilde{z} \gg \tilde{z}_{\mathrm{Br}+}$ where $\mathrm{Nu}_+ \to \mathrm{Nu}_{\mathrm{fd,Br}\pm} = 8.92$. Also, as Br increases, the location of the transition moves further upstream but its limiting value remains 8.92. The same trends were reported in [40] for the case of smooth plates. Figure 11.11 presents Nu_+ versus $\tilde{z}$ for the same domain geometry and Br as in Fig. 11.10, but for $\mathrm{Pe} = 10$. Comparing Figs. 11.10 and 11.11 we see that as Pe increases the transitions of Nu_+ to $\mathrm{Nu}_{\mathrm{fd,Pe}+}$ and then to $\mathrm{Nu}_{\mathrm{fd,Br}\pm}$ occur further upstream given that the flow becomes thermally-developed faster with increasing Pe.

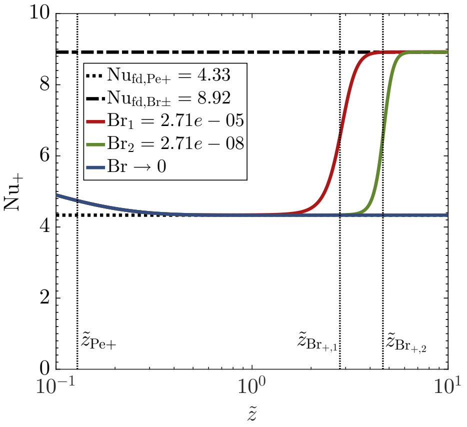

Figure 11.10: Nu$_+$ vs. $\tilde{z}$ for $\phi = 0.01$, $H/d = 10$, Pe $= 1$ and $\tilde{q} = 0$ when both plates are textured with isothermal ridges; $\tilde{z}_{\mathrm{Pe+}} = 0.13$, $\tilde{z}_{\mathrm{Br+,1}} = 2.81$ and $\tilde{z}_{\mathrm{Br+,2}} = 4.65$.

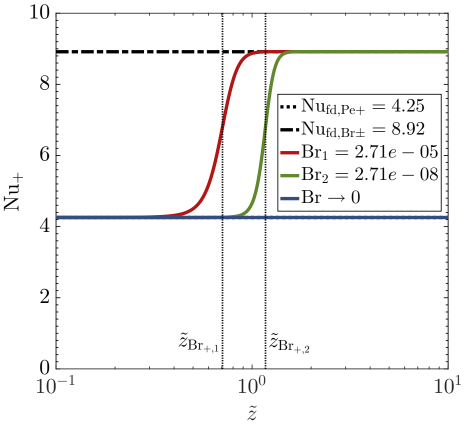

Figure 11.11: Nu$_+$ vs. $\tilde{z}$ for $\phi = 0.01$, $H/d = 10$, Pe $= 10$ and $\tilde{q} = 0$ when both plates are textured with isothermal ridges; $\tilde{z}_{\mathrm{Pe+}} = 0.02$, $\tilde{z}_{\mathrm{Br+,1}} = 0.71$ and $\tilde{z}_{\mathrm{Br+,2}} = 1.17$.

Chapter 12

Conclusions

We considered the Extended Graetz-Nusselt problem, i.e., hydrodynamically-developed and thermally-developing flow with finite axial conduction, for the case of textured plates (or plate) with isothermal parallel ridges. We developed semi-analytical expressions for the Nusselt number in an infinite domain, before and after a jump in ridge temperature. Effects of viscous dissipation and volumetric heat generation were included. Two different configurations for the ridges were analyzed: 1) both plates textured and 2) one plate textured and the other one smooth and adiabatic. The menisci between the ridges were considered to be flat and adiabatic. The solid-liquid interfaces and the menisci were subjected to no-slip and no-shear boundary conditions, respectively. Using separation of variables, we expressed the homogeneous part of the solution as an infinite sum of the product of an exponentially decaying function of the streamwise coordinate and a second eigenfunction depending on the transverse coordinates. The latter eigenfunctions satisfy a two-dimensional non-linear eigenvalue problem from which the eigenvalues and eigenfunctions follow numerically. The particular solution accounting for viscous dissipation and volumetric heat generation is also determined numerically.

The derived expressions for the local Nusselt number and the Nusselt number averaged over the composite interface indicate that the Nusselt number is a function of the transverse (along the ridge) and streamwise coordinates, the aspect ratio of the domain, the solid fraction of the ridges, the Péclet and Brinkman numbers, and the dimensionless volumetric heat generation rate. Expressions were also derived for the fully-developed local Nusselt number and for the fully-developed Nusselt number averaged over the composite interface. Two asymptotic limits were identified for the fully-developed Nusselt number and expressions were derived to estimate the streamwise locations where they occur. The first limit is relevant to the effects of axial conduction, and the corresponding fully-developed Nusselt number is a function of the geometry and the Péclet number. The second limit is relevant to viscous dissipation and volumetric heat generation effects, and the corresponding fully-developed Nusselt number is a function of the geometry, the Brinkman number and the dimensionless volumetric heat generation rate. If volumetric heat generation is absent, the aforementioned Nusselt number is a function of the geometry only.

The results indicate that the Nusselt number averaged over the composite interface decreases as the aspect ratio and/or the solid fraction decreases. Moreover, the fully-developed Nusselt number averaged over the composite interface in the region after the temperature change tends to a finite value as the Péclet number tends to infinity for both geometries studied. On the contrary, in the region before the temperature change, the fully-developed average Nusselt number tends to infinity when both plates are textured with isothermal ridges, and to zero when one plate is smooth and adiabatic, as the Péclet number tends to infinity.

Using the present analysis, the fully-developed local Nusselt number and the fully-developed Nusselt number averaged over the composite interface can be computed in a small fraction of the time that is required by a general computational fluid dynamics (CFD) solver. More importantly, the analysis provides semi-analytical expressions to evaluate the local Nusselt number and the Nusselt number averaged over the composite interface at any location, which are prohibitively expensive to compute using a general CFD code.

Nomenclature

Roman Symbols

a	half meniscus width, m
$\tilde{a}$	dimensionless half meniscus width; a/D_h
$\mathbf{B}$	orthogonality matrix
Br	Brinkman number; $\left(\mu\overline{w}^2\right)/[k\left(T_{\mathrm{r}+}-T_{\mathrm{r}-}\right)]$
c_i	expansion coefficients
c_p	specific heat at constant pressure, J/(kg K)
D	domain
d	half ridge pitch, m
$\tilde{d}$	dimensionless half ridge pitch; d/D_h
D_h	hydraulic diameter; $2H$
$\mathrm{d}p/\mathrm{d}z$	prescribed pressure gradient, Pa/m
f	friction factor; $2D_\mathrm{h}\left(-\mathrm{d}p/\mathrm{d}z\right)/\left(\rho\overline{w}^2\right)$
$f\mathrm{Re}$	Poiseuille number
H	distance between parallel plates, m
h	heat transfer coefficient, W/(m^2 K)

$h_{l\pm}$	local heat transfer coefficient, $\mathrm{W/(m^2\,K)}$
k	thermal conductivity, $\mathrm{W/(m\,K)}$
Nu	Nusselt number; hD_h/k
$\mathrm{Nu}_{l\pm}$	local Nusselt number; $h_{l\pm}D_\mathrm{h}/k$
$\mathrm{Nu}_{\pm}$	Nusselt number averaged over the composite interface; $\int_0^d \mathrm{Nu}_{l\pm}\mathrm{d}x/d$
$\mathrm{Nu}_{l,\mathrm{fd,Pe}\pm}$	fully-developed local Nusselt number when the effects of Br and $\tilde{\dot{q}}$ are negligible, *i.e.*, when $\lvert\tilde{z}_{\mathrm{Pe}\pm}\rvert \ll \lvert\tilde{z}\rvert \ll \min\left(\lvert\tilde{z}_{\mathrm{Br}\pm}\rvert, \left\lvert\tilde{z}_{\tilde{\dot{\mathrm{q}}}\pm}\right\rvert\right)$
$\mathrm{Nu}_{l,\mathrm{fd,Br},\tilde{\dot{\mathrm{q}}}\pm}$	fully-developed local Nusselt number when the effects of Br and $\tilde{\dot{q}}$ are dominant, *i.e.*, when $\lvert\tilde{z}\rvert \gg \max\left(\lvert\tilde{z}_{\mathrm{Br}\pm}\rvert, \left\lvert\tilde{z}_{\tilde{\dot{\mathrm{q}}}\pm}\right\rvert\right)$
$\mathrm{Nu}_{\mathrm{fd,Pe}\pm}$	fully-developed Nusselt number averaged over the composite interface when the effects of Br and $\tilde{\dot{q}}$ are negligible, *i.e.*, when $\lvert\tilde{z}_{\mathrm{Pe}\pm}\rvert \ll \lvert\tilde{z}\rvert \ll \min\left(\lvert\tilde{z}_{\mathrm{Br}\pm}\rvert, \left\lvert\tilde{z}_{\tilde{\dot{\mathrm{q}}}\pm}\right\rvert\right)$
$\mathrm{Nu}_{\mathrm{fd,Br},\tilde{\dot{\mathrm{q}}}\pm}$	fully-developed Nusselt number averaged over the composite interface when the effects of Br and $\tilde{\dot{q}}$ are dominant, *i.e.*, when $\lvert\tilde{z}\rvert \gg \max\left(\lvert\tilde{z}_{\mathrm{Br}\pm}\rvert, \left\lvert\tilde{z}_{\tilde{\dot{\mathrm{q}}}\pm}\right\rvert\right)$
$\mathrm{Nu}_{\mathrm{fd,Br}\pm}$	fully-developed Nusselt number averaged over the composite interface when the effects of Br are dominant, *i.e.*, when $\lvert\tilde{z}\rvert \gg \lvert\tilde{z}_{\mathrm{Br}\pm}\rvert$ and $\mathrm{Br} \gg \tilde{\dot{q}}$
$\mathrm{Nu}_{\mathrm{fd},\tilde{\dot{\mathrm{q}}}\pm}$	fully-developed Nusselt number averaged over the composite interface when the effects of $\tilde{\dot{q}}$ are dominant, *i.e.*, when $\lvert\tilde{z}\rvert \gg \left\lvert\tilde{z}_{\tilde{\dot{\mathrm{q}}}\pm}\right\rvert$ and $\tilde{\dot{q}} \gg \mathrm{Br}$
Pe	Péclet number; RePr
Pr	Prandtl number; $(c_p\mu)/k$
$\dot{q}$	volumetric heat generation rate, $\mathrm{W/m^3}$
$\tilde{\dot{q}}$	dimensionless heat generation rate; $\dot{q}D_\mathrm{h}^2/[k(T_{\mathrm{r}+}-T_{\mathrm{r}-})]$
Re	Reynolds number; $\rho\overline{w}D_\mathrm{h}/\mu$
T	temperature, °C
$\tilde{T}$	dimensionless temperature; $(T-T_{\mathrm{r}-})/(T_{\mathrm{r}+}-T_{\mathrm{r}-})$

$\tilde{T}_{\mathrm{h}}$	homogeneous solution
$\tilde{T}_{\mathrm{p}}$	particular solution
T_{b}	bulk temperature; $2\left(dH\overline{w}\right)^{-1}\int_0^{H/2}\int_0^{d} wT\mathrm{d}x\mathrm{d}y$
$\tilde{T}_{\mathrm{p,b}}$	dimensionless bulk temperature of particular solution
$\tilde{T}_{\mathrm{b}}$	dimensionless bulk temperature
T_{r}	ridge temperature
w	streamwise velocity, m/s
$\overline{w}$	mean streamwise velocity, m/s
$\tilde{w}$	dimensionless streamwise velocity; $\left(\mu w\right)\left(-\mathrm{d}p/\mathrm{d}z\right)^{-1}/D_{\mathrm{h}}^{2}$
$\overline{\tilde{w}}$	dimensionless mean streamwise velocity; $\left(\mu\overline{w}\right)\left(-\mathrm{d}p/\mathrm{d}z\right)^{-1}/D_{\mathrm{h}}^{2}$
x	lateral coordinate, m
$\tilde{x}$	dimensionless lateral coordinate; x/D_{h}
y	vertical coordinate, m
$\tilde{y}$	dimensionless vertical coordinate; y/D_{h}
z	streamwise coordinate, m
$\tilde{z}$	dimensionless streamwise coordinate; $z/(\mathrm{Pe}D_{\mathrm{h}})$
$\tilde{z}_{\mathrm{Pe}\pm}$	estimate of the dimensionless streamwise location where Nu becomes fully developed and the effects of Br and $\tilde{q}$ are negligible compared to those of Pe; $\left(\ln\left|\lambda_{\pm2}\right|-\ln\left|\lambda_{\pm1}\right|\right)/(\lambda_{\pm2}-\lambda_{\pm1})$
$\tilde{z}_{\mathrm{Br}\pm}$	estimate of the dimensionless streamwise location where the effects of Br and Pe become of the same order; $\ln\left(\mathrm{Br}^{-1}\right)/\lambda_{\pm1}$
$\tilde{z}_{\tilde{\mathrm{q}}\pm}$	estimate of the dimensionless streamwise location where the effects of $\tilde{q}$ and Pe become of the same order; $\ln\left(\tilde{q}^{-1}\right)/\lambda_{\pm1}$

Greek Symbols

λ_i	i-th eigenvalue
μ	dynamic viscosity, $\mathrm{Pa} \cdot \mathrm{s}$
ϕ	solid fraction; $(d-a)/d$
ψ_i	i-th eigenfunction
ρ	density, $\mathrm{kg/m^3}$

Subscripts

fd	fully developed conditions
i	indicator
$-$	refering to streamwise location $z \leq 0$
$+$	refering to streamwise location $z > 0$
s	smooth plates

Part IV

Conjugate Nusselt Numbers for Simultaneously-Developing Flow through Rectangular Ducts

Chapter 14

Introduction

Flow through rectangular ducts is common in heat transfer applications; consequently its thermal characteristics have been quantified in terms of various Nusselt numbers (Nu) for a wide range of flow conditions and aspect ratios [42, 27]. The common boundary conditions applied are those of uniform wall temperature $\textcircled{T}$ and of uniform heat rate per unit length of the duct with either circumferentially uniform wall temperature $\textcircled{H1}$ or uniform heat flux $\textcircled{H2}$ in each cross section [27]. Here we focus on the case of laminar forced convection with constant thermophysical properties and negligible viscous dissipation. An overview of the relevant previous work follows.

Clark and Kays [43] studied the case of hydrodynamically and thermally fully-developed flow through rectangular ducts of arbitrary aspect ratio when a $\textcircled{T}$ or $\textcircled{H1}$ boundary condition applies on all four walls of the duct. Savino and Siegel [44] also considered fully-developed flow with $\textcircled{H1}$ boundary condition but the heat flux applied on the shorter walls was set to be an arbitrary fraction of that applied along the longer walls. Schmidt and Newell [45] considered fully-developed conditions too but allowed one or more walls to be subjected to a $\textcircled{T}$ or $\textcircled{H1}$ boundary condition while the rest of them were insulated. Shah [46] studied the case of an $\textcircled{H2}$ boundary condition for fully-developed flow. Montgomery and Wibulswas [47] and Montgomery and Wibulswas [48] considered hydrodynamically-developed and thermally-developing flow, and simultaneously-developing flow, respectively, when a $\textcircled{T}$ or $\textcircled{H1}$ boundary condition applies on all four walls.

Conjugate effects under hydrodynamically and thermally fully-developed conditions were first studied by Han [49]. Heat was exchanged through two opposite sides of the duct subjected to an $\textcircled{H1}$ boundary condition, both where they were wetted by the fluid and

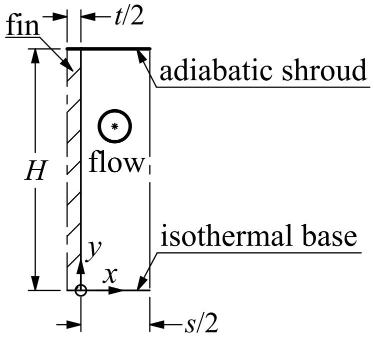

Figure 14.1: Rectangular duct under consideration.

formed the roots of extended surfaces [49]. Sparrow et al. [1] also considered this case but one side of the duct, i.e., the base of it, was subjected to an either Ⓣ or (H1) boundary condition and the opposite one was covered by an adiabatic shroud. Karamanis and Hodes [50] extended the available results of Sparrow et al. [1] for the Ⓣ boundary condition and provided a framework to use them to minimize the thermal resistance of longitudinal-fin heat sinks. Siegel and Savino [51] considered the same duct configuration and fully-developed conditions but heat was internally generated in part of the extended surfaces. Lyczkowski et al. [52] considered the case of hydrodynamically-developed and thermally-developing flow for this duct configuration for a variety of thermal boundary conditions. Moharana et al. [53] also studied this duct configuration but for simultaneously-developing flow when a (H2) boundary condition applies on the base of the duct. Finally, Moharana et al. [53] considered conduction effects within the heat-exchanging base too.

The present work complements the existing literature for the aforementioned duct configuration studying the case of conjugate heat transfer under conditions of simultaneously-developing flow when a Ⓣ boundary condition applies along the base of duct and the opposite side is covered by an adiabatic shroud as per Fig. 14.1. The external faces of the side walls are adiabatic; in the context of longitudinal-fin heat sinks that can be because of symmetry considerations as a series of these ducts are stacked in parallel. The height and length (perpendicular to the page) of the duct, the width of the wetted portion of the isothermal base, and the thickness of the extended surfaces are H, L, s, and, t, respectively. The flow is assumed to be steady and laminar, and the fluid and solid have constant thermophysical properties. There is no viscous dissipation and heat is transferred solely by forced convection.

The analysis is comprised of five parts. In Section 15, we identify the relevant dimensionless parameters and present the corresponding dimensionless formulation. Next, Section 16 provides the relevant definitions of the local conjugate Nusselt number along the extended surface, the local transversely-averaged one over the isothermal base, the average of that in the streamwise direction, and, finally, the average over the whole area of the isothermal base conjugate Nusselt number. Section 17 discusses the solution process of the dimensionless conjugate heat transfer problem, and results are presented in Section 18. Additional results for the average over the whole area of the isothermal base conjugate Nusselt number are provided in the Appendix. The results are relevant to, e.g., longitudinal-fin heat sinks [54, 55], catalytic reactors for micro fuel processors and biological sensors [56, 57].

Chapter 15

Analysis

15.1 Governing Equations and Dimensional Analysis

Given conditions of steady and hydrodynamically-developing laminar flow, a fluid with constant thermophysical properties and forced convection, the relevant forms of the continuity and the Navier-Stokes equations are, respectively,

$$\nabla \cdot \mathbf{U} = 0 \tag{15.1}$$

$$\rho\left(\mathbf{U} \cdot \nabla\right)\mathbf{U} = -\nabla p + \mu \nabla^2 \mathbf{U} \tag{15.2}$$

where p, ρ, and μ are the pressure, density, and dynamic viscosity, respectively, and

$$\mathbf{U} = \begin{bmatrix} u \\ v \\ w \end{bmatrix} \tag{15.3}$$

is the velocity vector where u, v, and w are the velocity components in the x, y, and z-direction, respectively. Utilizing the symmetry of the problem with respect to the plane through $x = s/2$, as per Fig. 14.1, the boundary conditions for the hydrodynamic problem are, as per the computational domain depicted in Fig. 15.1,

$$u = v = 0, w = w_{\text{in}} \text{ for } z = 0 \tag{15.4}$$

$$u = v = w = 0 \quad \text{for } x = 0,\ y = 0 \text{ and } y = H \tag{15.5}$$

$$u = \frac{\partial v}{\partial x} = \frac{\partial w}{\partial x} = 0 \quad \text{for } x = \frac{s}{2} \tag{15.6}$$

$$p = 0 \quad \text{for } z = L \tag{15.7}$$

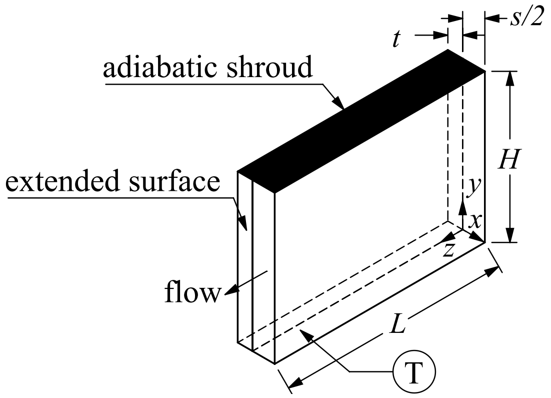

Figure 15.1: Computational domain.

where w_{in} is the uniform inlet streamwise velocity.

The relevant forms of the thermal energy equation for the fluid and the extended surface are, respectively,

$$\rho c_p \mathbf{U} \cdot \nabla T = k \nabla^2 T \tag{15.8}$$

$$\nabla^2 T_{\mathrm{e}} = 0 \tag{15.9}$$

where T and T_{e} are the fluid and extended surface temperatures, respectively, and k and c_p are the thermal conductivity and specific heat at constant pressure of the fluid, respectively. The boundary conditions for the thermal energy equation for the fluid are

$$T = T_{\mathrm{B}} \text{ for } y = 0 \tag{15.10}$$

$$\frac{\partial T}{\partial y} = 0 \text{ for } y = H \tag{15.11}$$

$$T = T_{\mathrm{i}} \text{ for } z = 0 \tag{15.12}$$

$$\frac{\partial T}{\partial z} = 0 \text{ for } z = L \tag{15.13}$$

$$\frac{\partial T}{\partial x} = 0 \text{ for } x = \frac{s}{2} \tag{15.14}$$

$$T = T_{\mathrm{e}} \text{ for } x = 0 \tag{15.15}$$

$$k\frac{\partial T}{\partial x} = k_{\mathrm{e}}\frac{\partial T_{\mathrm{e}}}{\partial x} \text{ for } x = 0 \tag{15.16}$$

where T_{B} and T_{i} are the temperature of the isothermal base and the uniform temperature of the fluid at the inlet of the duct, respectively, and k_{e} is the thermal conductivity of the extended surface. Equations (15.15) and (15.16) are the two conjugate boundary conditions that impose continuity of temperature and heat flux at the fluid-extended surface interface. The other boundary conditions for the extended surface are

$$
\begin{aligned}
T_{\mathrm{e}} &= T_{\mathrm{B}} \text{ for } y = 0 && (15.17)\\
\frac{\partial T_{\mathrm{e}}}{\partial y} &= 0 \text{ for } y = H && (15.18)\\
\frac{\partial T_{\mathrm{e}}}{\partial z} &= 0 \text{ for } z = 0 \text{ and } z = L && (15.19)\\
\frac{\partial T_{\mathrm{e}}}{\partial x} &= 0 \text{ for } x = -t && (15.20)
\end{aligned}
$$

along with the two conjugate boundary conditions at the fluid-extended surface interface given by Eqs. (15.15) and (15.16).

Equations (15.1)-(15.20) show that the conjugate heat transfer problem involves four geometric parameters (H, s, L, t), four thermophysical properties of the fluid (ρ, μ, c_p, k), one thermophysical property of the extended surface (k_{e}), and one external parameter (w_{in}). Therefore, the Buckingham Pi Theorem dictates that the conjugate Nusselt number for the case at hand is a function of six independent dimensionless parameters and a valid set of them is

$$
\begin{aligned}
\tilde{s} &= \frac{s}{D_{\mathrm{h}}} && (15.21)\\
\tilde{L} &= \frac{L}{D_{\mathrm{h}}} && (15.22)\\
\tilde{t} &= \frac{t}{D_{\mathrm{h}}} && (15.23)\\
\mathrm{Re}_{D_{\mathrm{h}}} &= \frac{\rho w_{\mathrm{in}} D_{\mathrm{h}}}{\mu} && (15.24)\\
\mathrm{Pr} &= \frac{c_p \mu}{k} && (15.25)\\
K_{\mathrm{e}} &= \frac{k}{k_{\mathrm{e}}} && (15.26)
\end{aligned}
$$

where $\tilde{s}$, $\tilde{L}$, and $\tilde{t}$ are the dimensionless width of the wetted portion of the base, the dimensionless length of the duct, and the dimensionless thickness of the extended surface, respectively. $\mathrm{Re}_{D_{\mathrm{h}}}$ is the Reynolds number based on the hydraulic diameter

$$D_{\mathrm{h}} = \frac{2sH}{s+H} \qquad (15.27)$$

Pr and K_{e} are the Prandtl number of the fluid and the fluid-to-extended surface thermal conductivity ratio, respectively. Finally, it is emphasized that the present analysis is valid for arbitrary values of the Péclet number ($\mathrm{Pe} = \mathrm{Re}_{D_\mathrm{h}}\mathrm{Pr}$) because it takes into consideration the axial conduction term in both the thermal energy equation for the fluid and the diffusion equation for the extended surface.

15.2 Dimensionless Hydrodynamic and Thermal Problems

Denoting nondimensional variables with tildes and defining

$$\begin{aligned} \tilde{x} &= \frac{x}{D_\mathrm{h}} && (15.28)\\ \tilde{y} &= \frac{y}{D_\mathrm{h}} && (15.29)\\ \tilde{z} &= \frac{z}{D_\mathrm{h}} && (15.30)\\ \tilde{\mathbf{U}} &= \frac{\mathbf{U}}{w_\mathrm{in}} && (15.31)\\ \tilde{p} &= \frac{D_\mathrm{h}}{\mu w_\mathrm{in}} p && (15.32) \end{aligned}$$

Equations (15.1) and (15.2) become, respectively,

$$\begin{aligned} \nabla \cdot \tilde{\mathbf{U}} &= 0 && (15.33)\\ \mathrm{Re}_{D_\mathrm{h}} \left(\tilde{\mathbf{U}} \cdot \nabla\right) \tilde{\mathbf{U}} &= -\nabla \tilde{p} + \nabla^2 \tilde{\mathbf{U}} && (15.34) \end{aligned}$$

subject to

$$\begin{aligned} \tilde{u} = \tilde{v} = 0, \tilde{w} &= 1 \text{ for } \tilde{z} = 0 && (15.35)\\ \tilde{u} = \tilde{v} = \tilde{w} &= 0 \text{ for } \tilde{x} = 0,\ \tilde{y} = 0 \text{ and } \tilde{y} = \tilde{H} && (15.36)\\ \tilde{u} = \frac{\partial \tilde{v}}{\partial \tilde{x}} = \frac{\partial \tilde{w}}{\partial \tilde{x}} &= 0 \text{ for } \tilde{x} = \frac{\tilde{s}}{2} && (15.37)\\ \tilde{p} &= 0 \text{ for } \tilde{z} = \tilde{L} && (15.38) \end{aligned}$$

where $\tilde{H} = H/D_\mathrm{h}$. Defining the dimensionless temperature for the fluid and the extended surface as

$$\begin{aligned} \tilde{T} &= \frac{T - T_\mathrm{i}}{T_\mathrm{B} - T_\mathrm{i}} && (15.39)\\ \tilde{T}_\mathrm{e} &= \frac{T_\mathrm{e} - T_\mathrm{i}}{T_\mathrm{B} - T_\mathrm{i}} && (15.40) \end{aligned}$$

respectively, the dimensionless thermal energy equation for the fluid becomes

$$\tilde{\mathbf{U}} \cdot \nabla \tilde{T} = \frac{1}{\mathrm{Pe}} \nabla^2 \tilde{T} \tag{15.41}$$

subject to

$$\begin{aligned}
\tilde{T} &= 1 \text{ for } \tilde{y} = 0 && (15.42)\\
\frac{\partial \tilde{T}}{\partial \tilde{y}} &= 0 \text{ for } \tilde{y} = \tilde{H} && (15.43)\\
\tilde{T} &= 0 \text{ for } \tilde{z} = 0 && (15.44)\\
\frac{\partial \tilde{T}}{\partial \tilde{z}} &= 0 \text{ for } \tilde{z} = \tilde{L} && (15.45)\\
\frac{\partial \tilde{T}}{\partial \tilde{x}} &= 0 \text{ for } \tilde{x} = \frac{\tilde{s}}{2} && (15.46)\\
\tilde{T} &= \tilde{T}_{\mathrm{e}} \text{ for } \tilde{x} = 0 && (15.47)\\
K_{\mathrm{e}} \frac{\partial \tilde{T}}{\partial \tilde{x}} &= \frac{\partial \tilde{T}_{\mathrm{e}}}{\partial \tilde{x}} \text{ for } \tilde{x} = 0 && (15.48)
\end{aligned}$$

The dimensionless thermal energy equation for the extended surface becomes

$$\nabla^2 \tilde{T}_{\mathrm{e}} = 0 \tag{15.49}$$

and the corresponding boundary conditions are

$$\begin{aligned}
\tilde{T}_{\mathrm{e}} &= 1 \text{ for } \tilde{y} = 0 && (15.50)\\
\frac{\partial \tilde{T}_{\mathrm{e}}}{\partial \tilde{y}} &= 0 \text{ for } \tilde{y} = \tilde{H} && (15.51)\\
\frac{\partial \tilde{T}_{\mathrm{e}}}{\partial \tilde{z}} &= 0 \text{ for } \tilde{z} = 0 \text{ and } \tilde{z} = \tilde{L} && (15.52)\\
\frac{\partial \tilde{T}_{\mathrm{e}}}{\partial \tilde{x}} &= 0 \text{ for } \tilde{x} = -\tilde{t} && (15.53)
\end{aligned}$$

along with the two conjugate boundary conditions at the fluid-extended surface interface given by Eqs. (15.47) and (15.48).

The solution process of the conjugate problem described by Eqs. (15.33)-(15.38) and Eqs. (15.41)-(15.53) is comprised of two parts. First, Eqs. (15.33) and (15.34) are solved subject to the boundary conditions given by Eqs. (15.35)-(15.38) to compute the dimensionless velocity field. Then, Eqs. (15.41) and (15.49) are solved simultaneously subject to the boundary conditions given by Eqs. (15.42)-(15.48) and (15.50)-(15.53) utilizing the previously computed $\tilde{\mathbf{U}}$ to determine the dimensionless temperature fields of the fluid and the extended surface. Once, $\tilde{T}$ is known the various conjugate Nusselt numbers follow from an energy balance as per Section 16.1.

In the present analysis, the conjugate problem was solved numerically using the general CFD solver FLUENT® in conjunction with ANSYS Workbench® for multiple sets of values of the of dimensionless parameters. Details of the numerical method and the results are presented in Sections 17 and 18, respectively.

Chapter 16

Conjugate Nusselt Number

16.1 Local conjugate Nusselt Number along the extended surface

The local thermal performance of the extended surface can be quantified by the corresponding local conjugate Nusselt number defined as

$$\mathrm{Nu_e}\left(\tilde{\mathrm{y}}, \tilde{\mathrm{z}}\right) = \frac{h_{\mathrm{e}} D_{\mathrm{h}}}{k} \tag{16.1}$$

where h_{e} is the local heat transfer coefficient along the extended surface. An energy balance at a point along the extended surface yields

$$-k \left.\frac{\partial T}{\partial x}\right|_{x=0} = h_{\mathrm{e}} \left(T|_{x=0} - T_{\mathrm{b}} \right) \tag{16.2}$$

where T_{b} is the bulk temperature of the fluid at the corresponding streamwise location defined as

$$T_{\mathrm{b}}\left(z\right) = \frac{2}{sHw_{\mathrm{in}}} \int_0^H \int_0^{s/2} wT \mathrm{d}x \mathrm{d}y \tag{16.3}$$

Substituting Eqs. (16.2) and (16.3) into Eq. (16.1) yields

$$\mathrm{Nu_e}\left(\tilde{\mathrm{y}}, \tilde{\mathrm{z}}\right) = -\frac{1}{\left(\left.\tilde{T}\right|_{\tilde{x}=0} - \tilde{T}_{\mathrm{b}} \right)} \left.\frac{\partial \tilde{T}}{\partial \tilde{x}}\right|_{\tilde{x}=0} \tag{16.4}$$

where

$$\tilde{T}_{\mathrm{b}}\left(\tilde{z}\right) = \frac{2}{\tilde{s}\tilde{H}} \int_0^{\tilde{H}} \int_0^{\tilde{s}/2} \tilde{w}\tilde{T} \mathrm{d}\tilde{x} \mathrm{d}\tilde{y} \tag{16.5}$$

We emphasize that $\mathrm{Nu_e}$ is the only conjugate Nusselt number defined in this analysis based on the temperature difference $(T|_{x=0} - T_\mathrm{b})$ because this is the relevant driving force for heat transfer to investigate the relative thermal performance between different locations along the height and length of the extended surface. To quantify the actual local thermal performance of the extended surface, we define the dimensionless local heat flux as

$$\tilde{q}''_\mathrm{e} = -\left.\frac{\partial \tilde{T}}{\partial \tilde{x}}\right|_{\tilde{x}=0} \tag{16.6}$$

which is essentially a local Nusselt number based on the constant temperature difference $(T_\mathrm{B} - T_\mathrm{i})$, but we choose not to call it as such to avoid confusion with $\mathrm{Nu_e}$. The different nature of $\mathrm{Nu_e}$ and $\tilde{q}''_\mathrm{e}$ can be illustrated by the fact as $\tilde{z} \to \infty$ and thus the flow becomes fully-developed, $\mathrm{Nu_e}$ asymptotically converges to a distribution along the height of the extended surface that is independent of $\tilde{z}$ [1] and which quantifies the relative performance to heat transfer along the height of the extended surface. To the contrary, $\tilde{q}''_\mathrm{e} \to 0$, as $\tilde{z} \to \infty$ given that at this limit the flow becomes essentially isothermal and minimal heat transfer occurs. The remaining definitions for the Nusselt number are based on the constant temperature difference $(T_\mathrm{B} - T_\mathrm{i})$ which is the relevant driving force for heat transfer to investigate the thermal performance of the rectangular duct as a whole.

16.2 Local transversely-averaged conjugate Nusselt Number of the isothermal base

The local, in terms of the streamwise direction, thermal performance of the rectangular duct can be quantified using the local transversely-averaged conjugate Nusselt Number of the isothermal base defined as

$$\mathrm{Nu_B}(\tilde{z}) = \frac{h_\mathrm{B} D_\mathrm{h}}{k} \tag{16.7}$$

where h_B is the transversely-averaged heat transfer coefficient of the isothermal base. An energy balance at a streamwise location along the isothermal base yields

$$\int_{-t}^{0} -k_\mathrm{e} \left.\frac{\partial T_\mathrm{e}}{\partial y}\right|_{y=0} \mathrm{d}x + \int_{0}^{s/2} -k \left.\frac{\partial T}{\partial y}\right|_{y=0} \mathrm{d}x = \left(t + \frac{s}{2}\right) h_\mathrm{B} \left(T_{\mathrm{B}.} - T_\mathrm{i}\right) \tag{16.8}$$

Substituting Eq. (16.8) into Eq. (16.7) yields

$$\mathrm{Nu_B}\left(\tilde{z}\right) \quad = \quad -\frac{\frac{1}{K_\mathrm{e}}\int_{-\tilde{t}}^{0}\left.\frac{\partial \tilde{T}_\mathrm{e}}{\partial \tilde{y}}\right|_{\tilde{y}=0}\mathrm{d}\tilde{x}+\int_{0}^{\tilde{s}/2}\left.\frac{\partial \tilde{T}}{\partial \tilde{y}}\right|_{\tilde{y}=0}\mathrm{d}\tilde{x}}{\left(\tilde{t}+\tilde{s}/2\right)} \tag{16.9}$$

16.3 Average conjugate Nusselt Number of the isothermal surface

The average conjugate Nusselt Number of the isothermal base between the duct inlet and a dimensionless distance $\tilde{z}$ from it, is

$$\overline{\mathrm{Nu}}_\mathrm{B}\left(\tilde{z}\right) = \frac{1}{z}\int_0^z \mathrm{Nu_B}\mathrm{d}z \tag{16.10}$$

Thus, from Eqs. (16.9) and (16.10), it follows that

$$\overline{\mathrm{Nu}}_\mathrm{B}\left(\tilde{z}\right) \quad = \quad -\frac{\int_0^{\tilde{z}}\left(\frac{1}{K_\mathrm{e}}\int_{-\tilde{t}}^{0}\left.\frac{\partial \tilde{T}_\mathrm{e}}{\partial \tilde{y}}\right|_{\tilde{y}=0}\mathrm{d}\tilde{x}+\int_{0}^{\tilde{s}/2}\left.\frac{\partial \tilde{T}}{\partial \tilde{y}}\right|_{\tilde{y}=0}\mathrm{d}\tilde{x}\right)\mathrm{d}\tilde{z}}{\tilde{z}\left(\tilde{t}+\tilde{s}/2\right)} \tag{16.11}$$

Finally, we denote $\overline{\mathrm{Nu}}_\mathrm{B}\left(\tilde{L}\right)$ by $\overline{\mathrm{Nu}}_{\mathrm{B},\tilde{L}}$; this is the average conjugate Nusselt Number over the total area of the isothermal base of the duct.

Chapter 17

Solution of the conjugate heat transfer problem

The conjugate heat transfer problem defined by Eqs. (15.33)-(15.38) and (15.41)-(15.53) was solved in the present study for multiple sets of values of the dimensionless independent variables using the Finite Volume Method implemented in FLUENT®, in conjunction with ANSYS Workbench®. The large number of cases considered were coded into parametric models. Each parametric model had fixed values of $\tilde{s}$, $\tilde{L}$, $\tilde{t}$, Pr, and K_e, and the value of $\mathrm{Re}_{D_\mathrm{h}}$ was varied. Results have been computed for $\tilde{s} = [0.5125, 0.6]$, $\tilde{L} = [5.5, 52.5]$, $\tilde{t} = [0.01375, 0.2625]$, $\mathrm{Pr} = 0.71$, $K_\mathrm{es} = 6.56e-5$ and $11.1e-5$, and $\mathrm{Re}_{D_\mathrm{h}} = [51.68, 7627.46]$. Note that for the operating points with $\mathrm{Re}_{D_\mathrm{h}} > 2300$, the local Reynolds number at the outlet of the duct $\mathrm{Re}_L = (\rho w_\mathrm{in} L)/\mu$ was below $5e5$. As such, given that the flow at the duct inlet is laminar, it remains so throughout the computational domain [42]. The selected ranges of values of the dimensionless parameters are relevant to thermal management of electronics applications and correspond to ducts with $H = [2\,\mathrm{cm}, 4\,\mathrm{cm}]$, $s = [1\,\mathrm{mm}, 4\,\mathrm{mm}]$, $L = [4\,\mathrm{cm}, 10\,\mathrm{cm}]$, $t = [0.1\,\mathrm{mm}, 0.5\,\mathrm{mm}]$, with copper or aluminum extended surfaces, air for the fluid, and a pressure drop across the duct between 10 Pa and 60 Pa.

The execution process of the parametric models was as follows. For of each model, ANSYS Workbench® defines the geometry of the domain using the prescribed $\tilde{s}$, $\tilde{L}$ and $\tilde{t}$. Then, it discretizes the resulting domain with a structured mesh; the number of discretization cells for each model was between 184800 to 735000 elements to ensure grid independence. Next, ANSYS Workbench® creates the corresponding FLUENT® model using the resulting mesh and the prescribed $\mathrm{Re}_{D_\mathrm{h}}$, Pr and K_e. FLUENT® iteratively solves the conjugate problem employing the Coupled Pseudo Transient solver and Second-Order Upwind Scheme [58], until convergence. The convergence criterion was that the computed residual for $\overline{\mathrm{Nu}}_{\mathrm{B},\tilde{L}}$ to be less than $1\mathrm{E}-6$. Then, the above process is repeated for the next higher value of $\mathrm{Re}_{D_\mathrm{h}}$of the parametric model.

Chapter 18

Results

Figure 18.1 presents the computed dimensionless temperature of the extended surface $\left(\tilde{T}_{\mathrm{e}}\right)$ versus $\tilde{y}$ for $\tilde{s} = 0.525$, $\tilde{L} = 26.25$, $\mathrm{Re}_{D_{\mathrm{h}}} = 882.92$, $K_{\mathrm{e}} = 11.1e-5$ and $\mathrm{Pr} = 0.71$, at different streamwise locations and selected values of $\tilde{t}$. As expected, for every given location $\tilde{y}$, $\tilde{T}_{\mathrm{e}}$ increases monotonically as $\tilde{z}$ increases. Moreover, the rate at which the extended surface tends to become isothermal increases as $\tilde{t}$ increases from 0.026 to 0.053, because as $\tilde{t}$ increases the conduction resistance of the extended surface decreases.

Figure 18.2 presents the computed dimensionless local heat flux $(\tilde{q}''_{\mathrm{e}})$ versus $\tilde{y}$ for the aforementioned values of the dimensionless independent variables. It shows that for every given location $\tilde{y}$, $\tilde{q}''_{\mathrm{e}}$ decreases monotonically as $\tilde{z}$ increases as expected since the temperature of the fluid increases. The two local maxima of each curve indicate the locations of the corresponding developing thermal boundary layers. They show that the no-slip boundary

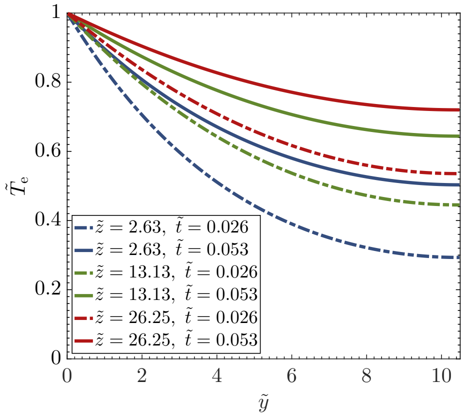

Figure 18.1: $\tilde{T}_{\mathrm{e}}$ versus $\tilde{y}$ for $\tilde{s} = 0.525$, $\tilde{L} = 26.25$, $\mathrm{Re}_{D_{\mathrm{h}}} = 882.92$, $K_{\mathrm{e}} = 11.1e-5$ and $\mathrm{Pr} = 0.71$, at different streamwise locations and selected values of $\tilde{t}$.

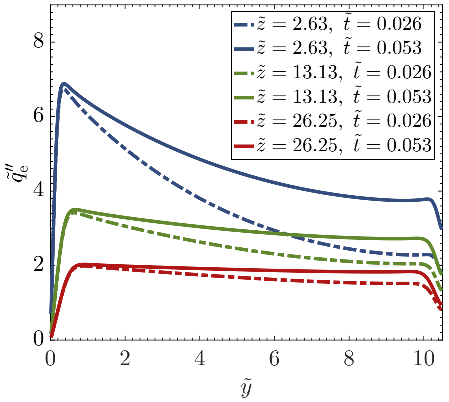

Figure 18.2: $\tilde{q}''_{\mathrm{e}}$ versus $\tilde{y}$ for $\tilde{s} = 0.525$, $\tilde{L} = 26.25$, $\mathrm{Re}_{D_\mathrm{h}} = 882.92$, $K_\mathrm{e} = 11.1e-5$ and $\mathrm{Pr} = 0.71$, at different streamwise locations and selected values of $\tilde{t}$.

condition that applies along the wetted part of the base and the adiabatic shroud degrades significantly the local heat transfer from the extended surface due to the slow moving fluid in these areas. This is more pronounced as $\tilde{y} \to 0$ where the fluid temperature is close to that of the isothermal base and as such $\tilde{q}''_{\mathrm{e}} \to 0$. Also, note that close to the isothermal base, $\tilde{q}''_{\mathrm{e}}$ is approximately the same at each streamwise location for both values of $\tilde{t}$. This is because heat transfer from the lower portion of the extended surface is predominantly governed by the aspect aspect ratio of the duct and its effects on the velocity field. However, heat transfer from the upper portion of the extended surface is predominantly governed by the conduction resistance of the extended surface, and as such lower values of $\tilde{t}$ provide smaller $\tilde{q}''_{\mathrm{e}}$ at that area for the same $\tilde{z}$. Similar behavior was observed by Sparrow et al. [1] for the case of fully-developed flow.

Figure 18.3 presents the local conjugate Nusselt number along the extended surface (Nu_e) versus $\tilde{y}$ for the same values of the independent variables as those for Figs. 18.1 and 18.2. Recall that Nu_e represents the relative local efficiency to heat transfer along the extended surface. Figure 18.3 indicates that the local efficiency to heat transfer from the lower part of the extended surface decreases monotonically as $\tilde{z}$ increases. This is because this part of the extended surface operates at temperatures close to that of the isothermal base. As such, as the temperature of the fluid increases as $\tilde{z}$ increases, the local heat transfer from the lower part of the extended surface degrades for given $\tilde{y}$ as $\tilde{z}$ increases. However, the opposite is true for the the local efficiency to heat transfer from the upper part of the extended surface. There, Nu_e increases as $\tilde{z}$ increases for given $\tilde{y}$, albeit not monotonically for every $\tilde{t}$. This is because in this part of the extended surface $\tilde{T}_\mathrm{e}$ increases as $\tilde{z}$ increases

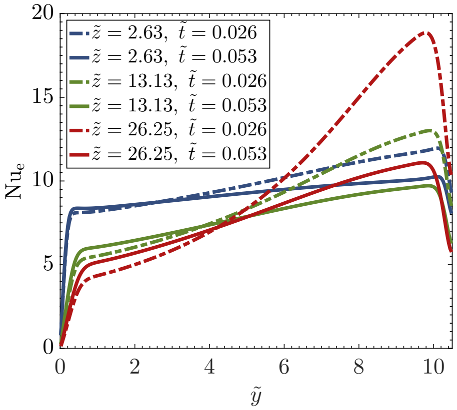

Figure 18.3: $\mathrm{Nu_e}$ versus $\tilde{y}$ for $\tilde{s} = 0.525$, $\tilde{L} = 26.25$, $\mathrm{Re}_{D_\mathrm{h}} = 882.92$, $K_\mathrm{e} = 11.1e-5$ and $\mathrm{Pr} = 0.71$, at different streamwise locations and selected values of $\tilde{t}$.

for given $\tilde{y}$.

Overall, Figs. 18.1, 18.2 and 18.3 show the strong coupling between the heat conduction within the extended surface and the convective heat transfer occurring in the flow, and their effects on the overall heat transfer characteristics of the duct. If, e.g., we draw our attention on the solid green curve corresponding to $\tilde{z} = 13.13$ and $\tilde{t} = 0.053$ in these three figures, despite the fact that the extended surface is far from being isothermal due to its finite thermal conductivity, as per Fig. 18.1, the local dimensionless heat transfer along the extended surface away from the isothermal base and the adiabatic shroud is approximately uniform, as per Fig. 18.2, because the local efficiency to heat transfer increases as $\tilde{y}$ increases, as per Fig. 18.3. However, for streamwise locations closer to the inlet of the duct where the effects of the finite thermal conductivity of the extended surface are dominant, per the blue solid curve corresponding to $\tilde{z} = 2.63$ and $\tilde{t} = 0.053$ in the aforementioned figures, the modest increase of the local efficiency to heat transfer along the extended surface as $\tilde{y}$ increases, as per Fig. 18.3, cannot compensate for the sharp decrease of $\tilde{T}_\mathrm{e}$ along the height of the extended surface, as per Fig. 18.1, resulting to a highly non-uniform decreasing distribution for the dimensionless local heat flux along the height of the extended surface, as per Fig. 18.2.

Figure 18.4 presents the local transversely-averaged ($\mathrm{Nu_B}$) and the average $\left(\overline{\mathrm{Nu}}_\mathrm{B}\right)$ conjugate Nusselt number of the isothermal base versus $\tilde{z}$ for the aforementioned values of the dimensionless independent variables. Both, $\mathrm{Nu_B}$ and $\overline{\mathrm{Nu}}_\mathrm{B}$ exhibit the anticipated trends for an internal forced convection flow with $\mathrm{Nu_B} < \overline{\mathrm{Nu}}_\mathrm{B}$ at each streamwise location, and $\overline{\mathrm{Nu}}_\mathrm{B} \rightarrow \overline{\mathrm{Nu}}_{\mathrm{B},\tilde{L}}$ as $\tilde{z} \rightarrow \tilde{L}$.

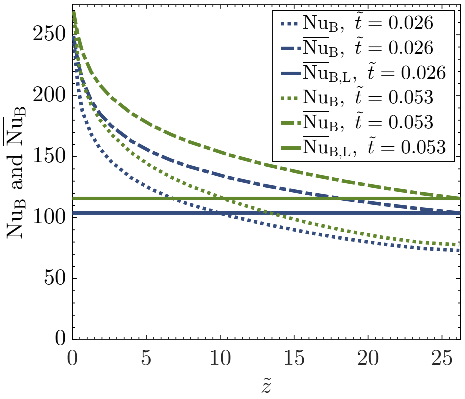

Figure 18.4: $\mathrm{Nu_B}$ and $\overline{\mathrm{Nu}}_\mathrm{B}$ versus $\tilde{z}$ for $\tilde{s} = 0.525$, $\tilde{L} = 26.25$, $\mathrm{Re}_{D_\mathrm{h}} = 882.92$, $K_\mathrm{e} = 11.1e-5$ and $\mathrm{Pr} = 0.71$ for selected values of $\tilde{t}$.

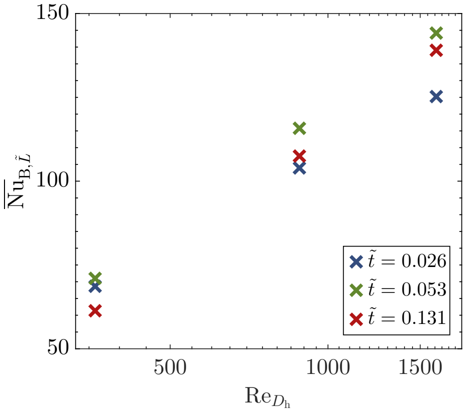

Figure 18.5: $\overline{\mathrm{Nu}}_{\mathrm{B},\tilde{L}}$ versus $\mathrm{Re}_{D_\mathrm{h}}$ for $\tilde{s} = 0.525$, $\tilde{L} = 26.25$, $K_\mathrm{e} = 11.1e-5$ and $\mathrm{Pr} = 0.71$ for selected values of $\tilde{t}$.

Figure 18.5 presents the average over the total area of the isothermal base conjugate Nusselt Number $\left(\overline{\mathrm{Nu}}_{\mathrm{B},\tilde{L}}\right)$ versus $\mathrm{Re}_{D_\mathrm{h}}$ for $\tilde{s} = 0.525$, $\tilde{L} = 26.25$, $K_\mathrm{e} = 11.1e-5$, and $\mathrm{Pr} = 0.71$, for selected values of $\tilde{t}$. The results indicate that there exists an optimal $\tilde{t}$ in each case that maximizes $\overline{\mathrm{Nu}}_{\mathrm{B},\tilde{L}}$ for the prescribed $\tilde{s}$, $\tilde{L}$, K_e, Pr, and $\mathrm{Re}_{D_\mathrm{h}}$. Similarly, if only K_e, Pr and $\mathrm{Re}_{D_\mathrm{h}}$ are prescribed, an optimization can be performed using the provided tabulation of the $\overline{\mathrm{Nu}}_{\mathrm{B},\tilde{L}}$ in the Appendix to determine the optimal $\tilde{s}$, $\tilde{L}$, and $\tilde{t}$ that maximize $\overline{\mathrm{Nu}}_{\mathrm{B},\tilde{L}}$ as per the approach proposed by Karamanis and Hodes [55]. Such optimizations are relevant to thermal management of electronics applications.

Chapter 19

Conclusions

The analysis considered the case of conjugate forced-convection heat transfer through a rectangular duct. Heat was exchanged through the isothermal base of the duct, i.e., the surface area comprised of the wetted portion of its base and the roots of its two side walls, which are extended surfaces within which conduction is three-dimensional. The opposite side of the duct was covered by an adiabatic shroud and the external faces of the side walls were adiabatic. The flow was steady, laminar and simultaneously-developing and the fluid had constant thermophysical properties. Prescribed were the width of the wetted portion of the base, the length of the duct, and the thickness of the extended surfaces, all three of them non-dimensionalized by the hydraulic diameter of the duct, and, additionally, the Reynolds number of the flow, the Prandtl number of the fluid, and the fluid-to-extended surface thermal conductivity ratio. The dimensionless temperature fields in the fluid and the extended surfaces were computed for multiple sets of values of the prescribed quantities. Corresponding results for the local conjugate Nusselt number along the extended surface ($\mathrm{Nu_e}$), the local transversely-averaged one over the isothermal base of the duct ($\mathrm{Nu_B}$), the average of that in the streamwise direction $\left(\overline{\mathrm{Nu}}_\mathrm{B}\right)$, and the average one over the whole area of the isothermal base of the duct $\left(\overline{\mathrm{Nu}}_{\mathrm{B},\tilde{L}}\right)$ were discussed. The local conjugate Nusselt number along the extended surface was shown to have strong dependence on the location along the extended surface. $\mathrm{Nu_e}$ monotonically decreases in the streamwise direction for locations close to the isothermal base given that at these locations the temperature of the extended surface is close to that of the isothermal base and that the temperature of the fluid increases in the streamwise direction. To the contrary, $\mathrm{Nu_e}$ increases in the streamwise direction for locations far from the isothermal base given that at these locations the temperature of the extended surface increases in the streamwise direction. The latter trend becomes more pronounced as the thickness of the extended surface decreases and thus the resistance to conduction of the extended surface increases. The results for the average over the whole area of the isothermal base of the duct conjugate Nusselt number show that for prescribed fluid-to-extended surface thermal conductivity ratio, and Reynolds and Prandtl numbers, there exist an optimal combination of the dimensionless width of the wetted portion of the base of the duct, duct length, and extended surface thickness, that maximize the heat transfer per unit area from the isothermal base. A dense tabulation of the average over the whole area of the isothermal base conjugate Nusselt number is provided in the Appendix to facilitate such optimizations.

Nomenclature

c_p	specific heat at constant pressure, $\mathrm{J/(kg\,K)}$
D_h	hydraulic diameter of the channel; $(2sH)/(s+H)$
H	rectangular duct height, m
h_B	local transversely-averaged heat transfer coefficient of the isothermal base, $\mathrm{W/(m^2\,K)}$
h_e	local heat transfer coefficient along the extended surface, $\mathrm{W/(m^2\,K)}$
$\tilde{H}$	rectangular duct dimensionless height; H/D_h
k	thermal conductivity of fluid, $\mathrm{W/(m\,K)}$
K_e	fluid-to-extended surface thermal conductivity ratio; k/k_e
k_e	thermal conductivity of extended surface, $\mathrm{W/(m\,K)}$
L	rectangular duct length, m
$\tilde{L}$	rectangular duct dimensionless length; L/D_h
$\mathrm{Nu_B}$	local transversely-averaged conjugate Nusselt Number of the isothermal base; $h_\mathrm{B}D_\mathrm{h}/k$
$\overline{\mathrm{Nu}}_\mathrm{B}$	average conjugate Nusselt Number of the isothermal base; $\int_0^z \mathrm{Nu_B}\,\mathrm{d}z/z$
$\overline{\mathrm{Nu}}_{\mathrm{B},\tilde{L}}$	average conjugate Nusselt Number over the total area of the isothermal base; $\overline{\mathrm{Nu}}_\mathrm{B}\left(\tilde{L}\right)$
$\mathrm{Nu_e}$	local conjugate Nusselt number along the extended surface; $h_\mathrm{e}D_\mathrm{h}/k$
p	pressure, Pa
$\tilde{p}$	dimensionless pressure; $(D_\mathrm{h}p)/(\mu w_\mathrm{in})$

Pe	Péclet number; $\mathrm{Re}_{D_\mathrm{h}}\mathrm{Pr}$
Pr	Prandtl number; $c_p\mu/k$
$\tilde{q}''_\mathrm{e}$	dimensionless local heat flux along the extended surface; $-\partial\tilde{T}/\partial\tilde{x}\rvert_{\tilde{x}=0}$
$\mathrm{Re}_{D_\mathrm{h}}$	Reynolds number based on D_h; $\left(\rho w_\mathrm{in} D_\mathrm{h}\right)/\mu$
Re_L	local Reynolds number at the outlet of the duct; $\left(\rho w_\mathrm{in} L\right)/\mu$
s	width of the wetted portion of the isothermal base, m
$\tilde{s}$	dimensionless width of the wetted portion of the isothermal base; s/D_h
T	fluid temperature, °C
t	extended surface thickness, m
$\tilde{t}$	extended surface dimensionless thickness; t/D_h
T_B	temperature of the isothermal base, °C
T_b	fluid bulk temperature; $2\int_0^H\int_0^{s/2} wT\mathrm{d}x\mathrm{d}y/(sHw_\mathrm{in})$
$\tilde{T}_\mathrm{b}$	dimensionless fluid bulk temperature; $2\int_0^{\tilde{H}}\int_0^{\tilde{s}/2}\tilde{w}\tilde{T}\mathrm{d}\tilde{x}\mathrm{d}\tilde{y}/\left(\tilde{s}\tilde{H}\right)$
T_i	fluid uniform inlet temperature, °C
T_e	extended surface temperature, °C
$\tilde{T}_\mathrm{e}$	dimensionless extended surface temperature; $\left(T_\mathrm{e}-T_\mathrm{i}\right)/\left(T_\mathrm{B}-T_\mathrm{i}\right)$
$\tilde{T}$	dimensionless fluid temperature; $\left(T-T_\mathrm{i}\right)/\left(T_\mathrm{B}-T_\mathrm{i}\right)$
$\mathbf{U}$	velocity vector, m/s
u	velocity component x-direction, m/s
$\tilde{\mathbf{U}}$	dimensionless velocity vector; $\mathbf{U}/w_\mathrm{in}$
v	velocity component y-direction, m/s
w	velocity component z-direction, m/s
w_in	uniform inlet streamwise velocity, m/s

$\tilde{w}$	dimensionless streamwise velocity; w/w_{in}
x	lateral coordinate, m
$\tilde{x}$	dimensionless lateral coordinate; x/D_{h}
y	vertical coordinate, m
$\tilde{y}$	dimensionless vertical coordinate; y/D_{h}
z	streamwise coordinate, m
$\tilde{z}$	dimensionless streamwise coordinate; z/D_{h}

Greek Symbols

μ	dynamic viscosity, Pa s
ρ	fluid density, $\mathrm{kg/m^3}$

Part V

Simultaneous Optimization of an Array of Heat Sinks

Chapter 21

Introduction

Effective thermal management of heat-dissipating microelectronic components requires addressing three primary resistances. They account for conduction in the semiconductor die and its package, thermal interfaces, and, our focus here, heat sinks. In general, a heat source is imposed along the bottom side of the base of a finned heat sink of equal or larger footprint. The thermal resistance between it and the coolant flowing through the heat sink follows from the solution of a conjugate heat transfer problem. A rigorous analysis to compute this parameter captures heat spreading in the base of the heat sink (if relevant), conduction along the fins and coolant-side convective heat transfer. It is rarely possible to perform this task analytically; consequently, Computational Fluid Dynamics (CFD), a laborious and slow process, is used. Hence, although it may be used to optimize the geometry of an isolated heat sink, a brute-force approach based upon it is impractical to optimize an array of them.

It is relevant to consider various approaches to heat sink optimization before describing our new one. We limit our discussion and the new results provided here to the case when the side of the base opposite the heat source, i.e., the plane of the base of the fins and the prime surface, is essentially isothermal. This is a valid assumption in many high-performance heat sinks as they often have heat pipes running along their length, or their base itself is one in the form of a vapor chamber. We further restrict our attention to forced convection in laminar flow through fully-shrouded longitudinally-finned heat sinks as per Fig. 21.1, which is a very common configuration in practice. A simple and often used approach is to assume hydrodynamically and thermally developed flow through an isothermal heat sink, and compute the thermal resistance based on a log-mean temperature

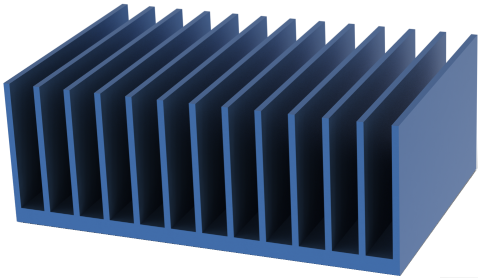

Figure 21.1: Longitudinal-fin heat sink (HS).

difference, where the mean heat transfer coefficient assumes a parallel plate configuration between fins. However, it is well known that 100% efficient fins do not minimize thermal resistance [59]. The accuracy of such a problem may be improved by using a semi-analytical approach to capture two-dimensional conduction along the fins, and, for the convective part, by assuming simultaneously developing flow between isothermal parallel plates, as per the method described by Holahan et al. [60].

Sparrow et al. [1] solved the full conjugate problem, i.e., conduction in the fin coupled to convection in the flow, for hydrodynamically and thermally developed flow. They neglected edge effects, a generally valid assumption due to the large number of fins on heat sinks. Hence, their domain consisted of half of a fin and half of an adjacent gap through which coolant flows, as per Fig. 21.2, where s, t and H are the fin spacing, thickness and height, respectively. The velocity and temperature profiles in the coolant, and the temperature profile in the fin were fully resolved. They concluded that the assumption of a uniform heat transfer coefficient is generally invalid. Indeed, they showed that for realistic fin thickness and thus efficiency, the heat transfer coefficient based on the bulk temperature of the coolant is often negative near the tip of the fin. Karamanis and Hodes [50] utilized the conjugate formulation developed by Sparrow et al. [1] to develop a procedure to optimize fin thickness, spacing, height and length for hydrodynamically and thermally developed flow. Also, Karamanis and Hodes [50] computed an extensive tabulation of the conjugate Nusselt number for heat sink-coolant combinations of copper-air, copper-water, aluminum-air and silicon-water. The dimensional flow and thermal resistances of a heat sink under these flow conditions follow directly from these tabulations.

Karamanis and Hodes [2] extended the conjugate formulation of Sparrow et al. [1] to simultaneously developing flow. The domain also consisted of half of a fin and half of an adjacent gap through which coolant flows, but, as per Fig. 21.3, it had a finite length L in

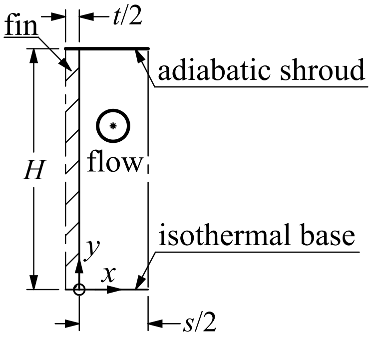

Figure 21.2: Computational domain of Sparrow et al. [1].

the streamwise direction because the transport problem is three-dimensional. Importantly, as in Sparrow et al. [1], the heat transfer coefficient used to define the conjugate Nusselt number is based on the total rate of heat flow along the prime surface and the fin, and on the temperature difference between the domain base and the coolant at the inlet. Karamanis and Hodes [2] show that per the Pi Theorem, the conjugate Nusselt number is a function of six independent dimensionless parameters, namely,

$$\tilde{s} = \frac{s}{D_\mathrm{h}} \tag{21.1}$$

$$\tilde{t} = \frac{t}{D_\mathrm{h}} \tag{21.2}$$

$$\tilde{L} = \frac{L}{D_\mathrm{h}} \tag{21.3}$$

$$\mathrm{Re}_{D_\mathrm{h}} = \frac{\rho \bar{w} D_\mathrm{h}}{\mu} \tag{21.4}$$

$$\mathrm{Pr} = \frac{c_p \mu}{k} \tag{21.5}$$

$$K_\mathrm{f} = \frac{k}{k_\mathrm{f}} \tag{21.6}$$

where $\tilde{s}$, $\tilde{t}$, and $\tilde{L}$ are the dimensionless fin spacing, dimensionless fin thickness and dimensionless heat sink length, respectively. $\mathrm{Re}_{D_\mathrm{h}}$ is the Reynolds number based on the hydraulic diameter

$$D_\mathrm{h} = \frac{2sH}{s+H} \tag{21.7}$$

Pr and K_f are the Prandtl number of the coolant and the coolant-to-fin thermal conductivity ratio. ρ, μ, c_p, and k are the density, dynamic viscosity, specific heat at constant pressure, and thermal conductivity of the coolant, respectively. k_f and $\bar{w}$ are the thermal conductivity of the fin and the mean velocity of the flow, respectively. Karamanis and Hodes [2] computed

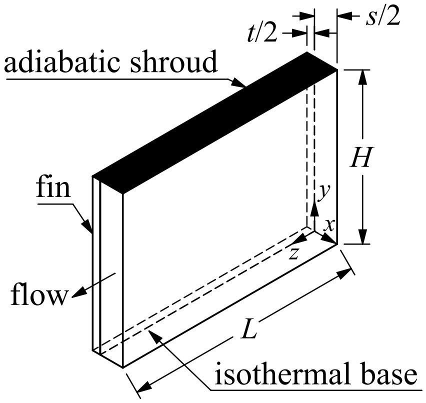

Figure 21.3: Computational domain of Karamanis and Hodes [2].

an extensive tabulation of the corresponding conjugate Nusselt numbers for heat sink-coolant combinations of copper-air and aluminum-air.

Here, we present a novel approach using such Poiseuille and conjugate Nusselt numbers [2] to simultaneously optimize the fin geometries of an array of longitudinal-fin heat sinks such as those found in, e.g., circuit packs, as per Fig. 21.4. Our method embeds the Poiseuille and conjugate Nusselt numbers in Flow Network Modeling (FNM) representations of such circuit packs in the form of look-up tables and, in turn, embeds the corresponding FNMs in a Multi-Variable Optimization framework (MVO) to optimize the fin geometries. We refer to this hybrid numerical scheme as CFM as per the first letter of the three existing schemes that it is based upon.

The remainder of this paper is divided into two sections. Section 22 provides background material on CFD, FNM, and MVO. Section 23 presents the hybridization approach and concludes with an example. Finally, we note that the present method is applicable to other types of heat sink geometries and for turbulent flow as well, provided that the corresponding Poiseuille and conjugate Nusselt numbers are available.

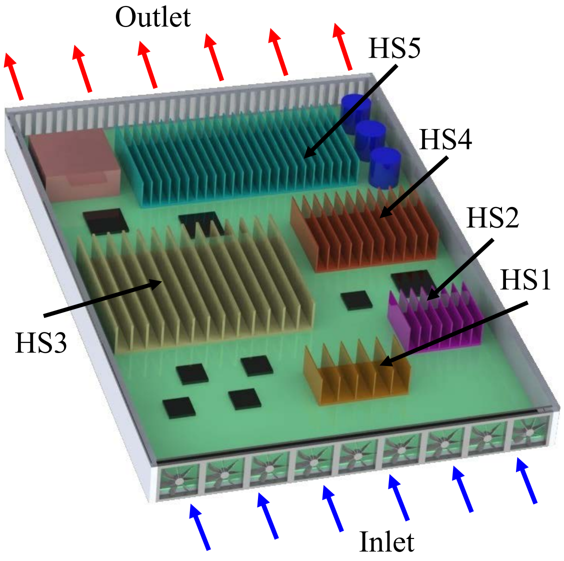

Figure 21.4: Schematic of a circuit pack with five longitudinal-fin heat sinks and several passive components.

Chapter 22

Enabling Methods

22.1 Computational Fluid Dynamics (CFD)

In CFD simulations, the governing nonlinear partial differential equations (PDEs) of the hydrodynamic and conjugate thermal problems are solved numerically on a computational domain that comprises of the geometry of the flow path and that of the heat sinks [61, 58]. For the case at hand, the governing equations for the hydrodynamic problem are the following forms of the continuity and Navier-Stokes Equations

$$\begin{aligned} \nabla \cdot \mathbf{U} &= 0 && (22.1) \\ \rho \left(\mathbf{U} \cdot \nabla \right) \mathbf{U} &= -\nabla p + \mu \nabla^2 \mathbf{U} && (22.2) \end{aligned}$$

respectively, where p is the pressure and

$$\mathbf{U} = \begin{bmatrix} u \\ v \\ w \end{bmatrix} \tag{22.3}$$

is the velocity vector where u, v and w are the velocity components in the x, y and z-direction, respectively. The boundary conditions are determined based on the characteristics of each particular application and usually include that of no-slip along the solid-coolant interfaces, and those of a prescribed velocity profile and pressure at the inlet and outlet of the computational domain, respectively.

The governing equations for the conjugate thermal problem for the coolant and the solid, i.e, the heat sinks in this case, are

$$\rho c_p \mathbf{U} \cdot \nabla T = k \nabla^2 T \tag{22.4}$$

$$\nabla^2 T_{\mathrm{f}} = 0 \tag{22.5}$$

respectively, where T and T_{f} are the coolant and fin temperature fields, respectively. Common boundary conditions for the conjugate thermal problem include that of prescribed temperature profile and zero temperature gradient at the inlet and outlet of the computational domain, respectively, and those of prescribed temperature or heat flux at the rest of the external boundaries. At the internal boundaries formed at the solid-coolant interfaces a conjugate boundary condition applies that imposes continuity of the temperature and heat flux fields, i.e., $T = T_{\mathrm{f}}$ and $K_{\mathrm{f}} \partial T / \partial \mathbf{n} = \partial T_{\mathrm{f}} / \partial \mathbf{n}$, where $\mathbf{n}$ is the unit normal vector along these interfaces. As such, CFD simulations fully resolve the velocity and temperature fields within a circuit pack.

The aspect of CFD that allows the numerical solution of the governing PDE's is a step where the equations are discretized spatially (and temporally when applicable) to be transformed into a linear system of equations. The two most common discretization techniques are the Finite Volume Method (FVM) and the Finite Element Method (FEM). Despite the apparent flexibility that the discretization lends to CFD, however, it is also its bottleneck. The accuracy of CFD simulations is based upon factors such as the quality, distribution and density of the discretization, i.e., the mesh. Of them, the mesh density is the factor with the highest impact on the computational time and resources needed. A circuit pack typically needs to be discretized with a few hundred thousand to up to tens of millions of computational elements with each solid and coolant computational element contributing one and five equations, respectively, to the system of equations to be solved. Thus, the resulting system of equations is very cumbersome and time consuming to solve, requiring from tens of minutes to days per simulation. As such, although a rigorous brute-force optimization of all the heat sinks in a circuit pack is in principle possible by performing a series of CFD simulations, the computational time is prohibitively long. For example, if such an optimization considers only two different values for the fin spacing, thickness, and length of each of the five heat sinks in the circuit pack of Fig. 21.4, a total of 32,768 CFD models needs to be executed.

However, the approach presented in Karamanis and Hodes [2] allows one to perform banks of CFD simulations to compute accurate conjugate Nusselt numbers for simultaneously developing flows for the computational domain in Fig. 21.3, over a wide range of operating conditions of longitudinal-fin heat sinks in circuit packs. These results, then, allow one to perform a rigorous multi-variable optimization as discussed in the following two subsections. Of course, the computational domain in Fig. 21.3 does not capture minor losses as does a CFD simulation of the full circuit pack. Instead, it was chosen to maximize the accuracy of the computed conjugate Nu for half of a fin and half of an adjacent gap through which coolant flows, which is used to estimate the thermal resistance of a heat sink during the optimization. As such, if minor losses are important, the results from the proposed optimization algorithm can be further refined using CFD.

22.2 Flow network modeling (FNM)

In FNM, a circuit pack is separated into distinct sub-regions [62], as per Fig. 22.1a. A flow ($R_{\mathrm{h},i}$) and a thermal ($R_{\mathrm{t},i}$) resistance is computed for each sub-region, and the circuit pack is mathematically represented as networks of them, as per Fig. 22.1b.

The resulting system of equations is small since each sub-region contributes only two equations to the system of equations to be solved, one to the hydrodynamic problem, and one to the thermal one as per

$$V_i = \frac{p_{\mathrm{in},i} - p_{\mathrm{out},i}}{R_{\mathrm{h},i}} \tag{22.6}$$

$$q_i = \frac{T_{\mathrm{max},i} - T_{\mathrm{in},i}}{R_{\mathrm{t},i}} \tag{22.7}$$

respectively, where $p_{\mathrm{in},i}$, $p_{\mathrm{out},i}$, and V_i are the inlet and outlet pressures of the i-th sub-region and the corresponding volumetric flow rate, respectively. $T_{\mathrm{max},i}$ is the maximum temperature occurring at the boundaries of the i-th sub-region, e.g., the prescribed temperature $T_{\mathrm{B,HS}i}$ of the isothermal base of the i-th heat sink. $T_{\mathrm{in},i}$ and q_i are the bulk temperature of the coolant at the inlet of the i-th sub-region and the corresponding heat rate, respectively. Additionally, each node at the interface between sub-regions contributes to the system of equations to be solved, one equation to conserve mass and one more to conserve thermal energy as per

$$\sum V_i = 0 \tag{22.8}$$

$$\sum q_i = 0 \tag{22.9}$$

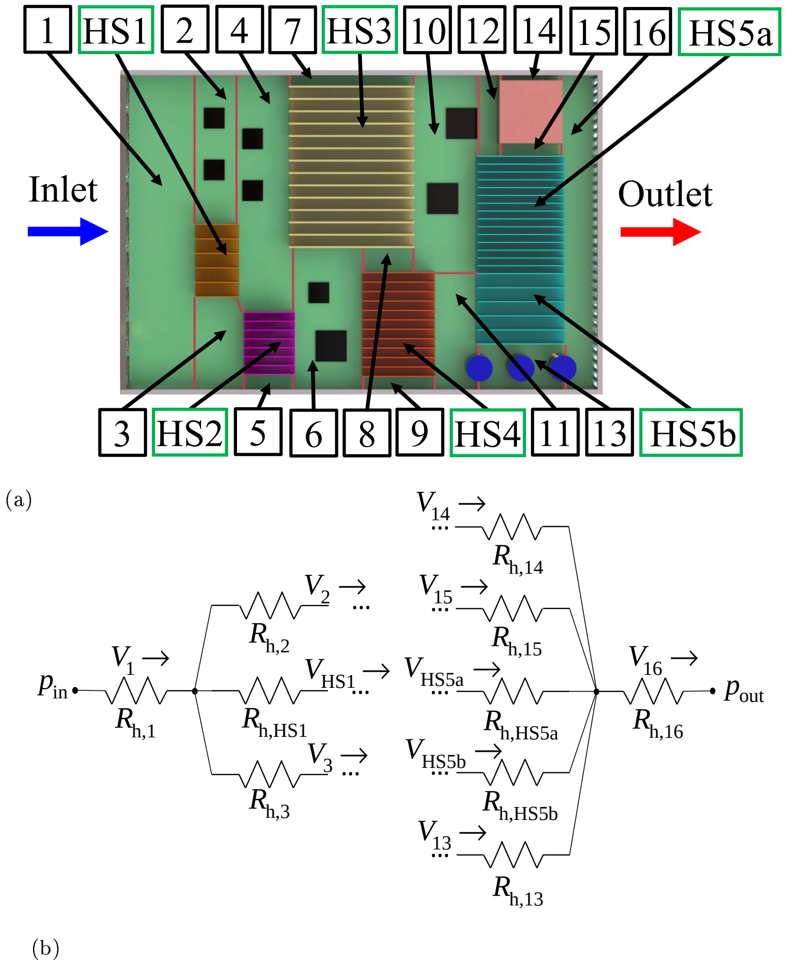

Figure 22.1: (a) FNM sub-regions and (b) flow resistance network representation of circuit pack in Fig. 21.4.

respectively. The bulk temperature of the coolant at the outlet of each sub-region follows from an energy balance per

$$T_{\text{out},i} = T_{\text{in},i} + \frac{q_i}{\rho c_p V_i} \tag{22.10}$$

Despite $R_{\text{h},i}$ and $R_{\text{t},i}$ being nonlinear with respect to V_i, such systems of algebraic equations are trivial to solve numerically.

The flow and thermal resistances of each sub-region, e.g., $1 - 16$ in Fig. 22.1a, are computed using correlations for major and minor losses [63, 64] or CFD results. The heat sinks can be further subdivided as per HS5a and HS5b in Fig. 22.1a to increase accuracy. The flow and thermal resistances of the heat sinks are commonly acquired either from experimental measurements that are accurate but apply over limited parameter ranges, or they are computed based on the often-poor assumption of a uniform heat transfer coefficient along the fins [1]. As such, an optimization of a circuit pack based upon conventional brute-force FNM executions is limited by the accuracy of the expressions used to predict the flow and thermal resistances of the heat sinks for arbitrary fin geometry.

Here, we increase the accuracy of FNM by using accurate CFD-precomputed conjugate Nusselt numbers for the heat sinks from Karamanis and Hodes [2]. The corresponding Poiseuille numbers can be computed from available expressions in the literature[42], but here they are obtained from the CFD models that were executed to tabulate the conjugate Nusselt number. The Poiseuille and conjugate Nusselt numbers of the i-th heat sink are defined by the expressions

$$\mathrm{Po}_{\mathrm{HS}i} = 2\frac{A_{\mathrm{cs,HS}i} D^2_{\mathrm{h,HS}i} \left(p_{\mathrm{in,HS}i} - p_{\mathrm{out,HS}i}\right)}{\mu L_{\mathrm{HS}i} V_{\mathrm{HS}i}} \tag{22.11}$$

$$\mathrm{Nu}_{\mathrm{HS}i} = \frac{q_{\mathrm{HS}i} D_{\mathrm{h,HS}i}}{k A_{\mathrm{fp,HS}i} \left(T_{\mathrm{B,HS}i} - T_{\mathrm{in,HS}i}\right)} \tag{22.12}$$

respectively, where

$$A_{\mathrm{cs,HS}i} = \frac{\left(W_{\mathrm{HS}i} - t_{\mathrm{HS}i}\right) s_{\mathrm{HS}i} H_{\mathrm{HS}i}}{\left(s_{\mathrm{HS}i} + t_{\mathrm{HS}i}\right)} \tag{22.13}$$

$$A_{\mathrm{fp,HS}i} = W_{\mathrm{HS}i} L_{\mathrm{HS}i} \tag{22.14}$$

are the cross-sectional area of the flow and the footprint of the heat sink, respectively. $W_{\mathrm{HS}i}$ is the width of the i-th heat sink. Combining Eqs. (22.6) and (22.11) and Eqs. (22.7) and (22.12), it follows that the dimensional flow and thermal resistances of the i-th heat sink are given by the expressions

$$R_{\mathrm{h,HS}i} = \frac{\mu L_{\mathrm{HS}i} \mathrm{Po}_{\mathrm{HS}i}}{2 A_{\mathrm{cs,HS}i} D^2_{\mathrm{h,HS}i}} \tag{22.15}$$

$$R_{\mathrm{t,HS}i} = \frac{D_{\mathrm{h,HS}i}}{k A_{\mathrm{fp,HS}i} \mathrm{Nu}_{\mathrm{HS}i}} \tag{22.16}$$

respectively.

22.3 Multi-Variable Optimization (MVO)

Both CFD and FNM are methods to compute the thermal performance of circuit packs, but they do not inherently provide a means to rigorously optimize fin geometries. Even a brute-force approach is too slow with CFD and not accurate with FNM, as previously explained. Here we complement their utility with MVO by which we refer to the suite of mathematical methods that solve problems of the form

$$\min_{\mathbf{x}} F\left(x_1, x_2, \ldots, x_n\right) \tag{22.17}$$

subject to

$$\mathbf{c}\left(x_1, x_2, \ldots, x_n\right) = 0 \tag{22.18}$$

$$\mathbf{g}\left(x_1, x_2, \ldots, x_n\right) \leq 0 \tag{22.19}$$

where F, $\mathbf{x}$, $\mathbf{c}$, and $\mathbf{g}$ are the scalar-valued objective function, and the vectors of the independent variables and of the equality and inequality constraints, respectively, and F, $\mathbf{c}$ and $\mathbf{g}$ are nonlinear in general.

In the context of the thermal management of electronics, F can be, e.g., the inverse of the total heat dissipated by a circuit pack, if the objective is to maximize the total heat dissipated from the circuit pack for prescribed pressure drop across the circuit pack and inlet coolant temperature. In such a case, $\mathbf{c}$ will be comprised of the system of equations for the hydrodynamic and thermal problems, i.e., the so called implicit constraints, along with any equality constraints that are relevant to the particular case, e.g., fixed heat sink footprint. Moreover, $\mathbf{g}$ will be comprised of the set of the relevant inequality constraints to, e.g., satisfy manufacturing and/or cost constraints, on, e.g., the fin spacing and thickness.

A large number of mathematical methods can be used to perform such an optimization [65]. Here, we use the Barrier Function method (or Interior Point method) in conjunction with the Trust Region method and the Conjugate Gradient method [66] for three reasons. The first one is that this approach makes no assumptions about the objective function and the constraints, hence, they can be arbitrary and non-linear. The second reason is that this method accommodates the usually large number of inequality constraints for typical thermal management applications. The third reason is that this approach is numerically robust [65].

Chapter 23

CFM

Having discussed the three enabling methods in CFM, we proceed with an example to demonstrate it. Figure 23.1 shows the circuit pack under consideration where two fully-shrouded, longitudinal-fin heat sinks are mounted in series. We emphasize that we use this simple example here as opposed to the circuit pack in Fig. 21.4 to reduce the number of equations involved in the optimization for demonstration purposes, but we do not lose generality. The upstream and downstream heat sinks are made out of copper ($k_{\mathrm{HS1}} = 401\,\mathrm{W/(mK)}$) and aluminum ($k_{\mathrm{HS2}} = 237\,\mathrm{W/(mK)}$), respectively. They are cooled by air ($\rho = 1.1614\,\mathrm{kg/m^3}$, $c_p = 1007\,\mathrm{J/kgK}$, $k = 26.3\mathrm{E}-3\,\mathrm{W/(mK)}$, $\mu = 1.85E-05\,\mathrm{Pa\cdot s}$) with $T_{\mathrm{in,CP}} = 27\,^{\mathrm{o}}\mathrm{C}$ at the inlet of the circuit pack. The pressure drop across the circuit pack is $p_{\mathrm{in,CP}} - p_{\mathrm{out,CP}} = 40\,\mathrm{Pa}$. The bases of the heat sinks are isothermal at $T_{\mathrm{B,HS1}} = 52\,^{\mathrm{o}}\mathrm{C}$ and $T_{\mathrm{B,HS2}} = 62\,^{\mathrm{o}}\mathrm{C}$. The width and height of the heat sinks are $W_{\mathrm{HS1}} = W_{\mathrm{HS2}} = 55.2\,\mathrm{mm}$ and $H_{\mathrm{HS1}} = H_{\mathrm{HS2}} = 30.0\,\mathrm{mm}$. The objective here is to compute the fin spacing, thickness and length for each heat sink, i.e., the values of the independent variables $\mathbf{x} = [s_{\mathrm{HS1}}, s_{\mathrm{HS2}}, t_{\mathrm{HS1}}, t_{\mathrm{HS2}}, L_{\mathrm{HS1}}, L_{\mathrm{HS2}}]^T$, that maximize the total heat dissipated by the two heat sinks, i.e., $(q_{\mathrm{HS1}} + q_{\mathrm{HS2}})$, while maintaining the values for the aforementioned independent variables within the operating envelope covered by the tabulations for $\mathrm{Po}_{\mathrm{HS}i}$ and $\mathrm{Nu}_{\mathrm{HS}i}$ in [2], i.e., using the box constraints

$$s_{\mathrm{min,HS}i} = 1\,\mathrm{mm} \leq \quad s_{\mathrm{HS}i} \quad \leq s_{\mathrm{max,HS}i} = 4\,\mathrm{mm} \tag{23.1}$$

$$t_{\mathrm{min,HS}i} = 0.2\,\mathrm{mm} \leq \quad t_{\mathrm{HS}i} \quad \leq t_{\mathrm{max,HS}i} = 1\,\mathrm{mm} \tag{23.2}$$

$$L_{\mathrm{min,HS}i} = 40\,\mathrm{mm} \leq \quad L_{\mathrm{HS}i} \quad \leq L_{\mathrm{max,HS}i} = 100\,\mathrm{mm} \tag{23.3}$$

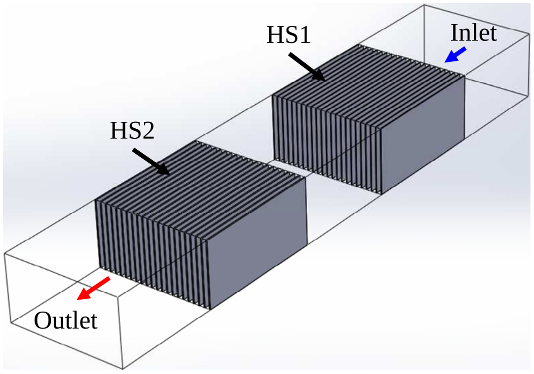

Figure 23.1: CFM example circuit pack.

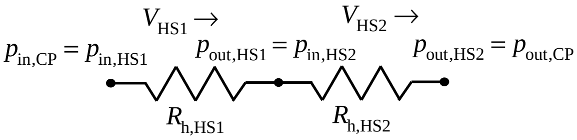

Figure 23.2: Hydrodynamic FNM representation of circuit pack in Fig. 23.1.

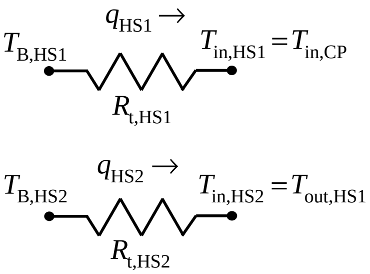

Figure 23.3: Thermal FNM representation of circuit pack in Fig. 23.1.

Also, for simplicity, the secondary pressure losses and heat transfer upstream, midway, and downstream of the heat sinks are assumed to be negligible. The hydrodynamic and thermal FNM representations of the circuit pack are presented in Figs. 23.2 and 23.3, respectively.

To proceed with the CFM optimization, the mathematical description of the optimization problem has to be constructed first. For the case at hand, the optimization problem takes the form

$$\min_{\mathbf{x}} \left[\frac{1}{q_{\text{HS1}} + q_{\text{HS2}}} \right] \tag{23.4}$$

subject to the equality constraints

$$p_{\mathrm{in,CP}} - p_{\mathrm{in,HS1}} = 0 \tag{23.5}$$

$$p_{\mathrm{in,HS1}} - p_{\mathrm{out,HS1}} - R_{\mathrm{h,HS1}} V_{\mathrm{HS1}} = 0 \tag{23.6}$$

$$V_{\mathrm{HS1}} - V_{\mathrm{HS2}} = 0 \tag{23.7}$$

$$p_{\mathrm{out,HS1}} - p_{\mathrm{in,HS2}} = 0 \tag{23.8}$$

$$p_{\mathrm{in,HS2}} - p_{\mathrm{out,HS2}} - R_{\mathrm{h,HS2}} V_{\mathrm{HS2}} = 0 \tag{23.9}$$

$$p_{\mathrm{out,HS2}} - p_{\mathrm{out,CP}} = 0 \tag{23.10}$$

$$T_{\mathrm{in,HS1}} - T_{\mathrm{in,CP}} = 0 \tag{23.11}$$

$$T_{\mathrm{B,HS1}} - T_{\mathrm{in,HS1}} - R_{\mathrm{t,HS1}} q_{\mathrm{HS1}} = 0 \tag{23.12}$$

$$T_{\mathrm{out,HS1}} - T_{\mathrm{in,HS1}} - \frac{q_{\mathrm{HS1}}}{\rho c_p V_{\mathrm{HS1}}} = 0 \tag{23.13}$$

$$T_{\mathrm{in,HS2}} - T_{\mathrm{out,HS1}} = 0 \tag{23.14}$$

$$T_{\mathrm{B,HS2}} - T_{\mathrm{in,HS2}} - R_{\mathrm{t,HS2}} q_{\mathrm{HS2}} = 0 \tag{23.15}$$

and to the inequality constraints

$$s_{\mathrm{min,HS1}} - s_{\mathrm{HS1}} \leq 0 \tag{23.16}$$

$$s_{\mathrm{HS1}} - s_{\mathrm{max,HS1}} \leq 0 \tag{23.17}$$

$$s_{\mathrm{min,HS2}} - s_{\mathrm{HS2}} \leq 0 \tag{23.18}$$

$$s_{\mathrm{HS2}} - s_{\mathrm{max,HS2}} \leq 0 \tag{23.19}$$

$$t_{\mathrm{min,HS1}} - t_{\mathrm{HS1}} \leq 0 \tag{23.20}$$

$$t_{\mathrm{HS1}} - t_{\mathrm{max,HS1}} \leq 0 \tag{23.21}$$

$$t_{\mathrm{min,HS2}} - t_{\mathrm{HS2}} \leq 0 \tag{23.22}$$

$$t_{\mathrm{HS2}} - t_{\mathrm{max,HS2}} \leq 0 \tag{23.23}$$

$$L_{\mathrm{min,HS1}} - L_{\mathrm{HS1}} \leq 0 \tag{23.24}$$

$$L_{\mathrm{HS1}} - L_{\mathrm{max,HS1}} \leq 0 \tag{23.25}$$

$$L_{\mathrm{min,HS2}} - L_{\mathrm{HS2}} \leq 0 \tag{23.26}$$

$$L_{\mathrm{HS2}} - L_{\mathrm{max,HS2}} \leq 0 \tag{23.27}$$

The equality constraints given by Eqs. (23.5)-(23.15) are implicit constraints; Eqs. (23.5)-(23.10) and Eqs. (23.11)-(23.15) follow from the hydrodynamic and thermal FNM representations of the circuit pack, as per Figs. 23.2 and 23.3, respectively. They constitute a well posed system of 11 nonlinear algebraic equations with 11 unknowns, namely: $p_{\text{in,HS1}}$, $p_{\text{out,HS1}}$, V_{HS1}, $p_{\text{in,HS2}}$, $p_{\text{out,HS2}}$, V_{HS2}, $T_{\text{in,HS1}}$, $T_{\text{out,HS1}}$, q_{HS1}, $T_{\text{in,HS2}}$ and q_{HS2}. It is noted that an additional equation for $T_{\text{out,HS2}}$ is not required. The inequality constraints given by inequalities (23.16)-(23.27) follow from the box constraints for the independent variables given by inequalities (23.1)-(23.3).

Next, the original equality-inequality-constrained optimization problem described by Eqs. (23.4)-(23.27) is transformed into a solely equality-constrained problem using the Barrier Function method. As such, Eq. (23.4) becomes

$$\min_{\mathbf{x}} \left[\frac{1}{q_{\text{HS1}} + q_{\text{HS2}}} - \kappa \sum_{m=1}^{12} \ln\left(\beta_i\right) \right] \tag{23.28}$$

where $\kappa > 0$ and $\beta_i > 0$ are the barrier parameter and slack variables, respectively. Equation (23.28) is subject to the original equality constraints given by Eqs. (23.5)-(23.15), to the equality constraints following from the transformed inequality constraints given by inequalities (23.16)-(23.27)

$$\begin{aligned}
s_{\text{min,HS1}} - s_{\text{HS1}} + \beta_1 &= 0 && (23.29)\\
s_{\text{HS1}} - s_{\text{max,HS1}} + \beta_2 &= 0 && (23.30)\\
s_{\text{min,HS2}} - s_{\text{HS2}} + \beta_3 &= 0 && (23.31)\\
s_{\text{HS2}} - s_{\text{max,HS2}} + \beta_4 &= 0 && (23.32)\\
t_{\text{min,HS1}} - t_{\text{HS1}} + \beta_5 &= 0 && (23.33)\\
t_{\text{HS1}} - t_{\text{max,HS1}} + \beta_6 &= 0 && (23.34)\\
t_{\text{min,HS2}} - t_{\text{HS2}} + \beta_7 &= 0 && (23.35)\\
t_{\text{HS2}} - t_{\text{max,HS2}} + \beta_8 &= 0 && (23.36)\\
L_{\text{min,HS1}} - L_{\text{HS1}} + \beta_9 &= 0 && (23.37)\\
L_{\text{HS1}} - L_{\text{max,HS1}} + \beta_{10} &= 0 && (23.38)\\
L_{\text{min,HS2}} - L_{\text{HS2}} + \beta_{11} &= 0 && (23.39)\\
L_{\text{HS2}} - L_{\text{max,HS2}} + \beta_{12} &= 0 && (23.40)
\end{aligned}$$

and to the equality constraints that follow from the fact that the β_i associated with the lower and upper boundary of each original box constraint are linearly dependent, i.e.,

$$\beta_1 + \beta_2 + s_{\text{min,HS1}} - s_{\text{max,HS1}} = 0 \tag{23.41}$$

$$\beta_3 + \beta_4 + s_{\text{min,HS2}} - s_{\text{max,HS2}} = 0 \tag{23.42}$$

$$\beta_5 + \beta_6 + t_{\text{min,HS1}} - t_{\text{max,HS1}} = 0 \tag{23.43}$$

$$\beta_7 + \beta_8 + t_{\text{min,HS2}} - t_{\text{max,HS2}} = 0 \tag{23.44}$$

$$\beta_9 + \beta_{10} + L_{\text{min,HS1}} - L_{\text{max,HS1}} = 0 \tag{23.45}$$

$$\beta_{11} + \beta_{12} + L_{\text{min,HS2}} - L_{\text{max,HS2}} = 0 \tag{23.46}$$

This transformation essentially introduces convexity at the boundaries of the original optimization problem given that as we approach a boundary, i.e., $\beta_i \to 0$, $-\ln(\beta_i) \to +\infty$. Moreover, the intensity of the added convexity is controlled by the value of the barrier parameter μ which is gradually reduced to zero during the iterative solution of the modified optimization problem such that the computed optimal values of the independent variables converge to those of the original optimization problem.

The steps of the solution algorithm follow. First, determine an initial set of the estimates of the optimal values of the independent variables $\mathbf{x}_0$, choose an initial value for the barrier parameter κ_0 that ensures numerical stability for the particular problem at hand, and set a convergence threshold e. Then, solve the modified optimization problem described by Eqs. (23.5)-(23.15) and (23.28)-(23.46) to determine the new estimates $\mathbf{x}_j$ using the Trust Region method in conjunction with the Conjugate Gradient method as described in Byrd et al. [66] and employed in MATLAB® [67]. Next, determine if the maximum value of the difference $|\mathbf{x}_j - \mathbf{x}_{j-1}|$ is greater than the convergence threshold e. If it is, set $\kappa_{j+1} = \alpha\kappa_j$, where $0 < \alpha < 1$, and proceed from step two; if not, the computed estimates are deemed converged. The value of α is heuristically determined and follows from a trade-off between convergence speed and numerical stability for lower and higher values of α, respectively.

Table 23.1 provides the baseline and the optimized fin geometries of the heat sinks along with the computed q_{HS1} and q_{HS2}. The results indicate that the optimized fin geometries increased the total heat dissipation of the circuit pack by 5.24%. However, it is emphasized here that the efficacy of an optimization algorithm should not be evaluated on the achieved change of the objective function, given that the baseline is arbitrary and, as such, large performance improvements can be demonstrated by just starting an optimization from a poorly designed baseline. To the contrary, the efficacy of an optimization algorithm should

	Baseline	Optimal
s_{HS1}	2.10 mm	3.60 mm
s_{HS2}	2.00 mm	1.90 mm
t_{HS1}	0.40 mm	0.60 mm
t_{HS2}	0.60 mm	0.58 mm
L_{HS1}	60.0 mm	51.5 mm
L_{HS2}	60.0 mm	93.4 mm
q_{HS1}	71.09 W	37.05 W
q_{HS2}	64.79 W	105.95 W
$q_{\text{HS1}} + q_{\text{HS2}}$	135.89 W	143.00 W

Table 23.1: Fin geometries and optimization example results.

be evaluated based upon its speed and accuracy. Regarding speed, the optimization for the case at hand required less than five minutes on a common desktop computer. Regarding accuracy, the results of the baseline and the optimized geometries were validated using the general CFD solver FLUENT [58], and the maximum discrepancy was found to be less than 4%. Precisely, the discrepancies for q_{HS1} and q_{HS2} for the baseline geometries were found to be 1.34% and 0.18%, respectively, and for the optimized geometries 1.56% and 3.71%, respectively. The larger discrepancy of q_{HS2} for the optimized geometries is because the tables of $\text{Po}_{\text{HS}i}$ and $\text{Nu}_{\text{HS}i}$ are not dense enough at that particular parameter space.

Overall, the example demonstrates how CFM can be implemented to perform a rigorous optimization of an array of heat sinks using an arbitrary objective function and constraints. However, care should be exercised when using this algorithm for two reasons. The first reason is that the algorithm makes no assumptions and as such both the objective function and the constraints should be carefully determined for the optimization to be practically successful. The presented example was selected particularly to demonstrate this issue; despite the fact that the total heat dissipation of the circuit pack, i.e., $(q_{\text{HS1}} + q_{\text{HS2}})$, increased after the optimization, q_{HS1} actually decreased. If such a decrease is unacceptable in a different scenario, an additional inequality constraint must be included for each heat sink to impose that the heat dissipation rate of the optimized geometry must be higher than that of its baseline. The second reason that care should be exercised is that CFM does not guarantee convergence towards the global optimum. Therefore, the optimization should be executed starting from different initial values of the independent variables to ensure that the computed optimum is indeed the global one.

Chapter 24

Conclusions

We have shown that the hybridization of Computational Fluid Dynamics (CFD), Flow Network Modeling (FNM), and Multi-Variable Optimization (MVO) enables one to optimize the geometry of an array of longitudinal-fin heat sinks in a laminar flow. The CFD part of the algorithm computes dimensionless flow resistances (Poiseuille number) and dimensionless thermal resistances (Nusselt number) for the heat sinks as a function of the relevant geometric, thermophysical, and external parameters. Then, a circuit pack, e.g., a blade server, is represented as a FNM, as is common practice. The heat sinks within this FNM are linked to the precomputed Poiseuille and conjugate Nusselt numbers such that the FNM may be rapidly solved for arbitrary heat sink geometry. Indeed, the solutions to the governing nonlinear partial differential equations are precomputed, and solving the FNM only requires the solution to an algebraic system of equations. Thus, the presented approach preserves much of the accuracy of CFD, within rapidly-soluble FNM models. This, in turn, makes it realistic to embed FNM models in an MVO to simultaneously optimize the fin thickness, spacing, height and length in an array of heat sinks, as was shown by an example. This is not possible to do with a brute-force CFD approach, and not sufficiently accurate with a conventional FNM approach. Moreover, CFD can be used to further refine the predicted optimal fin geometries from CFM.

Nomenclature

$A_{\mathrm{cs,HS}i}$	heat sink cross-sectional area of flow, m^2
$A_{\mathrm{fp,HS}i}$	heat sink foot-print, m^2
W	heat sink width, m
$\mathbf{c}$	vector of equality constraints
c_p	specific heat at constant pressure, J/(kg K)
D_{h}	hydraulic diameter; $(2sH)/(s+H)$
F	objective function
$\mathbf{g}$	vector of inequality constraints
H	fin height, m
k	thermal conductivity of fluid, W/(m K)
K_{f}	coolant-to-fin thermal conductivity ratio; k/k_{f}
k_{f}	fin thermal conductivity, W/(m K)
L	heat sink length, m
$\tilde{L}$	dimensionless heat sink length; L/D_{h}
$\mathrm{Nu}_{\mathrm{HS}i}$	heat sink conjugate Nusselt number defined by Eq. 19
p	pressure, Pa
$p_{\mathrm{in},i}$	i-th sub-region inlet pressure, Pa

$p_{\text{out},i}$	i-th sub-region outlet pressure, Pa
Po_{HSi}	heat sink Poiseuille number defined by Eq. 18
Pr	Prandtl number; $c_p\mu/k$
q_i	i-th sub-region heat rate, W
Re_{D_h}	Reynolds number based on D_h; $\left(\rho\bar{w}D_h\right)/\mu$
$R_{\text{h},i}$	i-th sub-region flow resistance, Pa/(m^3/s)
$R_{\text{t},i}$	i-th sub-region thermal resistance, °C/W
s	fin spacing, m
$\tilde{s}$	dimensionless fin spacing; s/D_h
T	fluid temperature, °C
t	fin thickness, m
$T_{\text{in},i}$	i-th sub-region inlet temperature, °C
$T_{\text{out},i}$	i-th sub-region outlet temperature, °C
$T_{\text{B,HS}i}$	temperature of heat sink base, °C
T_f	fin temperature, °C
$T_{\text{max},i}$	maximum temperature on boundaries of i-th sub-region, °C
$\tilde{t}$	dimensionless fin thickness; t/D_h
u	velocity component x-direction, m/s
v	velocity component y-direction, m/s
V_i	i-th sub-region volumetric flow rate, m^3/s
w	velocity component z-direction, m/s
$\bar{w}$	flow mean velocity, m/s
$\mathbf{x}$	vector of independent variables
x	lateral coordinate, m

y	vertical coordinate, m
z	streamwise coordinate, m

Greek Symbols

β	slack variable
κ	barrier parameter
μ	dynamic viscosity, $\mathrm{Pa} \cdot \mathrm{s}$
ρ	fluid density, $\mathrm{kg/m^3}$

Part VI

Appendix

Appendix A

The following two Subsections of the Appendix provide the necessary information for the extension of the present analysis to the configurations when both plates are textured with parallel ridges and the ridges are either aligned or staggered, respectively. Each subsection covers the cases when the ridges of one plate are isothermal and those of the other one are either adiabatic or isothermal.

Both Plates Textured, Aligned Ridges

When both plates are textured and the ridges are aligned as indicated in Fig. 2.3, the boundary conditions for the hydrodynamic problem given by Eqs. (3.7) and (3.8) apply rather than Eq. (3.9) at $\tilde{y} = \tilde{H}$. The computed Poiseuille numbers are presented in Fig. 25.1.

If only the lower plate has isothermal ridges and the upper one has adiabatic ridges, the boundary conditions for the thermal problem and for the eigenvalue problem are identical to those in Section 3.2. The expressions for $\mathrm{Nu_l}$, $\mathrm{Nu_{l,fd}}$, Nu, $\mathrm{Nu_{fd}}$, $\overline{\mathrm{Nu}}$ and $\overline{\mathrm{Nu}}_{\mathrm{UIT}}$ are identical to those given by Eqs. (4.6), (4.7), (4.13), (4.14), (4.16), (4.17) and the reader is referred to those expressions for their detailed form. The computed $\mathrm{Nu_{fd}}$ is presented in Fig. 25.2.

If the ridges of both plates are isothermal, the thermal boundary conditions given by Eqs. (3.20) and (3.21) apply rather than Eq. (3.22) at $\tilde{y} = \tilde{H}$. In terms of the eigenvalue problem, the boundary conditions given by Eqs. (3.26) and (3.27) apply rather than Eq. (3.28) at $\tilde{y} = \tilde{H}$.

In this case, the expressions for $\mathrm{Nu_l}$ and $\mathrm{Nu_{l,fd}}$ are identical to those given by Eqs. (4.6) and (4.7). However, the Nusselt number averaged over the composite interfaces is

$$\mathrm{Nu} = \frac{1}{2d}\int_{-d}^{d} \mathrm{Nu_l}\big|_{\tilde{y}=0}\,\mathrm{d}x + \frac{1}{2d}\int_{-d}^{d} \mathrm{Nu_l}\big|_{\tilde{y}=\tilde{H}}\,\mathrm{d}x \tag{25.1}$$

Moreover, following the same steps as in Section 4, it follows that

$$\int_{1}^{\tilde{d}} \left.\frac{\partial \psi_i}{\partial \tilde{y}}\right|_{\tilde{y}=0} \mathrm{d}\tilde{x} = \frac{\lambda_i}{4}\,\langle \psi_i, 1\rangle \tag{25.2}$$

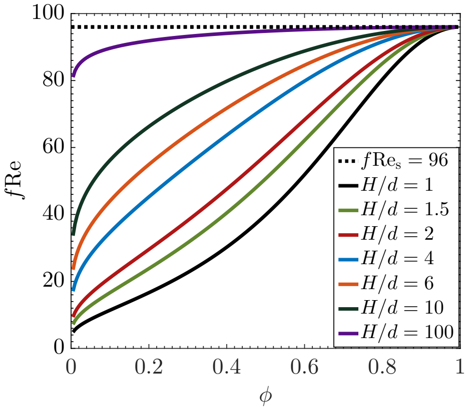

Figure 25.1: fRe vs. ϕ for selected H/d when both plates are textured and the ridges are aligned.

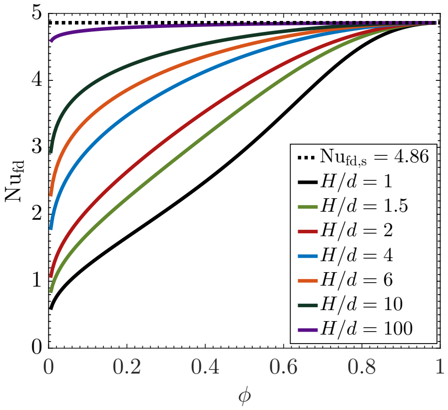

Figure 25.2: Nu_fd vs. ϕ for selected H/d when the ridges of one plate are isothermal and the ridges of the other one are aligned and adiabatic.

Thus, the expressions for the values of the Nusselt numbers take the form

$$\mathrm{Nu} = 16\frac{\tilde{H}^3}{f\mathrm{Re}}\frac{\sum\limits_{i=1}^{\infty}\left\langle\psi_i,\tilde{T}_\mathrm{in}\right\rangle\langle\psi_i,1\rangle\,\lambda_i\exp\left(-\lambda_i\tilde{z}\right)}{\sum\limits_{i=1}^{\infty}\left\langle\psi_i,\tilde{T}_\mathrm{in}\right\rangle\langle\psi_i,1\rangle\exp\left(-\lambda_i\tilde{z}\right)} \tag{25.3}$$

$$\mathrm{Nu}_\mathrm{fd} = 16\frac{\tilde{H}^3}{f\mathrm{Re}}\lambda_1 \tag{25.4}$$

$$\overline{\mathrm{Nu}} = 16\frac{\tilde{H}^3}{\tilde{z}f\mathrm{Re}}\ln\left(\frac{\sum\limits_{i=1}^{\infty}\left\langle\psi_i,\tilde{T}_\mathrm{in}\right\rangle\langle\psi_i,1\rangle}{\sum\limits_{i=1}^{\infty}\left\langle\psi_i,\tilde{T}_\mathrm{in}\right\rangle\langle\psi_i,1\rangle\exp\left(-\lambda_i\tilde{z}\right)}\right) \tag{25.5}$$

$$\overline{\mathrm{Nu}}_\mathrm{UIT} = 16\frac{\tilde{H}^3}{\tilde{z}f\mathrm{Re}}\ln\left(\frac{1}{\tilde{T}_\mathrm{b}}\right) \tag{25.6}$$

The computed Nu_fd is presented in Fig. 25.3.

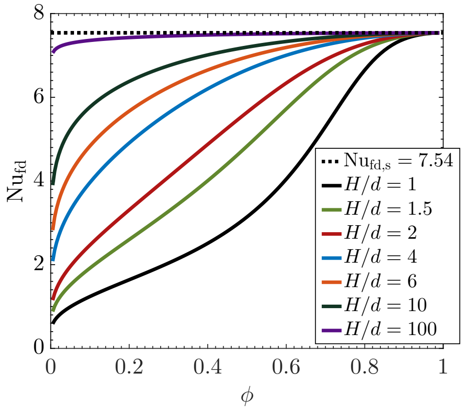

Figure 25.3: $\mathrm{Nu_{fd}}$ vs. ϕ for selected H/d when the ridges of both plates are isothermal and aligned.

Both Plates Textured, Staggered Ridges

When both plates are textured and the ridges are staggered in the transverse direction by half a pitch as shown in Fig. 2.4, the relevant boundary conditions for the hydrodynamic problem become

$$\frac{\partial \tilde{w}}{\partial \tilde{y}} = 0 \quad \text{for } |\tilde{x}| < 1,\ \tilde{y} = 0 \tag{25.7}$$

$$\tilde{w} = 0 \quad \text{for } 1 < |\tilde{x}| < \tilde{d},\ \tilde{y} = 0 \tag{25.8}$$

$$\frac{\partial \tilde{w}}{\partial \tilde{y}} = 0 \quad \text{for } \tilde{d} - 1 < |\tilde{x}| < \tilde{d},\ \tilde{y} = \tilde{H} \tag{25.9}$$

$$\tilde{w} = 0 \quad \text{for } |\tilde{x}| < \tilde{d} - 1,\ \tilde{y} = \tilde{H} \tag{25.10}$$

$$\frac{\partial \tilde{w}}{\partial \tilde{x}} = 0 \quad \text{for } |\tilde{x}| = \tilde{d},\ 0 < \tilde{y} < \tilde{H} \tag{25.11}$$

The computed Poiseuille numbers are presented in Fig. 25.4. Figure 25.5 presents the contour plot of the scaled dimensionless streamwise velocity $\tilde{w}/\overline{\tilde{w}}$ for this case.

If only the lower plate has isothermal ridges and the upper one has adiabatic ridges, the boundary conditions for the thermal problem and for the eigenvalue problem are identical to those in Section 3.2. The expressions for $\mathrm{Nu_l}$, $\mathrm{Nu_{l,fd}}$, Nu, $\mathrm{Nu_{fd}}$, $\overline{\mathrm{Nu}}$ and $\overline{\mathrm{Nu}}_{\mathrm{UIT}}$ are identical to those given by Eqs. (4.6), (4.7), (4.13), (4.14), (4.16), (4.17). The computed $\mathrm{Nu_{fd}}$ is presented in Fig. 25.6.

When the ridges on both plates are isothermal, the boundary conditions for the thermal problem become

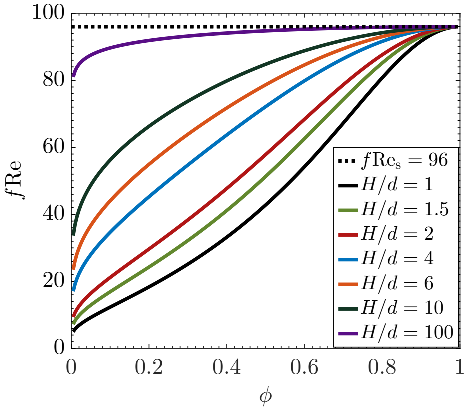

Figure 25.4: fRe vs. ϕ for selected H/d when both plates are textured and the ridges are staggered by half a pitch.

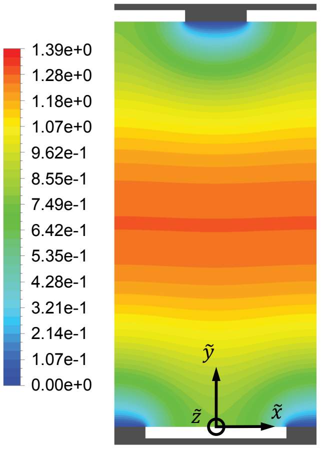

Figure 25.5: Contour plot of $\tilde{w}/\overline{\tilde{w}}$ when both plates are textured and the ridges are staggered by half a pitch for $H/d = 4$ and $\phi = 0.3$.

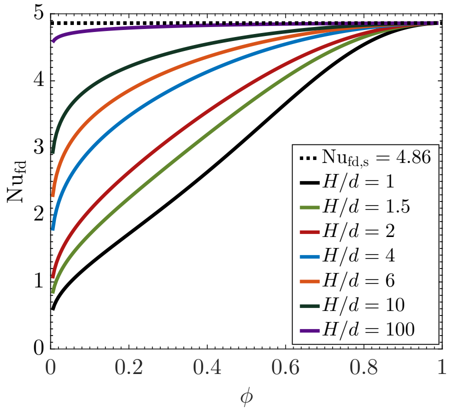

Figure 25.6: Nu_fd vs. ϕ for selected H/d when the ridges of one plate are isothermal and the ridges of the other one are staggered by half a pitch and adiabatic.

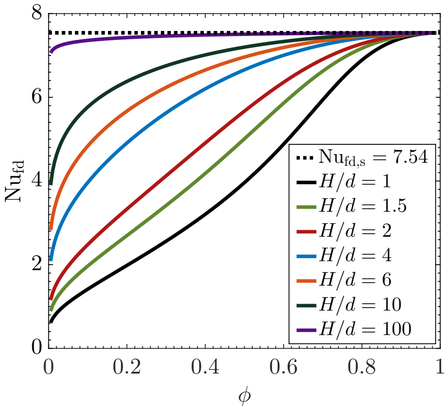

Figure 25.7: $\mathrm{Nu_{fd}}$ vs. ϕ for selected H/d when the ridges of both plates are isothermal and staggered by half a pitch.

$$\frac{\partial \tilde{T}}{\partial \tilde{y}} = 0 \quad \text{for } |\tilde{x}| < 1,\ \tilde{y} = 0 \tag{25.12}$$

$$\tilde{T} = 0 \quad \text{for } 1 < |\tilde{x}| < \tilde{d},\ \tilde{y} = 0 \tag{25.13}$$

$$\frac{\partial \tilde{T}}{\partial \tilde{y}} = 0 \quad \text{for } \tilde{d} - 1 < |\tilde{x}| < \tilde{d},\ \tilde{y} = \tilde{H} \tag{25.14}$$

$$\tilde{T} = 0 \quad \text{for } |\tilde{x}| < \tilde{d} - 1,\ \tilde{y} = \tilde{H} \tag{25.15}$$

$$\frac{\partial \tilde{T}}{\partial \tilde{x}} = 0 \quad \text{for } |\tilde{x}| = \tilde{d},\ 0 < \tilde{y} < \tilde{H} \tag{25.16}$$

$$\tilde{T} = \tilde{T}_{in} \quad \text{for } \tilde{z} = 0 \tag{25.17}$$

while those of the eigenvalue problem read

$$\frac{\partial \psi_i}{\partial \tilde{y}} = 0 \quad \text{for } |\tilde{x}| < 1,\ \tilde{y} = 0 \tag{25.18}$$

$$\psi_i = 0 \quad \text{for } 1 < |\tilde{x}| < \tilde{d},\ \tilde{y} = 0 \tag{25.19}$$

$$\frac{\partial \psi_i}{\partial \tilde{y}} = 0 \quad \text{for } \tilde{d} - 1 < |\tilde{x}| < \tilde{d},\ \tilde{y} = \tilde{H} \tag{25.20}$$

$$\psi_i = 0 \quad \text{for } |\tilde{x}| < \tilde{d} - 1,\ \tilde{y} = \tilde{H} \tag{25.21}$$

$$\frac{\partial \psi_i}{\partial \tilde{x}} = 0 \quad \text{for } |\tilde{x}| = \tilde{d},\ 0 < \tilde{y} < \tilde{H} \tag{25.22}$$

The expressions for $\mathrm{Nu_l}$, $\mathrm{Nu_{l,fd}}$, Nu, $\mathrm{Nu_{fd}}$, $\overline{\mathrm{Nu}}$ and $\overline{\mathrm{Nu}}_{\mathrm{UIT}}$ are identical to those given by Eqs. (4.6), (4.7), (25.3), (25.4), (25.5) and (25.6). The computed $\mathrm{Nu_{fd}}$ is presented in Fig. 25.7.

Appendix B

The two-dimensional eigenvalue problem defined by Eqs. (3.25)-(3.29) was numerically solved for multiple values of the aspect ratio and the solid fraction of the domain using a finite element method. The solution process is iterative and it was coded in MATLAB® employing the Partial Differential Equation (PDE) Toolbox[68]. The algorithm exploits the symmetry of the hydrodynamic and the eigenvalue problems with respect to the y axis in order to increase computational efficiency; therefore, the boundary conditions given by Eqs. (3.10) and (3.29) were both modified to apply at the $\tilde{x} = 0$ and $\tilde{x} = \tilde{d}$ boundaries.

The steps of the algorithm are as follows. First, the half domain is discretized with an initial number of finite elements. Next, Eq. (3.6) is solved subject to the new form of the boundary conditions given by Eqs. (3.7)-(3.9) to determine the two-dimensional velocity profile $\tilde{w}\left(\tilde{x}, \tilde{y}\right)$ required in Eq. (3.25). Then, Eq. (3.25) subject to the new form of the boundary conditions (3.26)-(3.28) is solved to determine all the eigenvalues in the interval $0 \leq \lambda_i \leq \mathrm{UB}$ along with their corresponding eigenfunctions ψ_i [68]. The upper bound (UB) was varied depending on the number of the eigenvalues sought. (MATLAB® requires prescription of the aforementioned interval for the sought λ_i because it solves the discretized eigenvalue problem by applying the Arnoldi algorithm to a shifted and inverted version of the original pencil [68].) Next, mesh refinement is implemented and the algorithm proceeds from step two until the change in the computed value of $\mathrm{Nu}_{\mathrm{fd}}$ is less than 0.01% - typically this required 3.5×10^5 elements that were adaptively placed in regions of sharp gradients. Finally, the computed eigenfunctions are normalized to satisfy Eq. (3.32).

The computations were validated in four ways. First, computed Poiseuille numbers were compared against those that follow from an analytical solution for the velocity profile by Philip [15] at a solid fraction $\phi = 0.25$ and various values of H/d as per Fig. 25.8; agreement was within 0.006%. Secondly, $f\mathrm{Re}$ and $\mathrm{Nu}_{\mathrm{fd}}$ were computed in the limit of $\phi \to 1$, i.e., for fully developed flow between two smooth parallel plates where one is isothermal and the

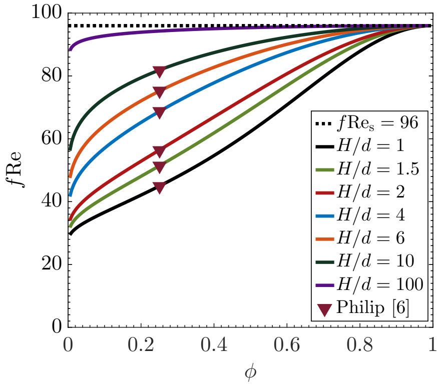

Figure 25.8: fRe vs. ϕ for selected values of H/d when one plate is textured and the other one is smooth.

other is adiabatic and $f\mathrm{Re_s} = 96$ and $\mathrm{Nu_{fd,s}} = 4.86$ [69]. Agreement was within 0.03% of fRe and 0.009% of $\mathrm{Nu_{fd}}$. Thirdly, the boundary condition at $\tilde{y} = \tilde{H}$ was changed to an isothermal one and $\mathrm{Nu_{UIT}}$ and $\overline{\mathrm{Nu}}_{\mathrm{UIT}}$ were computed at various streamwise locations in the limit $\phi \to 1$. The results were compared with those provided by Shah and London [70]. We find that if only 10 terms are used in the series given by Eqs. (4.13) and (4.17), the difference between our results and those provided in [70] were found to be less than 1.4% and 0.3%, respectively, even down to thermal entrance lengths $z^* = 1.5 \times 10^{-4}$.

Lastly, semi-analytical values of $\mathrm{Nu_{fd}}$ were compared with those obtained using FLUENT® [58] which is a general three-dimensional computational fluid dynamics (CFD) solver. This was done for the present case and for those in the Appendix when only one plate has isothermal ridges. Conditions of hydrodynamically and thermally developed flow were imposed by using translational periodic boundary conditions between the inlet and outlet - for details see [71, 58, 31]. The governing equations were discretized using a second-order upwind scheme and were solved using the Pressure-Based Coupled algorithm provided by FLUENT®. The aspect ratio, solid fraction, Reynolds number, and Péclet number were taken to be $H/d = 4$, $\phi = 0.3$, Re $= 2342.89$ and Pe $= 100.87$, respectively. This value of the Péclet number was chosen to enable comparisons with the present analysis which assumes Pe $\gg 1$ given that FLUENT® accounts for axial conduction. This study considers steady flows only and so the solutions obtained are laminar even at Reynolds numbers as high as 2342.89. Adaptive mesh refinement was employed, with the final computational mesh containing as many as 9×10^5 hexahedral elements. The computed $\mathrm{Nu_{fd}}$ for the three geometries mentioned above are 4.124, 3.836 and 3.836 correct to three decimals, and the discrepancy with the predicted values from the analysis are 0.12%, 0.19% and 0.19%. (The aligned and staggered values are almost identical since H/d is large enough and makes the alignment unimportant - see Appendix for more details.)

It is important to note that the present analysis produces results for the $\mathrm{Nu}_{\mathrm{fd}}$ in less than 3 minutes on a desktop computer, whereas FLUENT® requires several hours to converge. Furthermore, it provides the means to evaluate the Nusselt number averaged over the composite interface and, additionally, the streamwise length of the domain at any $\tilde{z}$, quantities which are prohibitively expensive to compute using a general CFD code.

Appendix C

This section provides the necessary information for the extension of the present analysis to the configuration when one plate is textured with isothermal parallel ridges and the other one is smooth and adiabatic, as per Fig. 8.3. The domain in the present case is symmetric with respect to the yz plane through $x = 0$ and therefore we further restrict to $0 \leq x \leq d$ and $0 \leq y \leq H$.

The relevant boundary conditions for the hydrodynamic problem are comprised by Eqs. (3.7), (3.8) and

$$\tilde{w} = 0 \quad \text{for } 0 < \tilde{x} < \tilde{d},\ \tilde{y} = 1/2 \tag{25.23}$$

$$\frac{\partial \tilde{w}}{\partial \tilde{x}} = 0 \quad \text{for } \tilde{x} = 0, \tilde{x} = \tilde{d},\ 0 < \tilde{y} < 1/2 \tag{25.24}$$

This hydrodynamic problem has been solved analytically by Philip [15]. However, here, as in the original case, we solve it numerically (see Appendix B) to facilitate the solution of the thermal energy equation.

The relevant boundary conditions for the thermal problem are comprised of Eqs. (9.23)-(9.25) and

$$\frac{\partial \tilde{T}}{\partial \tilde{y}} = 0 \quad \text{for } 0 < \tilde{x} < \tilde{d},\ \tilde{y} = 1/2 \tag{25.25}$$

$$\frac{\partial \tilde{T}}{\partial \tilde{x}} = 0 \quad \text{for } \tilde{x} = 0, \tilde{x} = \tilde{d},\ 0 < \tilde{y} < 1/2 \tag{25.26}$$

$$\tilde{T} = 0 \quad \text{for } 0 < \tilde{x} < \tilde{d},\ 0 < \tilde{y} < 1/2,\ \tilde{z} \to -\infty \tag{25.27}$$

$$\tilde{T} = 1 \quad \text{for } 0 < \tilde{x} < \tilde{d},\ 0 < \tilde{y} < 1/2,\ \tilde{z} \to +\infty \tag{25.28}$$

and the two continuity conditions are identical with those provided by Eqs. (9.39) and (9.40) but they apply for $0 < \tilde{x} < \tilde{d}$ and $0 < \tilde{y} < 1/2$.

The boundary conditions for the eigenvalue problem are comprised of Eqs. (3.26), (3.27) and

$$\frac{\partial \psi_\pm}{\partial \tilde{y}} = 0 \qquad \text{for } 0 < \tilde{x} < \tilde{d},\ \tilde{y} = 1/2 \tag{25.29}$$

$$\frac{\partial \psi_\pm}{\partial \tilde{x}} = 0 \qquad \text{for } \tilde{x} = 0, \tilde{x} = \tilde{d},\ 0 < \tilde{y} < 1/2 \tag{25.30}$$

and for the particular solution are comprised of Eqs. (9.63), (9.64) and

$$\frac{\partial \tilde{T}_{\mathrm{p,i}}}{\partial \tilde{y}} = 0 \qquad \text{for } 0 < \tilde{x} < \tilde{d},\ \tilde{y} = 1/2 \tag{25.31}$$

$$\frac{\partial \tilde{T}_{\mathrm{p,i}}}{\partial \tilde{x}} = 0 \qquad \text{for } \tilde{x} = 0, \tilde{x} = \tilde{d},\ 0 < \tilde{y} < 1/2 \tag{25.32}$$

where $\mathrm{i} = \mathrm{Br}$ or $\tilde{\mathrm{q}}$.

Then, following the same procedure as in Sections 3.2, 10 and 10.2, it can be shown that the corresponding expression for the expansion coefficients is

$$c_i = \frac{\int_0^{1/2} \int_0^{\tilde{d}} \left[\tilde{w} + 2\lambda_i / \left(f\mathrm{RePe}^2\right)\right] \psi_i \mathrm{d}\tilde{x}\mathrm{d}\tilde{y}}{\int_0^{1/2} \int_0^{\tilde{d}} \left[\tilde{w} + 4\lambda_i / \left(f\mathrm{RePe}^2\right)\right] \psi_i^2 \mathrm{d}\tilde{x}\mathrm{d}\tilde{y}} \tag{25.33}$$

The local Nusselt number is given by the expression

$$\mathrm{Nu}_{l\pm} = \frac{\tilde{d}\left(F_{l,1\pm} \mp F_{l,2}\right)}{f\mathrm{Re}\left(F_{3\pm} \mp F_4\right)} \tag{25.34}$$

where

$$F_{l,1\pm} = \sum_{i=\pm 1}^{\pm\infty} c_i \exp\left(-\lambda_i \tilde{z}\right) \left.\frac{\partial \psi_i}{\partial \tilde{y}}\right|_{\tilde{y}=0} \tag{25.35}$$

$$F_{l,2} = \frac{\mathrm{Br}\left(f\mathrm{Re}\right)^2}{4} \left.\frac{\partial \tilde{T}_{\mathrm{p,Br}}}{\partial \tilde{y}}\right|_{\tilde{y}=0} + \tilde{q} \left.\frac{\partial \tilde{T}_{\mathrm{p},\tilde{\mathrm{q}}}}{\partial \tilde{y}}\right|_{\tilde{y}=0} \tag{25.36}$$

$$F_{3\pm} = \sum_{i=\pm 1}^{\pm\infty} c_i \exp\left(-\lambda_i \tilde{z}\right) \int_0^{1/2} \int_0^{\tilde{d}} \tilde{w} \psi_i \mathrm{d}\tilde{x}\mathrm{d}\tilde{y} \tag{25.37}$$

$$F_4 = \int_0^{1/2} \int_0^{\tilde{d}} \left[\frac{\mathrm{Br}\left(f\mathrm{Re}\right)^2}{4} \tilde{T}_{\mathrm{p,Br}} + \tilde{q} \tilde{T}_{\mathrm{p},\tilde{\mathrm{q}}}\right] \tilde{w} \mathrm{d}\tilde{x}\mathrm{d}\tilde{y} \tag{25.38}$$

The Nusselt number averaged over the composite interface is

$$\mathrm{Nu}_\pm = \frac{F_{1\pm} \mp F_2}{2\left(F_{3\pm} \mp F_4\right)} \tag{25.39}$$

where

$$
\begin{aligned}
F_{1\pm} &= \sum_{i=\pm 1}^{\pm\infty} \lambda_i c_i \exp\left(-\lambda_i \tilde{z}\right) \times \\
&\quad \int_0^{1/2} \int_0^{\tilde{d}} \left[\tilde{w} + \frac{2\lambda_i}{f\mathrm{Re}\mathrm{Pe}^2} \right] \psi_i \mathrm{d}\tilde{x}\mathrm{d}\tilde{y} && (25.40) \\
F_2 &= \frac{\tilde{d}}{2}\left(\mathrm{Br} + \frac{2\tilde{q}}{f\mathrm{Re}} \right) && (25.41)
\end{aligned}
$$

The fully-developed local Nusselt number and the fully-developed Nusselt number averaged over the composite interface when $\left|\tilde{z}_{\mathrm{Pe}\pm}\right| \ll \left|\tilde{z}\right| \ll \min\left(\left|\tilde{z}_{\mathrm{Br}\pm}\right|, \left|\tilde{z}_{\tilde{\mathrm{q}}\pm}\right|\right)$ are given by the expressions

$$
\mathrm{Nu}_{l,\mathrm{fd},\mathrm{Pe}\pm} = \frac{\tilde{d}\, \frac{\partial \psi_{\pm 1}}{\partial \tilde{y}}\Big|_{\tilde{y}=0}}{f\mathrm{Re} \int_0^{1/2} \int_0^{\tilde{d}} \tilde{w}\psi_{\pm 1} \mathrm{d}\tilde{x}\mathrm{d}\tilde{y}} \qquad (25.42)
$$

and

$$
\mathrm{Nu}_{\mathrm{fd},\mathrm{Pe}\pm} = \frac{\lambda_{\pm 1}}{2}\left(1 + \frac{2\lambda_{\pm 1}}{f\mathrm{Re}\mathrm{Pe}^2} \frac{\int_0^{1/2} \int_0^{\tilde{d}} \psi_{\pm 1} \mathrm{d}\tilde{x}\mathrm{d}\tilde{y}}{\int_0^{1/2} \int_0^{\tilde{d}} \tilde{w}\psi_{\pm 1} \mathrm{d}\tilde{x}\mathrm{d}\tilde{y}} \right) \qquad (25.43)
$$

respectively. When $\left|\tilde{z}\right| \gg \max\left(\left|\tilde{z}_{\mathrm{Br}\pm}\right|, \left|\tilde{z}_{\tilde{\mathrm{q}}\pm}\right|\right)$, the expression for the corresponding fully-developed local Nusselt number and the fully-developed Nusselt number averaged over the composite interface become

$$
\mathrm{Nu}_{l,\mathrm{fd},\mathrm{Br},\tilde{\mathrm{q}}\pm} = \frac{\tilde{d}F_{l,2}}{f\mathrm{Re}F_4} \qquad (25.44)
$$

and

$$
\mathrm{Nu}_{\mathrm{fd},\mathrm{Br},\tilde{\mathrm{q}}\pm} = \frac{F_2}{2F_4} \qquad (25.45)
$$

respectively. Moreover, when $\tilde{q} \gg \mathrm{Br}$ or $\tilde{q} = 0$, Eq. (25.45) yields

$$
\mathrm{Nu}_{\mathrm{fd},\tilde{\mathrm{q}}\pm} = \frac{\tilde{d}}{2f\mathrm{Re} \int_0^{1/2} \int_0^{\tilde{d}} \tilde{w}\tilde{T}_{\mathrm{p},\tilde{\mathrm{q}}} \mathrm{d}\tilde{x}\mathrm{d}\tilde{y}} \qquad (25.46)
$$

and

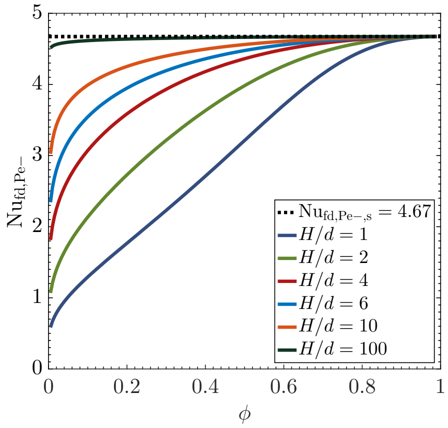

Figure 25.9: $\mathrm{Nu}_{\mathrm{fd,Pe-}}$ vs. ϕ for $\mathrm{Pe} = 1$ and selected H/d when one plate is textured with isothermal ridges and the other one is smooth and adiabatic.

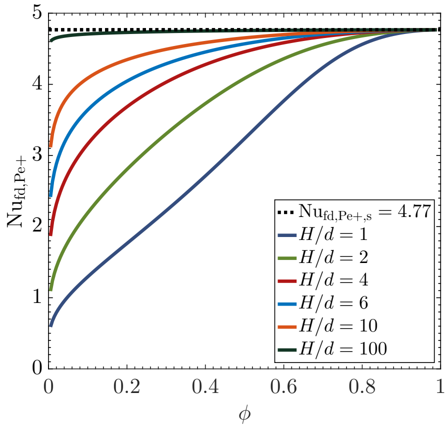

Figure 25.10: $\mathrm{Nu}_{\mathrm{fd,Pe+}}$ vs. ϕ for $\mathrm{Pe} = 1$ selected H/d when one plate is textured with isothermal ridges and the other one is smooth and adiabatic.

$$\mathrm{Nu}_{\mathrm{fd,Br}\pm} = \frac{\tilde{d}}{(f\mathrm{Re})^2 \int_0^{1/2} \int_0^{\tilde{d}} \tilde{w}\tilde{T}_{\mathrm{p,Br}} \mathrm{d}\tilde{x}\mathrm{d}\tilde{y}} \tag{25.47}$$

respectively.

Finally, we present the corresponding computed $\mathrm{Nu}_{\mathrm{fd,Pe}\pm}$, $\mathrm{Nu}_{\mathrm{fd,Br}\pm}$, $\mathrm{Nu}_{\mathrm{fd},\tilde{\mathrm{q}}\pm}$ and $\mathrm{Nu}_{\pm}$ in Figs. 25.9-25.18 for the same prescribed parameters as those in Figs. 11.1, 11.2, 11.4-11.11, respectively. Overall the results exhibit the same trends with those described in Section 5 with the exception that $\mathrm{Nu}_{\mathrm{fd,Pe-}}$ tends to zero as $\mathrm{Pe} \to \infty$.

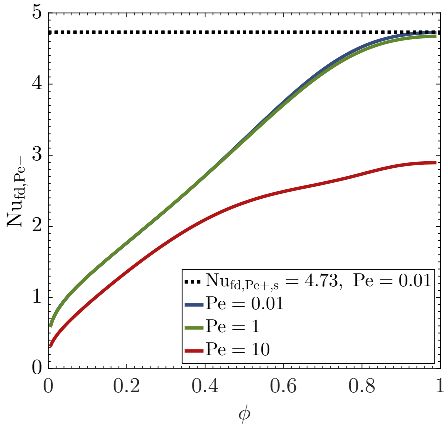

Figure 25.11: $\mathrm{Nu}_{\mathrm{fd,Pe-}}$ vs. ϕ for $\mathrm{Pe} = 0.01,\ 1,\ 10$ and $H/d = 1$ when one plate is textured with isothermal ridges and the other one is smooth and adiabatic.

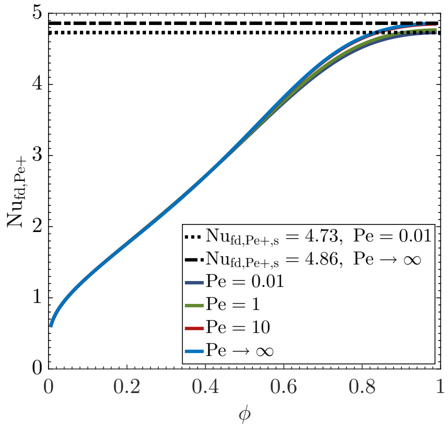

Figure 25.12: $\mathrm{Nu}_{\mathrm{fd,Pe+}}$ vs. ϕ for $\mathrm{Pe} = 0.01,\ 1,\ 10$ and $\mathrm{Pe} \to \infty$, $H/d = 1$ when one plate is textured with isothermal ridges and the other one is smooth and adiabatic.

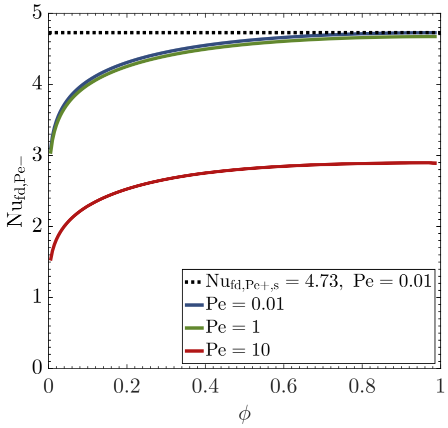

Figure 25.13: $\mathrm{Nu}_{\mathrm{fd,Pe-}}$ vs. ϕ for $\mathrm{Pe} = 0.01,\ 1,\ 10$ and $H/d = 10$ when one plate is textured with isothermal ridges and the other one is smooth and adiabatic.

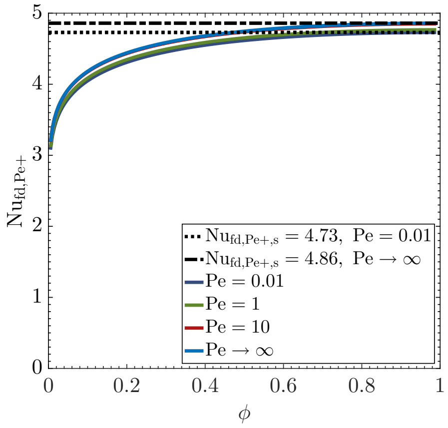

Figure 25.14: $\mathrm{Nu}_{\mathrm{fd,Pe+}}$ vs. ϕ for $\mathrm{Pe} = 0.01,\ 1,\ 10$ and $\mathrm{Pe} \to \infty$, and $H/d = 10$ when one plate is textured with isothermal ridges and the other one is smooth and adiabatic.

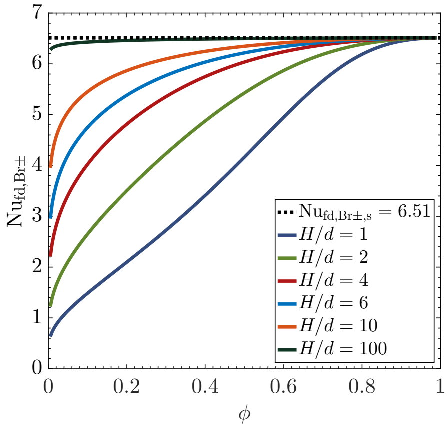

Figure 25.15: $\mathrm{Nu}_{\mathrm{fd,Br\pm}}$ vs. ϕ for selected H/d when one plate is textured with isothermal ridges and the other one is smooth and adiabatic.

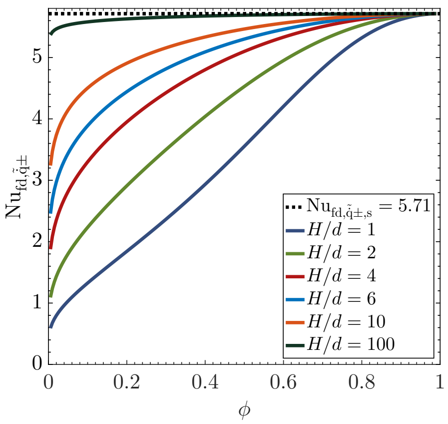

Figure 25.16: $\mathrm{Nu}_{\mathrm{fd},\tilde{\mathrm{q}}\pm}$ vs. ϕ for selected H/d when one plate is textured with isothermal ridges and the other one is smooth and adiabatic.

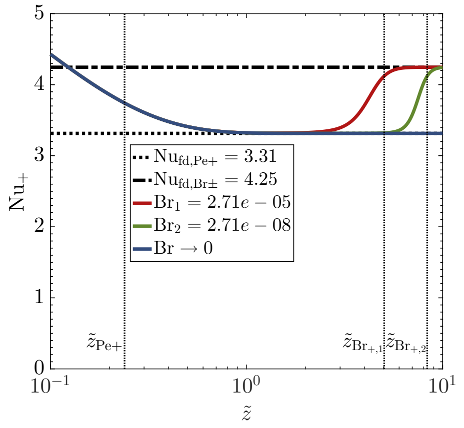

Figure 25.17: Nu_+ vs. $\tilde{z}$ for $\phi = 0.01$, $H/d = 10$, $\mathrm{Pe} = 1$ and $\tilde{\dot{q}} = 0$ when one plate is textured with isothermal ridges and the other one is smooth and adiabatic; $\tilde{z}_{\mathrm{Pe}+} = 0.24$, $\tilde{z}_{\mathrm{Br}+,1} = 5.03$ and $\tilde{z}_{\mathrm{Br}+,2} = 8.34$.

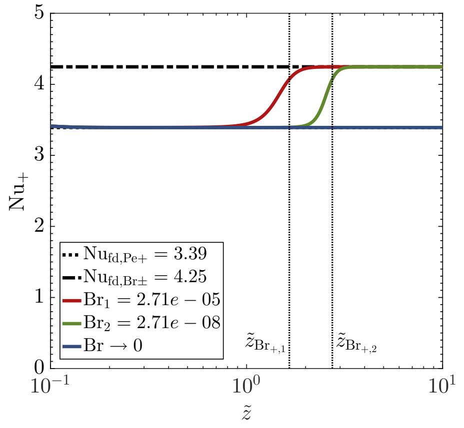

Figure 25.18: Nu_+ vs. $\tilde{z}$ for $\phi = 0.01$, $H/d = 10$, $\mathrm{Pe} = 10$ and $\tilde{\dot{q}} = 0$ when one plate is textured with isothermal ridges and the other one is smooth and adiabatic; $\tilde{z}_{\mathrm{Pe}+} = 0.05$, $\tilde{z}_{\mathrm{Br}+,1} = 1.65$ and $\tilde{z}_{\mathrm{Br}+,2} = 2.74$.

Appendix D

The non-linear eigenvalue problem presented in Section 9.2.1 was solved numerically using the Finite Element Method. The algorithm was coded in MATLAB® and results were obtained for multiple values of the aspect ratio of the domain (H/d), solid fraction of the ridges (ϕ) and Péclet number of the flow.

An overview of the algorithm is presented here and the detailed steps follow. For each pair of H/d and ϕ values, the algorithm initially solves the hydrodynamic problem to compute $\tilde{w}$ and the corresponding $f\mathrm{Re}$. Then, for the prescribed value of Pe, the $i-$th eigenvalue of interest (λ_i) is computed by carrying out iterations on inner and outer loops. Each iteration of the outer loop (indexed by m) refines the spatial discretization of the domain (mesh) to ensure mesh independence of the final results. Each iteration of the inner loop (indexed by j) computes a refined estimate of λ_i for the current mesh. This is accomplished by linearizing and solving Eq. (9.33) in the form

$$\nabla^2\psi_{i,m,j} = -\lambda_{i,m,j}\left(\frac{f\mathrm{Re}_m}{2}\tilde{w}_m + \frac{\lambda_{i,m,j-1,\mathrm{est}}}{\mathrm{Pe}^2}\right)\psi_{i,m,j} \tag{25.48}$$

where $\tilde{w}_m$ and $f\mathrm{Re}_m$ are the previously computed dimensionless velocity and Poiseuille number, respectively, from the current mesh, and $\lambda_{i,m,j-1,\mathrm{est}}$ is an estimate of λ_i from the previous ($j-1$) inner iteration.[1] This approach allows use of linear eigenvalue problem theory to solve the problem at hand at the expense that the process is iterative and only the computed eigenvalue of interest λ_i is valid, i.e., the solution process needs to be repeated if, for example, λ_{i+1} is also of interest. Moreover, in order to use the same code to calculate both the positive and negative eigenvalues, Eq. (25.48) is written in the form

$$\nabla^2\psi_{i,m,j} = -\lambda^*_{i,m,j}\left(\frac{i}{|i|}\frac{f\mathrm{Re}_m}{2}\tilde{w}_m + \frac{\lambda^*_{i,m,j-1,\mathrm{est}}}{\mathrm{Pe}^2}\right)\psi_{i,m,j} \tag{25.49}$$

---

[1] Note $\lambda_{i,m,j-1,\mathrm{est}} \neq \lambda_{i,m,j-1}$.

where

$$\lambda_{i,m,j}^{*} = \frac{i}{|i|}\lambda_{i,m,j} \tag{25.50}$$

The detailed steps of the solution process are as follows. In the first iteration of the outer loop ($m = 1$) the domain is discretized with an initial number of finite elements. Next, Eq. (9.5) is solved subject to the boundary conditions given by Eqs. (3.7)-(3.10) to determine $\tilde{w}_m(\tilde{x}, \tilde{y})$ and, subsequently, $f\mathrm{Re}_m$ required in Eq. (25.49). Then, Eq. (25.49) subject to the boundary conditions given by Eqs. (3.26)-(3.29) is solved iteratively within the inner loop to compute the eigenvalue of interest λ_i and the corresponding eigenfunction ψ_i for the current spatial discretization. At each iteration j of the inner loop, the code first uses the Arnoldi algorithm [68] to compute $\lambda_{i,m,j}^{*}$. Then, if $\lambda_{i,m,j}^{*} > \lambda_{i,m,j-1,\mathrm{est}}^{*}$, the new estimate is $\lambda_{i,m,j,\mathrm{est}}^{*} = \lambda_{i,m,j-1,\mathrm{est}}^{*} + \beta$, where $\beta > 0$, and if $\lambda_{i,m,j}^{*} < \lambda_{i,m,j-1,\mathrm{est}}^{*}$, the new estimate is $\lambda_{i,m,j,\mathrm{est}}^{*} = \lambda_{i,m,j}^{*}$ and $\beta = \beta/10$. The inner loop stops when $\left|\lambda_{i,m,j}^{*} - \lambda_{i,m,j-1,\mathrm{est}}^{*}\right| / \lambda_{i,m,j-1,\mathrm{est}}^{*} \leq 0.01\%$ and the corresponding value of j is recorded as $j - \mathrm{final}$. Next, the mesh is refined by adaptively placing elements in regions of sharp gradients and the algorithm proceeds from step two. The outer loop stops when $\left|\lambda_{i,m,j-\mathrm{final}}^{*} - \lambda_{i,m-1,j-\mathrm{final}}^{*}\right| / \lambda_{i,m-1,j-\mathrm{final}}^{*} \leq 0.01\%$.

The code was validated by computing λ_i and $\mathrm{Nu}_{\mathrm{fd,Pe}\pm}$ in the limit $\phi \to 1$ for the first ridge configuration, i.e., for smooth isothermal parallel plates, for different values of the Péclet number. The results are compared with those available in the literature in Tables 1 and 2. It is noted that due to a different nondimensionalization scheme, the results in Agrawal [36] and in Deavours [37] correspond to Pe/4 and to Pe/2, respectively, and the eigenvalues in both cases are multiplied by a factor of 1/16. The discrepancies are less than 0.1%, except for the case of $\mathrm{Nu}_{\mathrm{fd,Pe}-}$ for $\mathrm{Pe} = 2$, where it is 1.17%. This is attributed to the lack of more significant digits in the Nusselt number provided in [36], since the discrepancy in the corresponding eigenvalue is 0.02%.

Pe = 2			
	Code	[37]	%
λ_1	10.2236	10.2235	0.00
λ_{-1}	15.4358	15.4358	0.00
Pe = 4			
	Code	[36]	%
λ_1	16.7665	16.7664	0.00
λ_{-1}	37.5717	37.5776	0.02
λ_2	67.5856	67.5943	0.01
λ_3	117.8576	117.8707	0.01
λ_4	168.1265	168.0928	0.02
λ_5	218.4054	218.4320	0.01

Table 25.1: Comparison of computed λ_i for $\phi \to 1$ against literature.

Pe = 0.01			
	Code	[38]	%
$\mathrm{Nu}_{\mathrm{fd,Pe}+}$	8.1160	8.1155	0.01
Pe = 2			
	Code	[36]	%
$\mathrm{Nu}_{\mathrm{fd,Pe}+}$	7.7909	7.7960	0.07
$\mathrm{Nu}_{\mathrm{fd,Pe}-}$	8.9030	8.8	1.17

Table 25.2: Comparison of computed $\mathrm{Nu}_{\mathrm{fd,Pe}\pm}$ for $\phi \to 1$ against literature.

Appendix E

The two-dimensional particular problems for $\tilde{T}_{\mathrm{p,Br}}$ and $\tilde{T}_{\mathrm{p},\tilde{\mathrm{q}}}$ presented in Section 9.2.2 were numerically solved in an iterative manner using the Finite Element Method. The corresponding algorithms were coded in MATLAB® and results were obtained for multiple values of the aspect ratio of the domain (H/d) and the solid fraction (ϕ). Recall that $\tilde{T}_{\mathrm{p},\tilde{\mathrm{q}}}$ is identical to $\tilde{w}$ for the first ridge configuration and thus the corresponding problem does not need to be solved.

The steps of the algorithm for $\tilde{T}_{\mathrm{p,Br}}$ are as follows. First, the domain is discretized with an initial number of finite elements. Next, Eq. (9.5) is solved subject to the boundary conditions in Eqs. (3.7)-(3.10) to compute $\tilde{w}\left(\tilde{x},\tilde{y}\right)$ and then $\nabla\tilde{w}\left(\tilde{x},\tilde{y}\right)$ that is required in Eq. (9.62). Then, Eq. (9.62) is solved subject to the boundary conditions in Eqs (9.63)-(9.66) to compute $\tilde{T}_{\mathrm{p,Br}}\left(\tilde{x},\tilde{y}\right)$ and consequently $\mathrm{Nu}_{\mathrm{fd,Br\pm}}$. Next, the mesh is refined by adaptively increasing the element density in regions of sharp gradients of $\tilde{T}_{\mathrm{p,Br}}$, and the algorithm proceeds from step two. The process is repeated until the change in the computed value of $\mathrm{Nu}_{\mathrm{fd,Br\pm}}$ is less than 0.01%. The code was validated by computing $\mathrm{Nu}_{\mathrm{fd,Br\pm}}$ at the limit $\phi \to 1$ for the first ridge configuration, i.e., for smooth isothermal parallel plates, and the discrepancy with the corresponding result in the literature $\mathrm{Nu}_{\mathrm{fd,Br\pm,s}} = 17.5$[39] was found to be less than 0.05%.

The steps of the algorithm for $\tilde{T}_{\mathrm{p},\tilde{\mathrm{q}}}$ are as follows. First, the domain is discretized with an initial number of finite elements. Next, Eq. (9.69) is solved subject to the boundary conditions given by Eqs. (9.63)-(9.66) where $\mathrm{i} = \tilde{\mathrm{q}}$, to compute $\tilde{T}_{\mathrm{p},\tilde{\mathrm{q}}}\left(\tilde{x},\tilde{y}\right)$ and consequently $\mathrm{Nu}_{\mathrm{fd},\tilde{\mathrm{q}}\pm}$. Then, the mesh is adaptively refined and the algorithm proceeds from step two. The process is repeated until the change in the computed value of $\mathrm{Nu}_{\mathrm{fd},\tilde{\mathrm{q}}\pm}$ is less than 0.01%.

Appendix F

This sections contains the computed tabulation of $\overline{\mathrm{Nu}}_{\mathrm{B},\tilde{L}}$ for $\tilde{s} = [0.5125, 0.6]$, $\tilde{L} = [5.5, 52.5]$, $\tilde{t} = [0.01375, 0.2625]$, $\mathrm{Pr} = 0.71$, $K_{\mathrm{e}} = 6.56e - 5$ and $11.1e - 5$, and $\mathrm{Re}_{D_{\mathrm{h}}} = [51.68, 7627.46]$.

				$\overline{\mathrm{Nu}}_{\mathrm{B},\tilde{L}}$	
$\tilde{s}$	$\tilde{L}$	$\tilde{t}$	$\mathrm{Re}_{D_{\mathrm{h}}}$	$K_{\mathrm{e}} = 6.56e - 5$	$K_{\mathrm{e}} = 11.1e - 5$
0.5125	20.50	0.05125	126.53	65.93	60.28
0.5125	20.50	0.05125	329.29	128.52	108.77
0.5125	20.50	0.05125	623.01	172.45	140.68
0.5125	20.50	0.10250	126.53	60.65	57.72
0.5125	20.50	0.10250	329.29	128.32	115.07
0.5125	20.50	0.10250	623.01	181.24	156.36
0.5125	20.50	0.25625	126.53	44.40	43.48
0.5125	20.50	0.25625	329.29	100.25	95.10
0.5125	20.50	0.25625	623.01	149.03	137.71
0.5125	51.25	0.05125	53.78	13.52	13.37
0.5125	51.25	0.05125	152.18	35.41	34.37
0.5125	51.25	0.05125	304.44	65.98	61.04
0.5125	51.25	0.10250	53.78	11.68	11.62
0.5125	51.25	0.10250	152.18	30.90	30.54
0.5125	51.25	0.10250	304.44	59.51	57.50
0.5125	51.25	0.25625	53.78	8.22	8.20
0.5125	51.25	0.25625	152.18	21.82	21.74
0.5125	51.25	0.25625	304.44	42.72	42.25
0.5250	10.50	0.02625	664.31	151.08	126.14
0.5250	10.50	0.02625	1471.90	190.88	155.72
0.5250	10.50	0.02625	2501.59	221.47	178.38
0.5250	10.50	0.05250	664.31	164.56	145.36
0.5250	10.50	0.05250	1471.90	215.27	185.19
0.5250	10.50	0.05250	2501.59	255.52	215.98
0.5250	10.50	0.13125	664.31	149.94	140.77
0.5250	10.50	0.13125	1471.90	203.49	187.43
0.5250	10.50	0.13125	2501.59	248.30	225.34

Table 25.3: Computed $\overline{\mathrm{Nu}}_{\mathrm{B},\tilde{L}}$ for different values of $\tilde{s}$, $\tilde{L}$, $\tilde{t}$, $\mathrm{Re}_{D_{\mathrm{h}}}$, K_{e}, and $\mathrm{Pr} = 0.71$.

				$\overline{\mathrm{Nu}}_{\mathrm{B},\tilde{L}}$	
$\tilde{s}$	$\tilde{L}$	$\tilde{t}$	$\mathrm{Re}_{D_\mathrm{h}}$	$K_\mathrm{e} = 6.56e-5$	$K_\mathrm{e} = 11.1e-5$
0.5250	21.00	0.05250	121.73	35.86	35.20
0.5250	21.00	0.05250	316.63	80.04	75.47
0.5250	21.00	0.05250	598.86	117.71	107.47
0.5250	21.00	0.10500	121.73	31.13	30.86
0.5250	21.00	0.10500	316.63	71.70	69.54
0.5250	21.00	0.10500	598.86	108.52	103.11
0.5250	21.00	0.26250	121.73	21.95	21.87
0.5250	21.00	0.26250	316.63	51.56	50.92
0.5250	21.00	0.26250	598.86	79.62	77.89
0.5250	26.25	0.02625	359.17	75.63	68.55
0.5250	26.25	0.02625	882.92	121.32	103.85
0.5250	26.25	0.02625	1608.20	149.95	125.26
0.5250	26.25	0.05250	359.17	74.75	70.93
0.5250	26.25	0.05250	882.92	127.66	115.73
0.5250	26.25	0.05250	1608.20	162.87	144.20
0.5250	26.25	0.13125	359.17	62.59	61.29
0.5250	26.25	0.13125	882.92	112.42	107.40
0.5250	26.25	0.13125	1608.20	147.71	139.04
0.5250	52.50	0.05250	51.68	6.58	6.56
0.5250	52.50	0.05250	146.33	17.53	17.49
0.5250	52.50	0.05250	292.89	34.41	34.08
0.5250	52.50	0.10500	51.68	5.66	5.65
0.5250	52.50	0.10500	146.33	15.05	15.03
0.5250	52.50	0.10500	292.89	29.65	29.55
0.5250	52.50	0.26250	51.68	3.96	3.96
0.5250	52.50	0.26250	146.33	10.55	10.54
0.5250	52.50	0.26250	292.89	20.80	20.78

Table 25.4: Computed $\overline{\mathrm{Nu}}_{\mathrm{B},\tilde{L}}$ for different values of $\tilde{s}$, $\tilde{L}$, $\tilde{t}$, $\mathrm{Re}_{D_\mathrm{h}}$, K_e, and $\mathrm{Pr} = 0.71$.

				$\overline{\mathrm{Nu}}_{\mathrm{B},\tilde{L}}$	
$\tilde{s}$	$\tilde{L}$	$\tilde{t}$	$\mathrm{Re}_{D_\mathrm{h}}$	$K_\mathrm{e} = 6.56e - 5$	$K_\mathrm{e} = 11.1e - 5$
0.5500	5.50	0.01375	2272.67	175.89	146.31
0.5500	5.50	0.01375	4699.40	221.03	180.54
0.5500	5.50	0.01375	7627.46	256.72	207.78
0.5500	5.50	0.02750	2272.67	201.60	176.61
0.5500	5.50	0.02750	4699.40	261.45	223.55
0.5500	5.50	0.02750	7627.46	309.80	260.73
0.5500	5.50	0.06875	2272.67	204.70	190.86
0.5500	5.50	0.06875	4699.40	275.42	251.83
0.5500	5.50	0.06875	7627.46	335.44	302.12
0.5500	11.00	0.02750	611.90	94.88	88.20
0.5500	11.00	0.02750	1355.18	128.81	117.25
0.5500	11.00	0.02750	2302.55	156.92	140.62
0.5500	11.00	0.05500	611.90	92.14	88.49
0.5500	11.00	0.05500	1355.18	127.53	120.80
0.5500	11.00	0.05500	2302.55	157.74	147.79
0.5500	11.00	0.13750	611.90	76.48	75.17
0.5500	11.00	0.13750	1355.18	107.31	104.79
0.5500	11.00	0.13750	2302.55	134.24	130.38
0.5500	13.75	0.01375	1559.48	114.99	99.52
0.5500	13.75	0.01375	3331.16	148.02	125.03
0.5500	13.75	0.01375	5525.11	174.40	145.07
0.5500	13.75	0.02750	1559.48	124.82	113.91
0.5500	13.75	0.02750	3331.16	165.64	147.78
0.5500	13.75	0.02750	5525.11	199.54	175.07
0.5500	13.75	0.06875	1559.48	120.22	115.15
0.5500	13.75	0.06875	3331.16	163.95	154.91
0.5500	13.75	0.06875	5525.11	201.92	188.63

Table 25.5: Computed $\overline{\mathrm{Nu}}_{\mathrm{B},\tilde{L}}$ for different values of $\tilde{s}$, $\tilde{L}$, $\tilde{t}$, $\mathrm{Re}_{D_\mathrm{h}}$, K_e, and $\mathrm{Pr} = 0.71$.

				$\overline{\mathrm{Nu}}_{\mathrm{B},\tilde{L}}$	
$\tilde{s}$	$\tilde{L}$	$\tilde{t}$	$\mathrm{Re}_{D_\mathrm{h}}$	$K_\mathrm{e} = 6.56e-5$	$K_\mathrm{e} = 11.1e-5$
0.5500	27.50	0.02750	333.41	39.71	38.80
0.5500	27.50	0.02750	815.93	71.05	67.35
0.5500	27.50	0.02750	1481.73	93.37	86.97
0.5500	27.50	0.05500	333.41	36.99	36.58
0.5500	27.50	0.05500	815.93	67.82	65.94
0.5500	27.50	0.05500	1481.73	90.47	87.03
0.5500	27.50	0.13750	333.41	29.86	29.74
0.5500	27.50	0.13750	815.93	55.63	54.99
0.5500	27.50	0.13750	1481.73	74.96	73.74
0.6000	6.00	0.01500	1953.91	110.52	102.2
0.6000	6.00	0.01500	4051.44	148.93	135.06
0.6000	6.00	0.01500	6587.88	181.46	162.14
0.6000	6.00	0.03000	1953.91	112.34	107.49
0.6000	6.00	0.03000	4051.44	154.31	145.63
0.6000	6.00	0.03000	6587.88	190.93	178.19
0.6000	6.00	0.07500	1953.91	102.97	101.02
0.6000	6.00	0.07500	4051.44	143.44	139.77
0.6000	6.00	0.07500	6587.88	179.62	174.01
0.6000	15.00	0.01500	1333.70	64.30	61.19
0.6000	15.00	0.01500	2857.62	88.19	82.69
0.6000	15.00	0.01500	4749.35	108.84	100.83
0.6000	15.00	0.03000	1333.70	63.75	62.08
0.6000	15.00	0.03000	2857.62	88.56	85.47
0.6000	15.00	0.03000	4749.35	110.47	105.81
0.6000	15.00	0.07500	1333.70	57.45	56.82
0.6000	15.00	0.07500	2857.62	80.48	79.28
0.6000	15.00	0.07500	4749.35	101.15	99.28

Table 25.6: Computed $\overline{\mathrm{Nu}}_{\mathrm{B},\tilde{L}}$ for different values of $\tilde{s}$, $\tilde{L}$, $\tilde{t}$, $\mathrm{Re}_{D_\mathrm{h}}$, K_e, and $\mathrm{Pr} = 0.71$..

Nomenclature

LB	lower bound of λ_i
UB	upper bound of λ_i
i	indicator
j	indicator
m	indicator
est	estimate
s	smooth plates

Bibliography

[1] Sparrow, E., Baliga, B., and Patankar, S., 1978. "Forced convection heat transfer from a shrouded fin array with and without tip clearance". *ASME J. Heat Transfer,* ***100***(4), pp. 572–579.

[2] Karamanis, G., and Hodes, M. "Conjugate nusselt numbers for simultaneously-developing flow through rectangular ducts". *Journal of Heat Transfer*. Submitted.

[3] Karamanis, G., Hodes, M., Kirk, T., and Papageorgiou, D., 2017. "Solution of the graetz-nusselt problem for liquid flow over isothermal parallel ridge". *Journal of Heat Transfer,* ***139***(9).

[4] Karamanis, G., Hodes, M., Kirk, T., and Papageorgiou, D. T., 2018. "Solution of the extended graetz–nusselt problem for liquid flow over isothermal parallel ridges". *Journal of Heat Transfer,* ***140***(6), p. 061703.

[5] Karamanis, G., and Hodes, M. "Simultaneous optimization of an array of heat sinks". *ASME Journal of Electronic Packaging*. Submitted.

[6] Kirk, T., Hodes, M., and Papageorgiou, D. T., 2017. "Nusselt numbers for poiseuille flow over isoflux parallel ridges accounting for meniscus curvature". *Journal of Fluid Mechanics,* ***811***, 001, pp. 315–349.

[7] Game, S., Hodes, M., Kirk, T., and Papageorgiou, D. T., 2018. "Nusselt numbers for poiseuille flow over isoflux parallel ridges for arbitrary meniscus curvature". *Journal of Heat Transfer,* ***140***(8), p. 081701.

[8] Lam, L. S., Hodes, M., and Enright, R., 2015. "Analysis of galinstan-based microgap cooling enhancement using structured surfaces". *Journal of Heat Transfer,* ***137***(9), p. 091003.

[9] Lobaton, E., and Salamon, T., 2007. "Computation of constant mean curvature surfaces: Application to the gas-liquid interface of a pressurized fluid on a superhydrophobic surface". *Journal of Colloid and Interface Science,* ***314***(1), pp. 184 – 198.

[10] Quéré, D., 2005. "Non-sticking drops". *Reports on Progress in Physics,* ***68***(11), p. 2495.

[11] Cassie, A., and Baxter, S., 1944. "Wettability of porous surfaces". *Transactions of the Faraday Society,* ***40***, pp. 546–551.

[12] Huang, D. M., Sendner, C., Horinek, D., Netz, R. R., and Bocquet, L., 2008. "Water slippage versus contact angle: A quasiuniversal relationship". *Phys. Rev. Lett.,* ***101***, Nov, p. 226101.

[13] Cottin-Bizonne, C., Steinberger, A., Cross, B., Raccurt, O., and Charlaix, E., 2008. "Nanohydrodynamics: The intrinsic flow boundary condition on smooth surfaces". *Langmuir,* ***24***(4), pp. 1165–1172. PMID: 18266337.

[14] Enright, R., Hodes, M., Salamon, T., and Muzychka, Y., 2014. "Isoflux nusselt number and slip length formulae for superhydrophobic microchannels". *Journal of Heat Transfer,* ***136***(1), p. 012402.

[15] Philip, J. R., 1972. "Flows satisfying mixed no-slip and no-shear conditions". *Zeitschrift für angewandte Mathematik und Physik ZAMP,* ***23***(3), pp. 353–372.

[16] Sbragaglia, M., and Prosperetti, A., 2007. "A note on the effective slip properties for microchannel flows with ultrahydrophobic surfaces". *Physics of Fluids (1994-present),* ***19***(4), p. 043603.

[17] Rothstein, J. P., 2010. "Slip on superhydrophobic surfaces". *Annual Review of Fluid Mechanics,* ***42***, pp. 89–109.

[18] Teo, C., and Khoo, B., 2009. "Analysis of stokes flow in microchannels with superhydrophobic surfaces containing a periodic array of micro-grooves". *Microfluidics and nanofluidics,* ***7***(3), pp. 353–382.

[19] Teo, C. J., and Khoo, B. C., 2010. "Flow past superhydrophobic surfaces containing longitudinal grooves: effects of interface curvature". *Microfluidics and Nanofluidics,* ***9***(2), pp. 499–511.

[20] Ng, C.-O., and Wang, C. Y., 2014. "Temperature jump coefficient for superhydrophobic surfaces". *Journal of Heat Transfer,* ***136***(6), p. 064501.

[21] Lam, L. S., Hodes, M., Karamanis, G., Kirk, T., and MacLachlan, S., 2016. "Effect of meniscus curvature on apparent thermal slip". *Journal of Heat Transfer,* ***138***(12), p. 122004.

[22] Hodes, M., Lam, L. S., Cowley, A., Enright, R., and MacLachlan, S., 2015. "Effect of evaporation and condensation at menisci on apparent thermal slip". *Journal of Heat Transfer,* ***137***(7), p. 071502.

[23] Lam, L. S., Melnick, C., Hodes, M., Ziskind, G., and Enright, R., 2014. "Nusselt numbers for thermally developing couette flow with hydrodynamic and thermal slip". *Journal of Heat Transfer,* ***136***(5), p. 051703.

[24] Maynes, D., Webb, B., and Davies, J., 2008. "Thermal transport in a microchannel exhibiting ultrahydrophobic microribs maintained at constant temperature". *Journal of Heat Transfer,* ***130***(2), p. 022402.

[25] Maynes, D., Webb, B., Crockett, J., and Solovjov, V., 2013. "Analysis of laminar slip-flow thermal transport in microchannels with transverse rib and cavity structured superhydrophobic walls at constant heat flux". *Journal of heat transfer,* ***135***(2), p. 021701.

[26] Maynes, D., and Crockett, J., 2014. "Apparent temperature jump and thermal transport in channels with streamwise rib and cavity featured superhydrophobic walls at constant heat flux". *Journal of Heat Transfer,* ***136***(1), p. 011701.

[27] Shah, R., and London, A., 1978. *Laminar flow forced convection in ducts: a source book for compact heat exchanger analytical data.* Academic Press.

[28] Nusselt, W., 1923. "Der wärmeaustausch am berieselungskühler". *VDI-Z,* ***67***(9), pp. 206–216.

[29] Brown, G. M., 1960. "Heat or mass transfer in a fluid in laminar flow in a circular or flat conduit". *AIChE Journal,* ***6***(2), pp. 179–183.

[30] Mikhaĭlov, M. D., and Özışık, M. N., 1994. *Unified analysis and solutions of heat and mass diffusion.* Courier Corporation.

[31] Hodes, M., Kirk, T., Karamanis, G., and MacLachlan, S., 2017. "Effect of thermocapillary stress on slip length for a channel textured with parallel ridges". *Journal of Fluid Mechanics,* ***814***, pp. 301–324.

[32] Panton, R. L., 2006. *Incompressible flow.* John Wiley & Sons.

[33] Maynes, D., Jeffs, K., Woolford, B., and Webb, B. W., 2007. "Laminar flow in a microchannel with hydrophobic surface patterned microribs oriented parallel to the flow direction". *Physics of Fluids,* ***19***(9).

[34] Ng, C.-O., Chu, H. C. W., and Wang, C. Y., 2010. "On the effects of liquid-gas interfacial shear on slip flow through a parallel-plate channel with superhydrophobic grooved walls". *Physics of Fluids,* ***22***(10).

[35] Marshall, J. S., 2017. "Exact formulae for the effective slip length of a symmetric superhydrophobic channel with flat or weakly curved menisci". *SIAM Journal on Applied Mathematics,* ***77***(5), pp. 1606–1630.

[36] Agrawal, H., 1960. "Heat transfer in laminar flow between parallel plates at small peclet numbers". *Applied Scientific Research,* ***9***(1), pp. 177–189.

[37] Deavours, C., 1974. "An exact solution for the temperature distribution in parallel plate poiseuille flow". *Journal of Heat Transfer,* ***96***(4), pp. 489–495.

[38] Pahor, S., and Strnad, J., 1961. "A note on heat transfer in laminar flow through a gap". *Applied Scientific Research,* ***10***(1), pp. 81–84.

[39] Dang, V.-D., 1983. "Heat transfer of power law fluid at low peclet number flow". *Journal of heat transfer,* ***105***(3), pp. 542–549.

[40] Jambal, O., Shigechi, T., Davaa, G., and Momoki, S., 2005. "Effects of viscous dissipation and fluid axial heat conduction on heat transfer for non-newtonian fluids in ducts with uniform wall temperature: Part i: Parallel plates and circular ducts". *International communications in heat and mass transfer,* ***32***(9), pp. 1165–1173.

[41] Sparrow, E., Novotny, J., and Lin, S., 1963. "Laminar flow of a heat-generating fluid in a parallel-plate channel". *AIChE Journal,* ***9***(6), pp. 797–804.

[42] Nellis, G. F., and Klein, S. A., 2009. *Heat Transfer.* Cambridge University Press, New York.

[43] Clark, S., and Kays, W., 1953. "Laminar-flow forced convection in rectangular tubes". *Trans. ASME,* ***75***(5).

[44] Savino, J. M., and Siegel, R., 1964. "Laminar forced convection in rectangular channels with unequal heat addition on adjacent sides". *International Journal of Heat and Mass Transfer,* ***7***(7), pp. 733–741.

[45] Schmidt, F., and Newell, M., 1967. "Heat transfer in fully developed laminar flow through rectangular and isosceles triangular ducts". *International journal of heat and mass transfer,* ***10***(8), pp. 1121–1123.

[46] Shah, R. K., and London, A. L., 1971. *Laminar flow forced convection heat transfer and flow friction in straight and curved ducts-A summary of analytical solutions.* Academic Press, New York.

[47] Montgomery, S., and Wibulswas, P., 1966. "Laminar flow heat-transfer in ducts of rectangular cross-section". In International Heat Transfer Conference, 3 RD, Chicago, IL, pp. 104–112.

[48] Montgomery, S., and Wibulswas, P., 1968. "Laminar flow heat transfer for simultaneously developing velocity and temperature profiles in ducts of rectangular cross section". *Applied Scientific Research,* ***18***(1), pp. 247–259.

[49] Han, L., 1959. "Laminar heat transfer in rectangular channels". *Journal of Heat Transfer (US),* ***81***.

[50] Karamanis, G., and Hodes, M., 2016. "Longitudinal-fin heat sink optimization capturing conjugate effects under fully developed conditions". *ASME Journal of Thermal Science and Engineering Applications,* ***8***(4), August 23, pp. 041011–041011–7.

[51] Siegel, R., and Savino, J. M., 1965. "An analytical solution of the effect of peripheral wall conduction on laminar forced convection in rectangular channels". *Journal of Heat Transfer,* ***87***(1), pp. 59–66.

[52] Lyczkowski, R., Solbrig, C., and Gidaspow, D., 1982. "Forced convection heat transfer in rectangular ducts general-case of wall resistances and peripheral conduction for ventilation cooling of nuclear waste repositories". *Nuclear Engineering and Design,* ***67***(3), pp. 357–378.

[53] Moharana, M. K., Singh, P. K., and Khandekar, S., 2012. “Optimum nusselt number for simultaneously developing internal flow under conjugate conditions in a square microchannel”. *Journal of Heat Transfer,* ***134***(7), p. 071703.

[54] Karamanis, G., and Hodes, M., 2017. “Optimal design of longitudinal-fin heat sinks accounting for simultaneously developing flow and conjugate effects.”. In Proceedings of the 2nd Thermal and Fluid Engineering Conference.

[55] Karamanis, G., and Hodes, M., 2018. “Algorithm for simultaneous optimization of an array of heat sinks”. In IEEE ITherm San Diego. P225.

[56] Moharana, M. K., Peela, N. R., Khandekar, S., and Kunzru, D., 2011. “Distributed hydrogen production from ethanol in a microfuel processor: Issues and challenges”. *Renewable and Sustainable Energy Reviews,* ***15***(1), pp. 524–533.

[57] Kolb, G., and Hessel, V., 2004. “Micro-structured reactors for gas phase reactions”. *Chemical Engineering Journal,* ***98***(1), pp. 1–38.

[58] *ANSYS FLUENT Theory Guide, ANSYS Inc., November 2013.*

[59] Kraus, A. D., and Bar-Cohen, A., 1983. “Thermal analysis and control of electronic equipment”. *Washington, DC, Hemisphere Publishing Corp., 1983, 633 p.*

[60] Holahan, M. F., Kang, S. S., and Bar-Cohen, A., 1996. “A flowstream based analytical model for design of parallel plate heatsinks”. *American Society of Mechanical Engineers, Heat Transfer Division,(Publication) HTD,* ***329***(7), pp. 63–71.

[61] Patankar, S., 1980. *Numerical heat transfer and fluid flow.* CRC press.

[62] Innovative Research, I. *MacroFlow User Manual.* 2520 Broadway Street NE, Suite 200, Minneapolis, MN 55413.

[63] Idelchik, I. E., 1986. “Handbook of hydraulic resistance”. *Washington, DC, Hemisphere Publishing Corp., 1986, 662 p. Translation.*

[64] Blevins, R. D., 1984. “Applied fluid dynamics handbook”. *New York, Van Nostrand Reinhold Co., 1984, 568 p.*

[65] Bertsekas, D. P., 1999. *Nonlinear programming.* Athena scientific Belmont.

[66] Byrd, R. H., Gilbert, J. C., and Nocedal, J., 2000. "A trust region method based on interior point techniques for nonlinear programming". *Mathematical Programming,* ***89***(1), pp. 149–185.

[67] *Optimization Toolbox User's Guide, MathWorks Inc., March 2016.*

[68] *Partial Differential Equation Toolbox User's Guide, MathWorks Inc., March 2016.*

[69] McCuen, P., Kays, W., and Reynolds, W., 1962. *Heat Transfer with Laminar and Turbulent Flow Between Parallel Planes with Constant and Variable Wall Temperature and Heat Flux.* Department of Mechanical Engineering, Stanford University, Stanford, California.

[70] Shah, R., 1975. "Thermal entry length solutions for the circular tube and parallel plates". In Third National Heat Mass Transfer Conference, Indian Institute of Technology, Bombay, India, Vol. 1, pp. 11–75.

[71] Patankar, S., Liu, C., and Sparrow, E., 1977. "Fully developed flow and heat transfer in ducts having streamwise-periodic variations of cross-sectional area". *Journal of Heat Transfer,* ***99***(2), pp. 180–186.